

DEFORMATION OF TWO-DIMENSIONAL AMORPHOUS  
GRANULAR PACKINGS

Jennifer M. Rieser

A DISSERTATION

in

Physics and Astronomy

Presented to the Faculties of the University of Pennsylvania

in

Partial Fulfillment of the Requirements for the

Degree of Doctor of Philosophy

2015

---

Douglas J. Durian, Professor of Physics  
Supervisor of Dissertation

---

Marija Drndic, Professor of Physics  
Graduate Group Chairperson

Dissertation Committee:

Paulo E. Arratia - Associate Professor of Mechanical Engineering and Applied Mechanics

Robert W. Carpick - Professor of Mechanical Engineering and Applied Mechanics

Eugene W. Beier - Professor of Physics

Douglas J. Durian - Professor of Physics

Andrea J. Liu - Professor of Physics

DEFORMATION OF TWO-DIMENSIONAL AMORPHOUS GRANULAR PACKINGS



2015

Jennifer M. Rieser

This work is licensed under the  
Creative Commons Attribution-  
NonCommercial-ShareAlike 4.0  
Unported License

To view a copy of this license, visit  
<http://creativecommons.org/licenses/by-nc-sa/4.0/>

Dedicated to my parents,  
Michael and Anna Rieser

## Acknowledgments

While this thesis bears my name, its completion would not have been possible without the meaningful interactions and unwavering support of many. I am forever grateful to all of you. I will take some time to acknowledge particularly influential individuals here.

My advisor, Doug Durian, has had a profound impact on my development as a scientist. His creativity, excitement for new data, particular attention to detail, and the high standards to which he holds both his students and scientific results have all been positive influences. He has been supportive and reassuring, reminding me on more than one occasion to "Never give up, never surrender." Throughout these past several years, Doug has provided a research environment that has given me the freedom to explore new ideas and wander down stray paths, yet he has been there to reign me back in when I have strayed too far into the wilderness. I have no doubt that I am a better scientist as a result of my interactions with and guidance from Doug.

Though my interactions with my co-advisor, Jerry Gollub, ended abruptly and much too soon, I am extremely fortunate to have had him as a research mentor. Jerry's friendly nature and his passion for teaching and research shine through in the interactions he has with his students. He is patient and takes great care to make sure that things are clear and understandable. I am sure that I did not always succeed in meeting his high expectations, but striving to do so has undoubtedly made me a better scientist.

My current and former labmates Anthony Chieco, Carlos Ortiz, Juha Koivisto, Kerstin Nordstrom, Lynn Daniels, Yuli Wei, Adam Roth, Yuka Takehara, and in particular Charles Thomas and Ted Brzinski have provided advice, encouragement, and thoughtful discussions over the years. These interactions have been very helpful and are greatly appreciated. And an extra-special thanks to Ted for introducing me to good coffee and helping me realize the full extent of my coffee snobbery. I do not know that I will ever achieve Ted's level of pretentiousness (for coffee, of course), but good coffee does make me happy.

I have been fortunate to have some excellent collaborations and discussions over these past several years. Interactions with Arjun Yodh, Andrea Liu, Paulo Arratia, Carl Goodrich, Sam Schoenholz, Dan Gianola, Jim Sethna, Ju Li, and Wenbin Li have proven very helpful and have definitely improved the quality of the work presented here.

My committee members, Doug Durian, Paulo Arratia, Andrea Liu, Rob Carpick, and Gene Beier generously donated their time and assistance. They have provided numerous helpful discussions and suggestions as well as the support provided throughout my time at Penn.

Jeff Hancock and Buddy Borders, machinists in the machine shop, built the experimental apparatus used to perform all experiments. Throughout the years, they have been very helpful, providing feedback on design ideas as well as occasionally supplying spare scraps for whatever random idea I had at any given time.

Several people at Georgia Tech have contributed profoundly to my academic upbringing, starting with Mohan Srinivasarao, who organized and lead seminars for high school students and introduced me to the fascinating world of soft matter. It was at these seminars that I found my interest in research and love of science, and it because of these seminars that I attended Georgia Tech.

Martin Jarrio sparked my interest in physics in the first minutes of the first Physics I lecture. His enthusiasm, patience, and encouragement along with his 14+ hours of office hours per week, the preponderance of which were occupied by me, are the reason I began this journey.

Andy Zangwill's course taught me the very important (though then painful) lesson that brute-force is often not the best approach. He has forever changed the way I think about and approach problems, and his encouragement and assistance throughout my undergraduate career and even to this day are greatly appreciated.

Mike Schatz, my undergraduate research advisor, provided me with my first opportunity to do research. His general exuberance, passion for research, willingness to help, encouragement to try new things along with his understanding and patience when things did not work out made my

time in his lab fun. He is undoubtedly the reason I pursued a PhD, and he continues to be an important mentor and confidante.

My very dear friend, Vivek Sharma, and I met in the Schatz lab at Georgia Tech. The countless cups of coffee that we shared, each accompanied by wonderful a conversation, have meant so much over the years. Vivek has freely offered his friendship, advice, encouragement, assistance, and shared his beautiful poetry. He has been and continues to be a truly wonderful friend.

My parents, Michael and Anna Rieser, have always nurtured my inquisitive nature and emphasized the importance of education. Informing me from a young age that there would come a time when they could no longer answer my questions, they encouraged me to not be shy about seeking assistance from others. I am forever grateful for the unconditional love and support they have provided throughout my life.

My husband, Gordon Berman, and I first met in 2006. He was and continues to be one of the kindest and most caring people I have ever met. We have shared so many wonderful moments over the years. His friendship, encouragement, and sense of humor, along with the daily cup of pour-over coffee prepared and hand-delivered to awaken me each morning have helped me maintain my sanity over these past several years.

Jack and Catherine Berman, without whom Gordon would not be here, have always been very warm and welcoming, and we've had many great times over these past nine years. I am very fortunate to have such wonderful people as in-laws.

Finally, these acknowledgements would not be complete without mentioning my pets. Escher the dog has provided unconditional love and support over these past 5 years, and, over the past 8 years, Dizzy cat has consistently shown great affection when he is hungry and when I am in his chair.

## ABSTRACT

### DEFORMATION OF TWO-DIMENSIONAL AMORPHOUS GRANULAR PACKINGS

Jennifer M. Rieser

Douglas J. Durian

A microscopic understanding of how amorphous materials deform in response to an imposed disturbance is lacking. In this thesis, the connection between local structure and the observed dynamics is explored experimentally in a disordered granular pillar subjected to a quasi-static deformation. The pillar is composed of a single layer of grains, allowing for easy visualization of all particles throughout the deformation. The addition of a liquid into the system causes capillary bridges form between the grains, making the grains cohesive. The two-dimensionality of the system ensures that the liquid is distributed uniformly throughout the packing, making the cohesive forces between the grains known everywhere. We perform separate experiments to measure these capillarity-induced forces, and we find these measurements to be in excellent agreement with our theoretical model and numerical calculations. In the main experiments presented in this thesis, we explore the quasi-static deformation of granular pillar subjected to uniaxial compression. We find a statistical correlation between the local dynamics, characterized by the deviatoric strain rate, and the local structure, characterized by a new measure, introduced here, akin to a relative free area. This correlation is stronger in the presence of cohesion and indicates that regions that are more (less) well packed relative to their surroundings experience lower (higher) strain rates than their surroundings. The deviatoric strain rate also highlights shear bands within the deforming pillar. These shear bands are transient, moving around as the compression occurs. We have developed a way to identify these extended bands, and we compare the structure within these bands to the structure outside. Preliminary results suggest that these shear bands coincide with paths through the material that tend to have more underpacked regions than other parallel in the

vicinity of the shear band.

# Contents

<b>Introduction</b>	<b>1</b>
<b>1 Experimental Setup and Image Analysis</b>	<b>6</b>
1.1 Introduction . . . . .	6
1.2 Experimental setup . . . . .	7
1.2.1 Compression of two-dimensional granular pillars . . . . .	9
1.2.2 Indentation of two-dimensional granular pillars . . . . .	10
1.3 Image analysis . . . . .	11
1.3.1 Particle centers and velocities . . . . .	13
1.3.2 Particle orientations and angular velocities . . . . .	15
<b>2 Tunable Capillary-Induced Interaction Between Vertical Cylinders</b>	<b>20</b>
2.1 Introduction . . . . .	21
2.2 Methods . . . . .	23
2.2.1 Experimental Setup . . . . .	23
2.2.2 Numerical Calculations . . . . .	27
2.2.3 Theoretical Model . . . . .	28
2.3 Results and Discussion . . . . .	31
2.3.1 Interactions Between Cylinder Pairs . . . . .	31

2.3.2	Interactions Between Cylinder Triplets . . . . .	37
2.3.3	Hysteresis Between Cylinder Pairs . . . . .	40
2.4	Conclusion . . . . .	43
<b>3</b>	<b>Threshold-free characterization of local structure in amorphous materials</b>	<b>45</b>
3.1	Introduction . . . . .	46
3.2	Structural characterization . . . . .	46
3.3	Dependence on packing fraction . . . . .	49
3.4	Conclusion . . . . .	52
<b>4</b>	<b>Local dynamics and structure</b>	<b>55</b>
4.1	Introduction . . . . .	55
4.2	Global packing fraction . . . . .	56
4.3	Global forces . . . . .	57
4.4	Dynamics . . . . .	58
4.4.1	Particle velocities . . . . .	58
4.4.2	Spatial velocity variations . . . . .	58
4.5	Structure . . . . .	61
4.6	Comparison between structure and dynamics . . . . .	66
4.7	Indentation . . . . .	68
<b>5</b>	<b>Extended Dynamics</b>	<b>73</b>
5.1	Introduction . . . . .	73
5.2	Identifying shear bands . . . . .	74
5.3	Shear band angle . . . . .	76
5.4	Refining shear bands . . . . .	77
5.5	Comparison with structure . . . . .	79

5.6	Particle rotations . . . . .	82
5.7	Future work . . . . .	83
<b>6</b>	<b>Conclusion</b>	<b>88</b>
6.1	Summary . . . . .	88
6.2	Future directions . . . . .	90
<b>A</b>	<b>Experimental procedure and image analysis details</b>	<b>92</b>
A.1	Experimental details . . . . .	92
A.1.1	Initialization . . . . .	92
A.1.2	Running an experiment . . . . .	95
A.1.3	Data types . . . . .	96
A.2	Force sensor calibration . . . . .	96
A.3	Particle tracking codes . . . . .	97
A.4	Orientation codes . . . . .	98

# List of Figures

1	The responses of amorphous systems to imposed disturbances for a wide variety of materials over many length scales. Despite their differences, these materials have all experienced a highly-localized region of intense shearing and have developed shear bands. . . . .	2
1.1	Experimental setup. A nearby computer communicates with the CompactRIO (cRIO), which controls stepper motor movement and data acquisition from force sensors. A camera mounted above is also controlled with a nearby computer. . . .	8
1.2	Top-down view of the experimental apparatus. Stepper motor rotation results in the translation of the aluminum plate, which drives the suspended rod into the disordered granular pillar at a constant speed. The pillar is 2D, allowing for visualization of all grains throughout the deformation. Images are acquired from a camera mounted above while force sensor data is simultaneously recorded from sensors mounted to the aluminum plate as well as those mounted to the side of the surrounding box. . . . .	10

1.3	Force as a function of time required to push a wedge of grains (shown in the inset) along the substrate. The wedge is placed between clamps at the compressing bar so that there is no relative particle motion inside the wedge. Using the known masses of the grains, we are able to estimate the coefficient of kinetic friction between the grains and the substrate. . . . .	11
1.4	Top-down view of the experimental apparatus for indentation into a granular packing. Stepper motor rotation results in the translation of the aluminum plate, which drives the wedge into the disordered granular pillar at a constant speed. The packing is confined on three sides by an aluminum frame. Two dimensionality allows for the visualization of all grains throughout the deformation. Images are acquired from a camera mounted above while force sensor data is simultaneously recorded from sensors mounted to the aluminum plate as well as those mounted to the side of the surrounding box. . . . .	12
1.5	Steps for identifying particle positions. a) Raw image, b) gradient of raw image, c) gradient image with detected edges superimposed, d) distance map determined from edges, e) distance map convolved with cone, f) peak determination from paraboloid estimates, g) final result. . . . .	14

- 1.6 Steps for identifying particle orientations. a) A single particle, initially (top image) and at some later time,  $t$  (bottom image), contrast-enhanced so that lines drawn on particles are more visible. b) Top: horizontal white line with similar dimensions to the lines drawn on particles, used to determine initial (absolute) orientation. Middle and bottom: further processing of boxed regions in a), resulting in the isolation of the lines drawn on particles. c) Magnitudes of  $2D$  polar Fourier transforms for adjacent image in b). Orientational changes in the lines correspond to horizontal shifts in these images. d) Top: cross-correlation between top two images in c), summed over  $\tilde{r}$ . The angle at which there is a peak in the cross-correlation (blue) identifies the relative orientational shift between the two images. A parabola (red) is fit to the curve near the peak to improve the estimation of this angle (green). Bottom: cross-correlation between bottom two images in c). e) Final results. . . . 18
- 2.1 a) A pair of  $R = 3.175$  mm upright cylinders standing in mineral oil (dyed red) viewed from the side. b) Final Surface Evolver output for a pair of cylinders with similar conditions to a), also viewed from the side. c) Final Surface Evolver state for a group of three cylinders. The capillary rise reaches the tops of the cylinders at small separations, causing the resulting cohesive force between to be set by  $h$ , the exposed height of the cylinders above the liquid reservoir. . . . . 24

- 2.2 a) Top-down view of the setup for measuring cohesive forces between cylinder pairs (single white star in the upper right corner of the stationary block, as shown) and cylinder triplets (the stationary block is rotated  $180^\circ$  so that the two white stars are located in the upper right corner). This schematic not to scale: in the experiments, the entire apparatus measures 56 cm x 71 cm, each cylinder has radius  $R = 3.175$  mm and there are 15 cylinder pairs and 16 cylinder triplets. Another row of cylinders is glued to a rod suspended from a plate attached to a motor. The suspended cylinders are 1 mm above the base of the surrounding box. A known amount of mineral oil is added to the surrounding container for each set of experiments. Initially, the cylinders attached to the suspended rod are moved into contact with the cylinders attached to the stationary block, allowing capillary bridges to form between them. The suspended cylinders are then pulled away from the stationary cylinders. Lateral capillary forces resist this motion, causing the suspended rod to come into contact with and exert a force on the force sensors. b) Side view of the region enclosed by the dashed box in a). . . . . 26
- 2.3 a) Side view of a capillary bridge between two upright cylinders, where  $z_2$  is the equilibrium rise height for a fluid with contact angle  $\theta_c$  between two cylinders, each of radius  $R$ , with surface separation  $d$ . b) View of the horizontal slice in the  $z = z_2$  plane.  $R_2$  is the radius of curvature of the fluid free surface in this horizontal plane, and  $\alpha$  is the angle between the line connecting the centers of the cylinders and the line from the center of the cylinder to the contact line. . . . . 29

2.4	Experimentally measured attractive forces between cylinder pairs (circles) as a function of separation for many exposed cylinder heights, $h$ as labeled. Each curve is the result of averaging five experimental trials together. Raw data and the resulting average curve for $h = 16.3$ mm are shown in the inset. The uncertainty in the depth measurements is $\pm 0.7$ mm, and forces for $d < 80$ $\mu\text{m}$ are excluded because they cannot be measured reliably. Lines represent the result of a global fit of the model to the eight largest exposed cylinder heights. . . . .	33
2.5	Surface energies as a function of cylinder separation determined using Surface Evolver, using best-fit parameters from the model. Each data point (circle) corresponds to one simulation. The simulation data for each exposed cylinder height is fit to a smoothing spline (solid lines), which is then differentiated to determine the force of attraction between cylinder pairs as a function of $d$ , the separation of the cylinder surfaces. . . . .	34
2.6	Attractive forces between cylinder pairs: experimental measurements (circles), Surface Evolver energy derivatives (lines), and model calculations (squares) for three different liquid levels. The dashed line indicates force predicted by the model discussed in the Theoretical Model part of the Methods section for infinitely tall cylinders. Deviations from this line occur at small separations, $d$ , because the capillary rise has reached the tops of the cylinders. . . . .	35

2.7	<p>Experimental data for <math>h = 16.3</math> mm shown (circles) along with total predicted force from the model using best-fit parameters from the model (solid line). The total predicted force, given in Eq. (2.2.4), is the sum of three terms. The first term in Eq. (2.2.4) is the force contribution from the pressure inside the fluid (dashed line) and remaining two terms describe the surface tension force (dotted line). The force is dominated by pressure for small separations, while surface tension is more important for large separations. There is a cross-over in the dominant contribution to the total force around <math>0.5l_c</math>. The near-plateau at small separations, <math>d</math>, is due to the finite height of the cylinders. In this entire region, the capillary rise height reaches the tops of the cylinders, so the increase of force here is caused only by an increase in the thickness of the capillary bridge as the separation between the cylinders decreases. . . . .</p>	36
2.8	<p>a) Force vs separation for a group of three cylinders for many exposed cylinder heights, <math>h</math>. b) Experimental force data and Surface Evolver energy derivatives (using parameters from model fit) show reasonable agreement for three different <math>h</math> values. . . . .</p>	38
2.9	<p>Force vs separation data are shown for triplets (circles) for numerous exposed cylinder heights. Forces between triplets will have contributions from the two pair-wise interactions acting in the directions <math>\pm\phi(d)/2 = \pm\arctan(R/\sqrt{d^2 + 4Rd + 3R^2})</math> relative to the direction of separation as well as a contribution from a capillary rise that occurs in the middle of the three cylinders. Contributions expected from the two pairwise interactions (solid lines) account for nearly all of the measured triplet interactions. . . . .</p>	39

2.10	Measured force vs separation for cylinder pairs at different speeds for $h = 14.1 \pm 0.7$ mm. A direction-of-motion-dependent hysteresis is observed, the strength of which is dependent upon the speed of the motion. The top curves (circles) are measured when the cylinder separation is increasing and the bottom curves (squares) are measured as the cylinders are pushed together. Lines represent the average of five to fifteen experiments, and the size of the points is indicative of the uncertainty. In the inset, experimental data for the slowest speed is plotted along with six evaluations of the model. The best-fit force curves are shown as the solid lines. Both contact angle and $h$ are fit parameters for increasing separation data (circles). For the decreasing separation data, $h$ is fixed and contact angle is the only fit parameter. . . . .	41
3.1	a) Three particles inside Voronoi cells (blue) and the corresponding Delaunay triangulation (green). Local anisotropy is characterized by the vectors (magenta) pointing from each particle center (red circle) to each Voronoi-cell centroid. b) Zoomed-in region of a disordered packing with super-imposed Radical Voronoi tessellation (blue) and resulting triangulation (green). Center-to-centroid vectors (magenta) are elongated by a factor of eight for ease of visualization. . . . .	47
3.2	a) PDF of $Q_k$ for a bidisperse packing of hard spheres with particle size ratio 3: 4 (circles) and best-fit Gaussian (solid line). $Q_k > 0$ regions are more tightly packed than their surroundings, hence we call these regions overpacked. $Q_k < 0$ regions are more loosely packed than their surroundings, and are therefore labeled underpacked. b) PDFs of standard measures of free area fraction for the same packing. These distributions are more complicated and less intuitive than $Q_k$ . Inset: $Q_k$ correlates well with a fractional deviation from the global packing fraction, therefore is similar to a relative free area. . . . .	53

3.3	Average moments of $Q_k$ distributions as a function of global packing fraction, $\phi$ . In all plots, each data point represents the average value of the specified moment over several configurations, with the size of the point indicating the uncertainty in the average. The main plots show the low $\phi$ behavior, which approaches the same constant value for all preparation protocols shown: infinitely-fast quench ( $\times$ ), thermal ( $\circ$ ), randomly placed non-overlapping monodisperse circles ( $+$ ), and random point patterns (dashed line). Insets show behavior near $\phi_c$ for quenched ( $\times$ ) and thermalized ( $\circ$ ) configurations. Rescaled distributions of $\phi_c$ are plotted as the solid lines, with color indicating preparation protocol from which they were determined. a) Standard deviation vs $\phi$ . b) Skewness vs $\phi$ . Both preparation protocols in a) and b) have a kink in the data that coincides with the peak in the respective $\phi_c$ distribution. . . . .	54
4.1	Global packing fractions for 30 cohesive pillars and 30 submerged pillars as a function of time. Compression starts at $t = 0$ . . . . .	56
4.2	Global forces as measured from the moving end of the apparatus. Cohesive forces tend to be higher than the submerged forces. Numbered points correspond to times at which snapshots are shown in Fig. 4.3. . . . .	57
4.3	Snapshots of particle velocities for cohesive (top row) and submerged (bottom row). Colors indicate speed relative to the particle speed, $v$ , of the compressing bar, $v_c$ . $\Delta t$ indicates time in each experiment relative to the time at which contact between the compressing bar and the pillar is established. In both cohesive and non-cohesive (submerged) experiments, the deformation is spatially anisotropic. Sharp spatial gradients in the velocities occur (as in 2 and 5), though the precise locations fluctuate in time. . . . .	59

4.4	A single triangle with vertices given by particle centers. $u$ and $v$ represent $x$ and $y$ displacements of each vertex. Strains are determined by assuming these displacements represent a linearly-varying velocity field over the triangle. . . . .	60
4.5	Snapshot of dilation rates for cohesive (left) and submerged (right), calculated per triangle. $\Delta t$ indicates time in each experiment relative to the time at which contact between the compressing bar and the pillar is established. . . . .	61
4.6	Snapshot of deviatoric strain rates for cohesive (left) and submerged (right), calculated per triangle. $\Delta t$ indicates time in each experiment relative to the time at which contact between the compressing bar and the pillar is established. The sharp spatial gradients in the velocities are well captured by the deviatoric strain rates. . . . .	62
4.7	Snapshot of the experimental system with the radical Voronoi tessellation (blue) and the resulting generalized Delaunay triangulation (green). These networks provide a natural way to define a local free volume within the material, however, the free volume within a region tends to be distributed amongst several cells/triangles. Another more direct approach is to analyze closed loops in a particle graph or contact network (shaded magenta region), however, this requires precise information about particle contacts. . . . .	63
4.8	Contact network for a single snapshot of the experiment. Lines are drawn between Voronoi neighbors (i.e, any two particles that share an edge in the Voronoi tessellation), and are color-coded by particle-particle surface separation, up to 0.5 mm. Given the uncertainty in particle positions resulting from tracking error, we do not know precise contact information. As a result, we must choose a cutoff if we wish to proceed, and this figure indicates that our results will be quite sensitive to this cutoff. . . . .	64

4.9	<p>Snapshots of <math>D_k</math>, shown for both cohesive and submerged. A zoomed in region is shown so that details are more visible. The top of the box in each case is just below the compressing bar, and the box width is the entire pillar width. Regions with <math>D_k &lt; 0</math> (cyan) coincide with regions of locally higher free volume, and regions with <math>D_k &gt; 0</math> (magenta) coincide with regions of locally lower free volume. . . . .</p>	65
4.10	<p>Logarithm of two-dimensional PDF of relative free area vs <math>D_k = \vec{\nabla} \cdot \vec{C}</math>. Relative free area, defined per triangle, is given by the difference of area fraction of the central triangle and the average of the surrounding triangles. . . . .</p>	66
4.11	<p>PDFs of <math>D_k</math> for 30 cohesive (red) and 30 submerged (blue) experiments. The initial states (<math>\circ</math>) are defined as the prepared initial condition before compression starts. The deformed states (<math>\times</math>) only include information from triangles in which at least one particle has moved one radius. The static triangles are not included because the disturbance never reaches them. The dashed lines represent Gaussians described the the mean, <math>\mu</math>, and the standard deviation, <math>\sigma</math>, of each initial data set. As deformation proceeds, the tails of the distributions broaden. . . . .</p>	67
4.12	<p>Logarithm of the two-dimensional PDF of relative strain rate vs <math>D_k</math> for 30 cohesive experiments. . . . .</p>	69
4.13	<p>Relative deviatoric strain rate vs <math>D_k = \vec{\nabla} \cdot \vec{C}</math>. <math>D_k</math> is logarithmically binned, and data points represent the average relative strain rate within each bin. Vertical error bars represent the standard error of the mean of the relative strain rate within each bin, and horizontal error bars represent bin widths. Each bin contains at least 100 data points, and these curves contains data from 30 experiments. . . . .</p>	70
4.14	<p>Particle velocities for indentation experiments into dry granular packings. Indenter angles are <math>45^\circ</math> for the experiment shown in the left column <math>90^\circ</math> for the experiment shown in the right column. . . . .</p>	71

4.15	Relative strain rate as a function of $D_k$ . $D_k$ values are divided into logarithmically-spaced bins, each of which contains at least 100 data points. Relative strain rates for 5 experiments at each indenter angle are averaged within each $D_k$ bin, shown as circles in the plot. Standard error of the mean for within each bin are shown as vertical errorbars, and horizontal errorbars show bin width for each $D_k$ bin. . . . .	72
5.1	Interpolated fields on top of the experimental image. a) $D_k$ , b) deviatoric strain rate, and c) both $D_k$ and deviatoric strain rate. A transient shear band winds through the packing, connecting several underpacked regions while largely avoiding the overpacked regions. . . . .	74
5.2	Interpolated deviatoric strain rate field with regions of interest shown as dashed lines. Left and right sides are treated independently throughout the analysis. . . . .	75
5.3	Steps to identify a single shear band at each point in time from the interpolated deviatoric strain rate field. a) Interpolated field. b) Two-dimensional spatial cross-correlation of interpolated field. Preferred directions of shear, if present, appear as extended bands in the spatial cross-correlation. c) Radon transform of spatial cross-correlation, the peak of which identifies the strongest line in b). d) Spatial cross-correlation with line identified from Radon transform overlaid. e) Radon transform of the image in a). This is used to locate the position of the shear band, given the orientation determined in c). f) Identified shear band overlaid on top of initial image. . . . .	77

5.4	Average shear band angles identified independently for left and right sides of the pillar as well as cohesive and non-cohesive experiments. The color in the images represents the averaged two-dimensional spatial cross-correlation for 30 experiments each, with at least 200 time data points per experiment. The orientation of the most extended feature is determined using the Radon transform, as explained in Fig. 5.3. Around 10 points surrounding the peak in the Radon transform are fit to a function of the form $y = a(x - x_0)^2 + b$ , with $\theta = 90^\circ - x_0$ . Bounds shown for $\theta$ are given by the 95% confidence intervals on the fit parameter $x_0$ . . . . .	78
5.5	Color in all images indicates deviatoric strain rate, and magnitude is given by the color bar in the bottom right of the figure. a) A curved transient shear band with strongest angle identified. b) Image in a) rotated by previously identified band angle. Previously-identified band location is shown as the black line. In this rotated frame, the maximum deviatoric strain rate is identified for each column, overlaid as the white dots, and the resulting group of points is then Gaussian-smoothed, shown as the red curve, with a filter window of a large particle radius. c) Integral of strain along paths parallel to the band, as a function of perpendicular distance to the band. The band width is estimated by finding the full width at half the maximum value d) Final result. . . . .	80
5.6	Examples of shear band identification method failing. In the picture on the left, there are multiple bands, so the assumption that there is only one is not valid. In the picture on the right, there is no band, so again the assumption that there is one shear band is incorrect. . . . .	81

5.7	Top left: interpolated deviatoric strain rate field, with the identified transient shear bands overlaid. Top right: $D_k$ field with shear band superimposed on top of the field. Lower plot: average of $\dot{J}_2$ and $D_k$ along paths parallel to shear band, as a function of perpendicular distance from the band. The maximum shear location coincides with a local minimum in the values of $D_k$ , supporting the idea that bands tend to avoid locally overpacked regions. . . . .	82
5.8	25 snapshots of deviatoric strain rate fields from 15 experiments. Identified band is overlaid on top of each image, and images were manually selected as having strong shear bands. . . . .	83
5.9	$D_k$ fields corresponding to the 25 snapshots in Fig. 5.8. Bands identified from strain rate are overlaid in red. . . . .	84
5.10	The green curve shows the average strain rates (in units of $s^{-1}$ ) of 25 shear bands as a function of perpendicular distance to each band. As expected, there is a peak in this curve at $x_{\perp} = 0$ . The blue curve shows the average $D_k$ field integrated along the bands. The shading around the each curve represents the standard error of the mean. There is a minimum in $\langle D_k \rangle$ that coincides with the maximum strain rate, suggesting that paths with more negative $D_k$ regions may be favored for shear bands. . . . .	85
5.11	Particle rotation rates for 17 points in time for which there is a shear band, interpolated onto a field. Identified shear band is super-imposed on top of each field. . . . .	86
5.12	The green curve shows the average strain rates of 17 as a function of perpendicular distance to each band. The blue curve shows the average of the magnitude of rotation rate field integrated along the bands. The shading around the each curve represents the standard error of the mean. There is a maximum in the magnitude of the rotation rates that coincides with the maximum strain rate, suggesting particles tend to rotate more inside shear bands. . . . .	87

A.1	Project explorer for RunMotorAndRecordForceDataTrigger.lvproj, the LabVIEW project that controls the experiment. The two .vi files needed to control the experiment are highlighted. . . . .	93
A.2	Two custom LavVIEW files required for data acquisition. User inputs are boxed in red. . . . .	94
A.3	Project explorer and .vi files needed to calibrate force sensors. . . . .	97
A.4	NI-9949 RJ50 screw terminal adapters. Omega LCEB mini-beam load cells attach to the terminals in the following way: green wire → 2, white wire → 3, red wire → 6, black wire → 7. . . . .	98
A.5	Code tree showing the main particle tracking function, trackEntireRun60mm.m, as well as functions called within the main function. . . . .	99
A.6	Code tree showing the main orientation identification function, findParticleOrientationsNew.m, as well as functions called within the main function. . . . .	99

# Introduction

Amorphous packings make up a broad class of materials whose defining characteristic is that the constituent components lack any underlying long-range structural order. Despite the ubiquity of these materials, spanning system sizes from nanometer-scale metallic glasses to macroscopic systems such as sands, soils, and rocks, present knowledge of how loading-induced deformation proceeds is rather limited. While these materials can be quite strong, when they do yield, deformation is often highly localized, and, as is the case in the examples in Fig. 1, can be catastrophic for the material [21, 29, 36, 83].

The presence of these highly localized deformations, or shear bands, has been explored in a variety of systems. In experiments in which an intruder is dragged through a granular bed, Gravish *et al.* [35] found the formation of shear bands to be dependent upon the packing fraction of the grains. In compressed granular soil columns, Oda and Kazama [67] found that large voids are created within the band. More recent experiments by Hall *et al.* [37] have used X-ray tomography to see inside a compressed soil column and developed image processing techniques that identify most of the particles within the column. While this is substantial progress, a full understanding of shear band formation is much more difficult without having complete knowledge of internal structure. Recent experiments by Strickland *et al.* [90, 91] quasi-statically compress a pillar composed of colloidal particles. They find that shear band formation is sensitive to the liquid content within the pillar. In experiments in which a thin film of nanoparticles is slowly

indented, shear band formation was found to depend strongly on the aspect ratio of the particles in the thin film [105]. In compressed metallic glasses, shear band formation has been found to depend on system size [101], though this is complicated as this dependence is convolved with a dependence on the compliance of the machine performing the compression tests [39]. Despite this substantial progress in understanding shear band formation, an understanding of how individual grain-scale structure and dynamics give rise to this global failure in the material is incomplete.

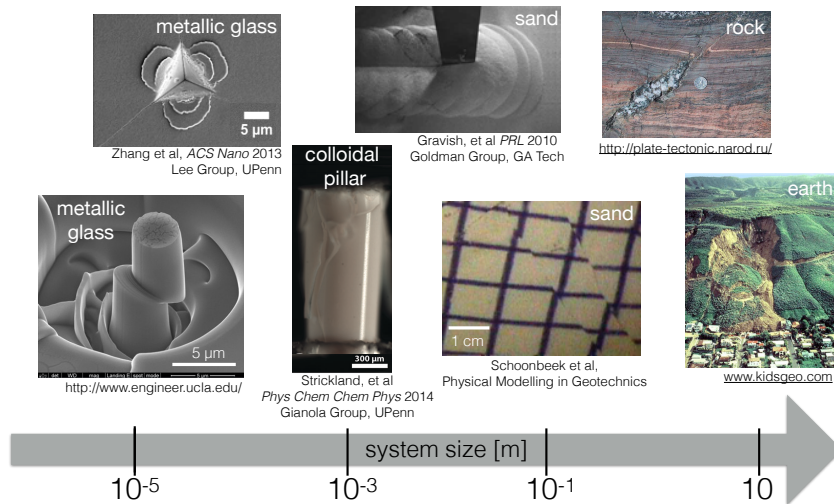


Figure 1: The responses of amorphous systems to imposed disturbances for a wide variety of materials over many length scales. Despite their differences, these materials have all experienced a highly-localized region of intense shearing and have developed shear bands.

Local rearrangements often precede this large-scale deformation [2, 28], though identifying where within the material these local structural reconfigurations are likely to occur *a priori* has proven challenging, making it difficult to predict where these materials will fail. Recently, Manning and Liu [60] found that local rearrangements in sheared packings of soft particles are preferentially initiated at locations for which vibrational modes have zero frequency. These *soft spots* identify regions the packing that are susceptible to flow and are analogous to dislocations in crystals. Cubuk, *et al.* [20] extended this idea to rigid-particle systems by employing machine-learning techniques

to identify soft spots in terms of numerous structural functions. They find that only a handful of functions are necessary to explain most of the observed dynamics during deformation. These results are promising, suggesting that structural signatures of weakness do indeed exist. However, the picture is incomplete as an understanding of which soft spots will undergo rearrangement and how they evolve and interact with each other to give rise to global failure is missing.

To explore the relation between local structure and dynamics in an amorphous system experimentally, we designed a custom apparatus in which a granular packing is subjected to quasi-static uniaxial compression. This geometry was chosen for its similarity to geometries used to probe material strength for a variety of systems including metallic glasses [18, 36], colloidal pillars [90, 91], packings of sand [54, 55], and soil columns [37]. Unlike these systems, our experiments are two dimensional, which allows for easy visualization of all grains within the material as it deforms and makes the direct comparison between local structure and dynamics possible. The details of the experimental setup as well as image processing techniques developed to identify grain positions are the focus of Chapter 1.

Another benefit of the two-dimensional system is that we can introduce uniformly-distributed grain-grain interactions by adding a fluid, allowing us to explore deformation as a function of grain-grain interactions. Our grains are upright cylindrical rods, and when the grain separation is small, capillary forces pull the liquid up between the grains. Near contact, this liquid column reaches the tops of the grains, allowing the interaction to be tuned by depth of the liquid. These cohesive interactions are characterized in Chapter 2. We measure the force required to quasi-statically separate pairs of grains experimentally as a function of liquid depth, and we developed a theoretical model by extending the ideas of Princen [73] to explain the origin of these forces. Finally, we investigate these forces numerically using Surface Evolver [9, 14], a finite element modeling software package designed to minimize the energy of the fluid surface for any input geometry subjected to user-specified physical constraints. All measures of forces are shown to be in excellent agreement.

In Chapter 3, we introduce a new measure of structural anisotropy in disordered materials. Starting from a generalized Voronoi tessellation [3, 32, 33, 44], we define a vector field that points from each particle center to each Voronoi cell centroid. These vectors point toward regions that are underpacked relative to the local surroundings and away from regions that are relatively overpacked, which leads us to look at the divergence of these vectors. The distribution of divergences within a packing is nearly Gaussian, so we explore how the moments of the distribution vary with area fraction in simulated bidisperse packings of soft spheres. We see a kink in these moments that coincides with the jamming transition, suggesting, as others have [64], that a purely geometrical signature of jamming exists.

We explore the relation between local structure within the pillar to the observed dynamics in Chapter 4. Local structure is characterized using the new measure introduced in Chapter 3, and local dynamics are characterized by the deviatoric strain rate, which is the second invariant of the local strain rate tensor. We find a statistical correlation between the local structure and dynamics that is consistent with our intuition: locally overpacked regions tend to experience lower strain rates while locally underpacked regions tend to experience higher strain rates. This correlation is stronger for cohesive packings. Preliminary results are also included from experiments imposing a more localized disturbance by quasi-statically indenting the packing with a wedge. Only non-cohesive systems have been explored, but the size of the disturbance has been varied by changing the angle of the wedge. We see a similar correlation between structure and dynamics in these experiments, with the larger wedge angle producing a stronger correlation.

Extended regions of intense shear are nicely highlighted by the deviatoric strain rate. Chapter 5 focuses on identifying these bands and comparing extended dynamics and structure. Unlike the examples shown in Fig. 1, the shear bands we observe do not persist in the same location, but rather move around throughout the deformation. Similar transient shear bands have been observed before [52, 54, 55], and have been shown to precede permanent shear bands in some experiments [54, 55]. Results presented in Chapter 5 are preliminary but suggest that the path the shear band

takes through the material contains more underpacked regions than other parallel paths in the vicinity of the band.

Finally, Chapter 6 summarizes the main results presented within this thesis and some ideas for future directions. Appendix A provides step-by-step instructions for running experiment along with detailed instructions for using custom-written programs to identify particle centers and orientations.

# Chapter 1

# Experimental Setup and Image Analysis

## 1.1 Introduction

This chapter begins with a detailed description of the general experimental setup for deforming two-dimensional disordered granular materials, followed by two specific deformation geometries explored in the remainder of this thesis. These specific geometries are chosen because they are commonly used in testing the mechanical response of metallic glasses to a well-controlled quasi-static deformation.

We choose two-dimensional granular materials so that we can identify all particles within the material. A camera captures images throughout the experiment. Image processing methods developed to extract particle information from the images is the topic covered in the remainder of this chapter. The resulting measurements provide the starting point for all subsequent analysis, so it is worth emphasizing that the quality of the image limits the amount and reliability of extracted information.

## 1.2 Experimental setup

The experimental setup is shown in Fig. 1.1. A National Instruments CompactRIO 9074 control most of the experiment. This CompactRIO chassis has 8 slots, each of which can accommodate one module. Numerous modules exist with a wide range of desirable functions. A CompactRIO with modules can operate as stand-alone computer if the field-programmable gate-array (FPGA) is configured and deployed, making it a very powerful and versatile tool. In experiments presented in this thesis, however, we operate only in Scan Engine mode, which allows for experimental control from Labview on a computer connected to the CompactRIO via an ethernet cable.

We use two modules for this experiment, one to control the motor and one to record readings from four force sensors. Motor movement is achieved using the National Instruments NI-9512 stepper driver interface module, which transmits instructions to the one-axis stepper motor driver, a National Instruments NI P70360. Necessary information is subsequently passed along to the stepper motor and results in rotation of the motor head. The DC power supply provides an extra 24 V to the NI-9512 necessary to control the motor. Acquisition of force sensor data is performed using a National Instruments NI-9237 analog input module, which reads the output signal from four Omega Engineering LCEB-5 mini-beam load cells.

A JAI/Pulnix TM-4200CL camera, mounted above the apparatus captures 4 MP 8-bit images at 8 Hz. Image acquisition is controlled via LabView on a nearby computer with a camera link connection between the camera and a NI PCIe-1433 frame grabber. Images are saved onto a solid state hard drive, and to ensure that no frames are dropped, images are streamed into container .avi files instead of individually written to the drive. An SMB signal from the frame grabber to the CompactRIO at the start of every new image capture triggers the recording of a simultaneous measurement from all four force sensors and synchronizes the acquisition of force and image data. See Appendix A.1-A.2 for further details on running experiments.

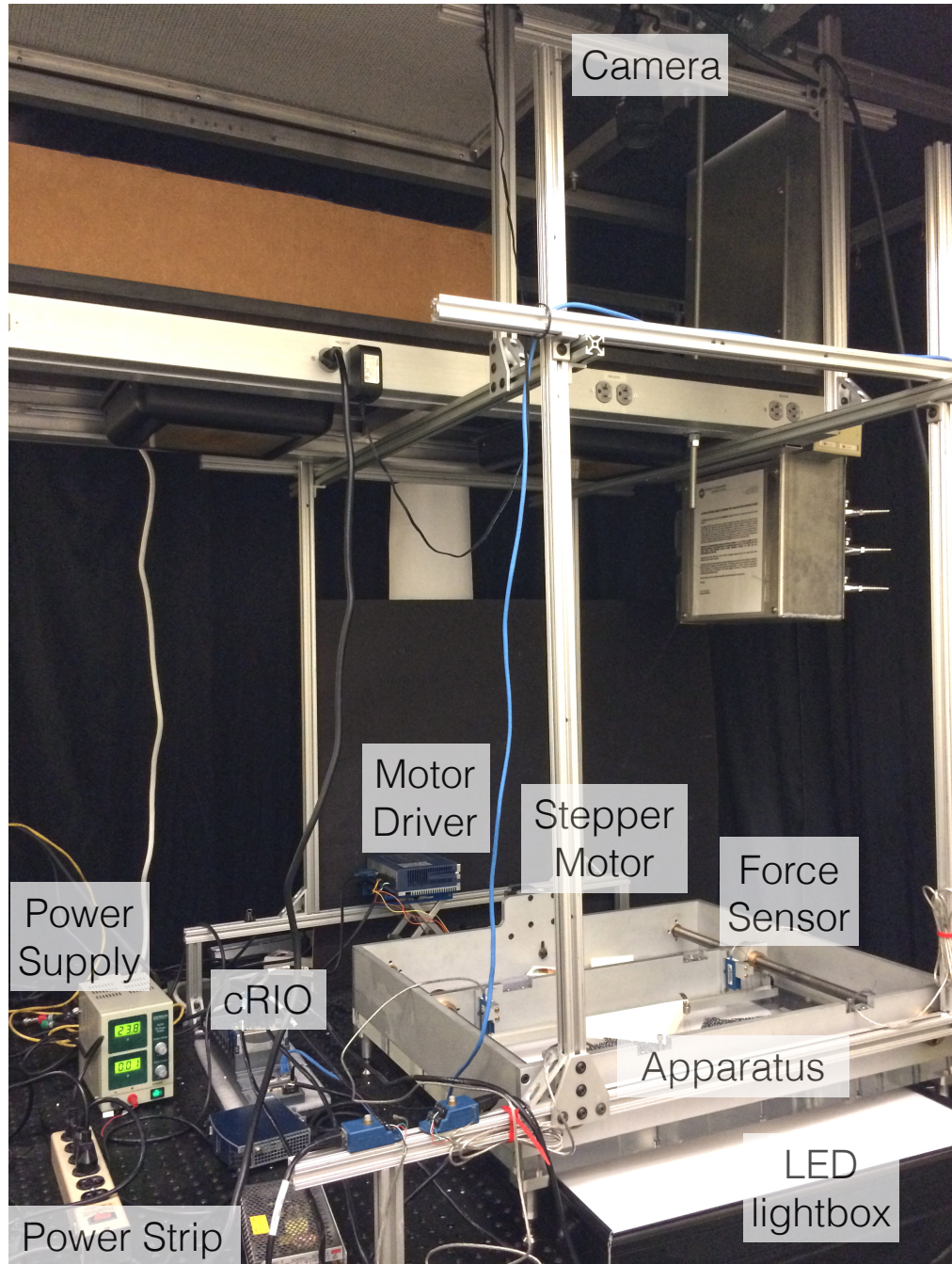


*Figure 1.1: Experimental setup. A nearby computer communicates with the CompactRIO (cRIO), which controls stepper motor movement and data acquisition from force sensors. A camera mounted above is also controlled with a nearby computer.*

### 1.2.1 Compression of two-dimensional granular pillars

A 2D granular pillar is created inside a large box, roughly  $60 \times 70$  cm, which sits horizontally on an optical table, see Fig. 1.2. Two threaded rods are affixed to the edges of this box with only the freedom to rotate. This rotation is driven by a stepper motor and results in the translational motion of an aluminum plate held by the rods. Deformation of the pillar begins when a suspended rod, which hangs from brackets mounted to the aluminum plate, is driven into the packing. Throughout the deformation, forces imposed by the driven suspended rod are measured as this rod is pushed by the packing into two force sensors mounted to the aluminum plate. In a similar setup at the static end of the pillar, a suspended rod is pushed into the two force sensors mounted to the surrounding box, allowing for the measurement of the forces transmitted through the pillar during the deformation. An LED lightbox illuminates the pillar from beneath the clear acrylic base of the box and provides uniform, constant lighting.

Grains within the pillar are cylindrical acetal dowel pins, standing upright on the base of the box so that only the tops of the grains are visible in Fig. 1.2. The pillars are bi-disperse with small grain diameter 4.8 mm, large grain diameter 6.4 mm, and all grain heights 19.05 mm. The grains have masses of around 0.46 g for small grains and 0.82 g for large grains. The base of the box is a large acrylic sheet, and we estimate the kinetic friction between the substrate and the grains by recording the force required to push a wedge of grains along the substrate, as shown in the inset of Fig. 1.3. We estimate that the coefficient of kinetic friction between the grains and the substrate is  $\mu_{meas} = 0.23 \pm 0.01$ .

To ensure similar initial conditions across experiments, pillars are manually forced to conform to the shape and size of a rigid frame. The pillar shown inside the apparatus in Fig. 1.2 is representative of the initial conditions created with this method. For experiments presented in this thesis, the ratio of initial pillar height,  $H_0$ , to initial width,  $W_0$ , is 2. Once a pillar has been created, the stepper motor drives the aluminum plate at a constant speed  $v_c = 0.085$  mm/s.

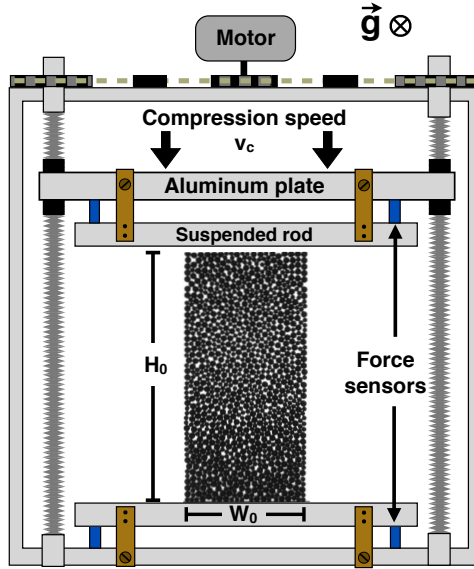


Figure 1.2: Top-down view of the experimental apparatus. Stepper motor rotation results in the translation of the aluminum plate, which drives the suspended rod into the disordered granular pillar at a constant speed. The pillar is 2D, allowing for visualization of all grains throughout the deformation. Images are acquired from a camera mounted above while force sensor data is simultaneously recorded from sensors mounted to the aluminum plate as well as those mounted to the side of the surrounding box.

Images and force sensor readings are acquired simultaneously throughout the compression at 8 Hz. Cohesive interactions can be introduced and tuned by adding a liquid into the surrounding container. These cohesive interactions are described in detail in the next chapter.

### 1.2.2 Indentation of two-dimensional granular pillars

The setup for indentation, shown in Fig 1.4, is similar to that of compression. A granular packing of desired dimensions is created with the help of a rigid frame. Unlike the compression experiments, the frame in indentation experiments is not removed prior to deformation. Rotation of stepper motor drives the translational motion of an aluminum plate toward the packing. A rod suspended

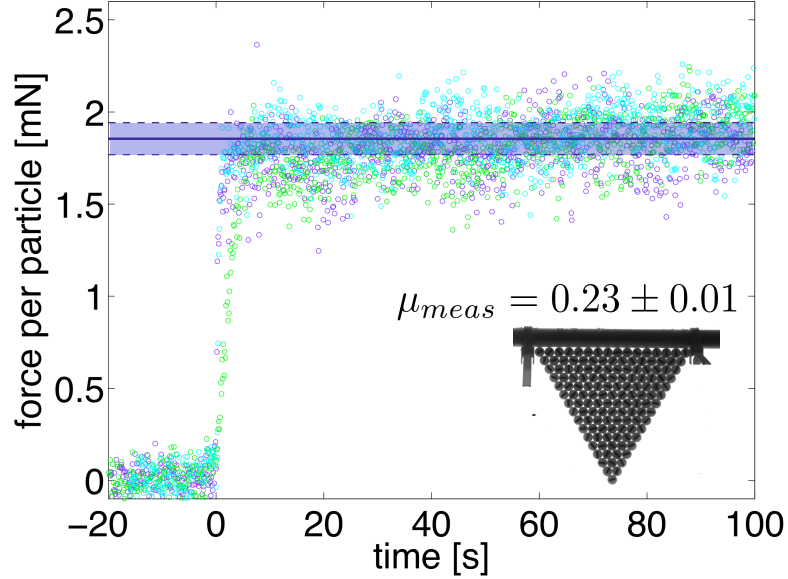


Figure 1.3: Force as a function of time required to push a wedge of grains (shown in the inset) along the substrate. The wedge is placed between clamps at the compressing bar so that there is no relative particle motion inside the wedge. Using the known masses of the grains, we are able to estimate the coefficient of kinetic friction between the grains and the substrate.

from the aluminum plate pushes a wedge into the grains, driving the deformation. The size of the disturbance is explored by varying the angle of the wedge, and, as with compression, particle interactions are tuned via capillary forces. Force sensors provide information about forces imposed onto the packing as well as those transmitted through the packing.

### 1.3 Image analysis

Images are grayscale 8-bit, 4 mega-pixel digital photographs acquired with a Pulnix TM-4200CL camera at 8 Hz. A 2D granular packing is illuminated from beneath with an LED light-box, which provides temporally constant and spatially uniform lighting. Particles are white cylindrical rods standing on end so that primarily the tops are visible in the images. The tops painted black to enhance the contrast between the sides and the tops of the grains, which is especially helpful when

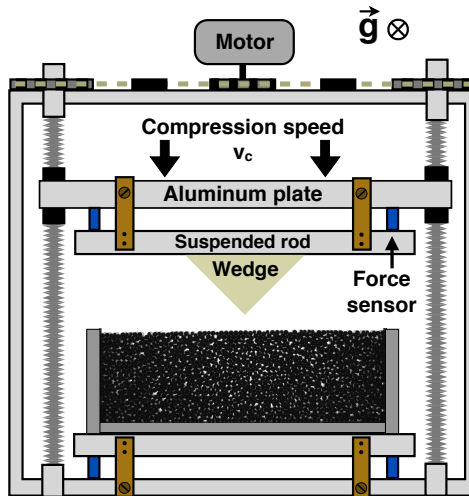


Figure 1.4: Top-down view of the experimental apparatus for indentation into a granular packing. Stepper motor rotation results in the translation of the aluminum plate, which drives the wedge into the disordered granular pillar at a constant speed. The packing is confined on three sides by an aluminum frame. Two dimensionality allows for the visualization of all grains throughout the deformation. Images are acquired from a camera mounted above while force sensor data is simultaneously recorded from sensors mounted to the aluminum plate as well as those mounted to the side of the surrounding box.

fluid is added to make the packing cohesive. Image clarity is further improved by using a Nikon 60mm f/2.8D AF Micro-Nikkor lens, a high-quality macro lens designed to enhance the sharpness of image features. All feature detection and image analysis is built upon the built-in codes in MATLAB Image Processing Toolbox.

### 1.3.1 Particle centers and velocities

The steps of particle center identification are outlined in Fig. 1.5. Starting from the initial image, an example of which is shown in Fig. 1.5a, we first compute the image gradient using the Prewitt gradient operator. [72] This method estimates the magnitude of the gradient of an image by convolving two  $3 \times 3$  kernels with the original image, one for variations in  $x$  and one for  $y$ , and taking the norm of the two convolutions. The gradient image is then converted to an 8-bit image, as shown in Fig. 1.5b. We find that performing analysis on the image gradient produces cleaner results than operating on the original image directly.

Canny edge detection [15] is a robust way of finding edges in an image over a wide range of intensity variations, and is the next step in our particle identification. This method computes the gradient of the image after smoothing with a Gaussian of width  $\sigma$ , then locates features with local intensity above an input threshold. For our images, parameter choices that work well are  $\sigma = \sqrt{2}$  and a threshold in the range of 0.15 to 0.2. The result is a binary image of edges, which have been identified and plotted in red on top of the gradient image in Fig. 1.5c.

We then compute the distance map of the binarized edges, which sets each pixel value based on the distance to the nearest white pixel. The result is shown in Fig. 1.5d. The center of a circular particle is maximally far away from all edges, therefore the peak of the distance map coincides with the particle centers. The distance map varies linearly with distance away from a white pixel, so for circular particles, the distance map profile is that of a right circular cone. The position of the cone apex provides the location of the particle center with pixel-scale resolution, and the height of the apex is related to the particle radius, though given that we have operated

on the gradient of the image, this height always underestimates the radius. We use this number to classify the particle as large or small, and then assign the radius from an independent calibration of the pixel-to-cm conversion.

To achieve sub-pixel accuracy in positions, we first convolve the distance map with a right circular cone, see Fig. 1.5e. The resulting profile is a paraboloid, as shown in Fig. 1.5f. To reduce computational time required, instead of locally fitting the profile peak to a paraboloid, we use subsets of data surrounding the peak to determine paraboloids described by each subset. Six points are needed to define a paraboloid, so the subsets used are defined by the center pixel, the closest four surrounding pixels, and one diagonal pixel within the  $3 \times 3$  region surrounding the central pixel, see Fig. 1.5f. The positions of the global maxima for the four resulting paraboloids are averaged to identify the peak location, shown in magenta in Fig. 1.5f. Variation of positions from 1000 images of stationary particles is  $\sim 0.05$  pixels  $\approx 0.003R$ .

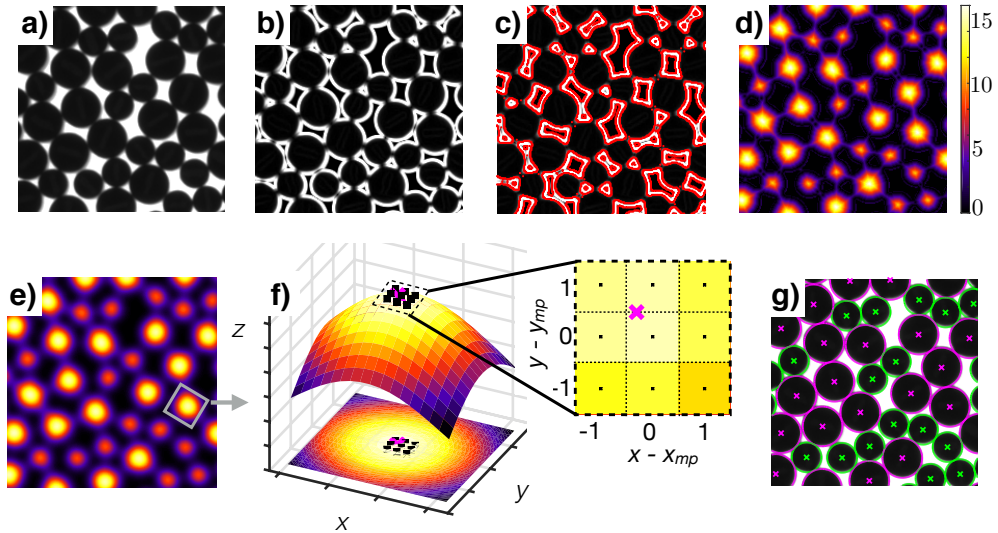


Figure 1.5: Steps for identifying particle positions. a) Raw image, b) gradient of raw image, c) gradient image with detected edges superimposed, d) distance map determined from edges, e) distance map convolved with cone, f) peak determination from paraboloid estimates, g) final result.

After particles in each image are identified individually, they are temporally connected by

comparing the positions between a given frame and the subsequent frame. Given that the imaging rate is much faster than the observed dynamics, it is sufficient to link particles in subsequent frames using only information center-to-center distance. There is typically only one choice within  $0.5R$  of each particle in two subsequent images. Although there is never more than one choice, occasionally, no matching particles are identified. In this situation, the last known position is compared with future images within a time window corresponding to particle motion on the scale of  $0.5R$ . If the particle is identified again later within this window, the positions are linearly interpolated to fill in the missing data points. If the particle is not located again within this time window, the track is truncated at the last known position. Once positions for each particle are linked, the time trace is smoothed by convolving with a Gaussian of a chosen temporal width, which typically corresponds to the amount of time associated with particle motions of around  $0.1R$ . Instantaneous velocities are estimated by differentiating these smoothed positions, and then retaining only one data point per time window. See Appendix A.3 for further details on particle tracking.

For image acquisition rates more comparable to the timescale of dynamics, a more sophisticated linking method is needed. One way to tackle this issue is to search not only in the neighborhood of the particle, but also to use velocity information and search for matches in the neighborhood of the projected position [68].

### 1.3.2 Particle orientations and angular velocities

White lines are drawn on the tops of the particles, allowing for the measurement of particle orientations and rotations. To identify these lines, we start by performing a local contrast enhancement on the each image, using the MATLAB implementation of the Contrast-Limited Adaptive Histogram Equalization (CLAHE) method. The result, as shown for one particle at two different times in Fig. 1.6a, is that the relative contrast between the dark particle top and the white line is greatly increased.

Next, a region of interest is taken surrounding each previously-identified particle center and placed into a new image that was originally defined to be all zeros. Each region is defined by a square box with edge length  $1.1R$ , and the region is placed so that its center in the new image corresponds to the particle center in the original image, rounded to the nearest pixel. This region is chosen to be large enough to include as much of the line as possible while being small enough to exclude all background lighting. After regions surrounding all centers have been placed into this new image, an H-minima transform is performed on this new image, reducing the depth of all local minima by as much as height  $h$ , an input parameter. The result is that all local minima with depth less than  $h$  are entirely suppressed, so  $h$  is chosen based on the scale of intensity fluctuations to be eliminated. Given that the lines are the brightest feature in this new image, these will be the last features to be suppressed by the H-minima transform. A value of  $h = 25$  works well for our new images. The transformed image is then rescaled so that the pixel intensity values in the image span the entire 8-bit range, then the image is converted to an 8-bit image. Two examples of the final result are shown in the bottom two pictures in Fig. 1.6b.

The absolute orientation of each particle is determined by comparing the initial enhanced line to a binary image of horizontal line of similar width and length, such as the one shown in the top image in Fig. 1.6b. After that, the relative rotation of a given particle is determined by comparing the enhanced line in the initial image, i.e, the middle image in Fig. 1.6b to the enhanced lines of the particle in subsequent images, i.e, the bottom image in Fig. 1.6b. We find that comparing the enhanced line with a rotated and translated version of itself produces better results than comparing the orientation at each time step with that of the horizontal line.

To make the comparisons between the enhanced lines in images  $A$  and  $B$ , between which the enhanced line has experienced a relative translation of  $(x_{AB}, y_{AB})$  and a relative rotation of  $\theta_{AB}$ , we employ a method developed previously [6, 22, 78, 102], which is built upon the fact that the

two-dimensional Fourier transforms of the respective images,  $\mathcal{F}_A(\tilde{x}, \tilde{y})$  and  $\mathcal{F}_B(\tilde{x}, \tilde{y})$ , are related:

$$\mathcal{F}_B(\tilde{x}, \tilde{y}) = e^{-2\pi i(\tilde{x}x_{AB} + \tilde{y}y_{AB})} \mathcal{F}_A(\tilde{x} \cos \theta_{AB} + \tilde{y} \sin \theta_{AB}, -\tilde{x} \sin \theta_{AB} + \tilde{y} \cos \theta_{AB}). \quad (1.3.1)$$

Notice that the translational component,  $(x_{AB}, y_{AB})$ , is completely contained within the phase of this complex number. Thus, by looking at the amplitude of Eq. 1.3.1, which only depends on the magnitude of the  $2D$  Fourier spectra for images  $A$  and  $B$ ,  $\mathcal{M}_A(\tilde{x}, \tilde{y})$  and  $\mathcal{M}_B(\tilde{x}, \tilde{y})$ , we can isolate the rotational alignment from the translational alignment. In polar coordinates, this becomes

$$\mathcal{M}_B(r, \theta) = \mathcal{M}_A(r, \theta - \theta_{AB}). \quad (1.3.2)$$

To compute the  $2D$  polar Fourier transform exactly and efficiently, we take advantage of the projection-slice theorem, which states that taking the  $1D$  Fourier transform of a  $2D$  function,  $I(x, y)$  (in our case, an image) projected onto a line oriented at an angle  $\phi$  is equivalent to taking a slice through the  $2D$  Fourier transform that passes through the origin as is oriented at angle  $\phi$ . Projecting  $I(x, y)$  onto a line oriented at an angle  $\phi$  is precisely the Radon transform, given by

$$R(r, \phi)[I(x, y)] \equiv \int_{-\infty}^{\infty} \int_{-\infty}^{\infty} I(x, y) \delta(r - x \cos \phi - y \sin \phi) dx dy. \quad (1.3.3)$$

Taking the  $1D$  Fourier transform of  $R(r, \phi)$  for each  $\phi$  yields the  $2D$  polar Fourier transform of  $I(x, y)$ . Recall that, in order to determine the relative orientational shift between a feature in two images, the magnitudes of these Fourier transforms,  $\mathcal{M}_A$  and  $\mathcal{M}_B$ , are sufficient. Examples of  $\mathcal{M}$  for the images in Fig. 1.6b are shown in Fig. 1.6c. The relative rotation of a feature between two images will result in a relative translational shift along the  $\tilde{\theta}$  axis in the magnitudes of the Fourier transforms, therefore we compute the cross-correlation of  $\mathcal{M}_A$  and  $\mathcal{M}_B$ , integrating over  $\tilde{r}$ :

$$C_{AB}(\theta) = \text{Re} \left\{ \mathcal{F}_1^{-1} \left[ \int \mathcal{F}_2 \{ \mathcal{M}_A(r, \theta) \} [\tilde{r}, \tilde{\theta}] \times \mathcal{F}_2^* \{ \mathcal{M}_B(r, \theta) \} [\tilde{r}, \tilde{\theta}] d\tilde{r} \right] [\theta] \right\}. \quad (1.3.4)$$

$\mathcal{F}_1^{-1}$  is a inverse  $1D$  Fourier transform and  $\mathcal{F}_2$  is a  $2D$  Fourier transform. Examples of  $C(\theta)$  are shown in Fig 1.6d: the top curve is the cross-correlation between the top two images in Fig. 1.6c and the bottom curve is the cross-correlation between the bottom two images in Fig. 1.6c. The

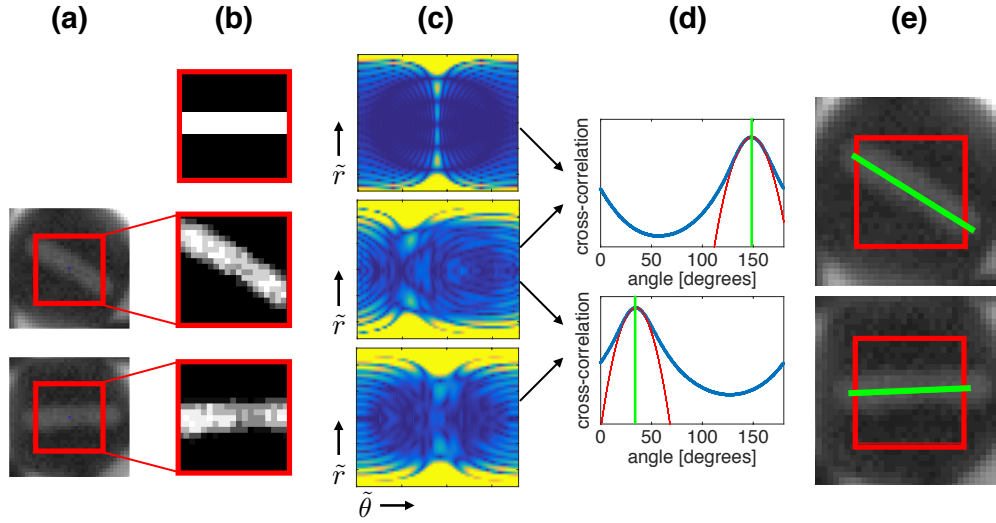


Figure 1.6: Steps for identifying particle orientations. a) A single particle, initially (top image) and at some later time,  $t$  (bottom image), contrast-enhanced so that lines drawn on particles are more visible. b) Top: horizontal white line with similar dimensions to the lines drawn on particles, used to determine initial (absolute) orientation. Middle and bottom: further processing of boxed regions in a), resulting in the isolation of the lines drawn on particles. c) Magnitudes of 2D polar Fourier transforms for adjacent image in b). Orientational changes in the lines correspond to horizontal shifts in these images. d) Top: cross-correlation between top two images in c), summed over  $\tilde{r}$ . The angle at which there is a peak in the cross-correlation (blue) identifies the relative orientational shift between the two images. A parabola (red) is fit to the curve near the peak to improve the estimation of this angle (green). Bottom: cross-correlation between bottom two images in c). e) Final results.

orientational shift,  $\theta_{AB}$ , between images  $A$  and  $B$ , is defined as the angle at which the cross-correlation is maximized. We improve our estimate of this angle by locally fitting a parabola to  $C(\theta)$  near the peak, shown in the plots as the red curves. The final identified orientations are shown as the green lines in Fig. 1.6e. Uncertainty in identified orientations for 1000 stationary frames is about  $0.5^\circ$ .

Note that there is a  $180^\circ$  degeneracy in angle identification. We correct for this by requiring that changes in orientation between successive frames must be less than  $90^\circ$ . If this condition is not met, we shift the angle by  $180^\circ$ . To compute angular velocities, we first unwrap the angle time trace of each particle, making the time trace continuous instead of bounded by  $\pm 180^\circ$ . The orientations are then smoothed with a Gaussian filtering window subsequently differentiated, in a manner identical to the determination of velocities from the particle positions. See Appendix A.4 for further details on identifying particle orientations.

## Chapter 2

# Tunable Capillary-Induced Interaction Between Vertical Cylinders

This work was done in collaboration with Paulo Arratia, Jerry Gollub, and Arjun Yodh and is published in Langmuir [79].

### **Abstract**

Deformation of a fluid interface caused by the presence of objects at the interface can lead to large lateral forces between the objects. We explore these fluid-mediated attractive force between partially submerged vertical cylinders. Forces are experimentally measured by slowly separating cylinder pairs and cylinder triplets after capillary rise is initially established for cylinders in contact. For cylinder pairs, numerical computations and a theoretical model are found to be in good agreement with measurements. The model provides insight into the relative importance of the

contributions to the total force. For small separations, the lateral force is dominated by the fluid pressure acting over the wetted cylinder surfaces. At large separations, the surface tension acting along the contact line dominates the lateral force. A cross-over between the two regimes occurs at a separation of around half of a capillary length. The experimentally measured forces between cylinder triplets are also in good agreement with numerical computations, and we show that pairwise contributions account for nearly all of the attractive force between triplets. For cylinders with equilibrium capillary rise height greater than the height of the cylinder, we find that the attractive force depends on the height of the cylinders above the submersion level, which provides a means to create precisely-controlled tunable cohesive forces between objects deforming a fluid interface.

## 2.1 Introduction

Flow properties of granular materials can be greatly influenced by the presence of a small amount of fluid [40, 63]. This fluid-driven change in behavior can be quite dramatic and has important implications for industrial processing, mining, and construction, as well as geological phenomena such as landslides. Nevertheless, an understanding of how local capillary-bridge-induced force distributions influence bulk flow properties and give rise to global deformation is lacking.

Previous studies have explored how global mechanical stability and flow response vary with liquid content [11, 38, 43, 62, 66, 82, 95], but relating global response to microscopic details has proven challenging in three-dimensional systems. While X-ray tomography provides detailed information about the three-dimensional structure of the distribution of liquid inside the granular material [84], little progress has been made in three-dimensional systems towards controlling where liquid resides throughout the granular material, making systematic exploration of the relationship between grain-scale structure and large-scale flows challenging.

In two-dimensional rafts of floating particles, however, the fluid distribution is uniform, and

fluid-mediated interactions have been characterized for a variety of particles [5, 13, 56, 57, 59, 61, 65, 86, 97, 99, 100, 103]. Additionally, it has recently been shown that the fluid distribution in a particle monolayer in a water-lutidine mixture can be controlled and uniform. [34] In this paper, we characterize the capillarity-induced interactions between vertical cylinders standing upright on a substrate in a pool of liquid. Here the fluid is distributed uniformly, as in rafts and monolayers. Furthermore, the strength of the attractive force can be tuned by varying the depth of the pool of fluid. Both the uniformity and tunability of these forces in two dimensional systems may prove helpful for understanding the influence of local fluid-grain interactions on bulk-scale granular flow.

Wetting and capillary interactions have long been studied. [12, 23, 71] For vertical cylinders, one context is surface roughness and superhydrophobicity due to an array of micropillars [8, 41, 53, 74]. If the micropillars are long and flexible, elastocapillary effects can lead to coalescence, which has important implications in nature as well as engineering and materials science. [7, 16, 17, 47, 70, 93] In this paper, however, we will focus on a different context. Here the cylinders are rigid and are not anchored to the substrate on which they sit. As a result, the cylinders do not bend or deform but are free to move laterally in response to the fluid forces.

In this latter context, Princen [73] considered the wicking behavior of long thin fibers and developed a model to estimate the capillary rise height of liquid between two rigid vertical cylinders as a function of their separation. Kralchevsky, *et al.* [49–51] solved the linearized Laplace equation to derive an analytical form for the lateral forces between floating colloidal particles in the limit of small deformations of the fluid surface. Velev, *et al.* [98] and Dushkin, *et al.* [24] used a torsion balance to experimentally measure the lateral forces between two partially submerged sub-millimeter-diameter vertical cylinders at separations greater than half a capillary length. Forces at these separations were shown to be similar to the predictions of Kralchevsky, *et al.* [49–51], indicating that the small-deformation approximation is reasonable at large separations. Cooray, *et al.* [19] later achieved even better agreement with the experimental values by numerically solving the full non-linear Laplace equation. However, all previous works [19, 24, 49–51, 98] characterizing

these forces have been restricted to sub-millimeter-diameter cylinders of effectively infinite height as cylinder height always exceeds the equilibrium capillary rise height. Further, previous experimental works [24, 98] only characterize forces for separations larger than half a capillary length. The capillary attraction of vertical cylinders of finite height in the millimeter-diameter range has not been investigated experimentally or theoretically.

In this paper, we explore the fluid-mediated attractions between rigid vertical cylinders of finite height and diameter larger than the capillary length. A custom-built apparatus permits measurement of forces between several pairs of vertical cylinders as they are quasi-statically separated. We thus measure forces for separations as small as  $80 \mu\text{m}$ . The fluid-surface deformations are large at these small separations, and therefore the analytical form obtained from the linearized Laplace equation [49–51] is not valid. However, we find reasonable agreement with an extension of the Princen model to calculate the lateral forces between vertical cylinders. Numerical computations are also shown to be in good agreement with experimental measurements. We observe that for cylinders of finite height at small separations, the capillary rise of the fluid reaches the tops of the cylinders, thereby introducing a way to control the strength of cohesion between cylinders. Lastly, we observe a velocity-dependent hysteresis consistent with the observations of Velev, *et al.* [98].

## 2.2 Methods

### 2.2.1 Experimental Setup

We measure the capillarity-induced attractive forces between pairs and triplets of vertical cylinders partially submerged in a fluid, as shown in Figure 2.1a. The cylinders are acetal dowel pins with density  $\rho_{cyl} = 1410 \text{ kg/m}^3$ , height  $H = 19.05 \text{ mm}$ , and radius  $R = 3.175 \text{ mm}$ . The fluid is heavy viscosity mineral oil with density  $\rho = 870 \pm 10 \text{ kg/m}^3$ . The acetal-air-mineral oil contact angle,  $\theta_c$ , is estimated to be  $\theta_c = 20 \pm 5^\circ$  from numerous photographs of a single cylinder partially submerged in oil. Using the equation for capillary rise inside a glass cylindrical tube,  $h_{\text{rise}} =$

$2\gamma \cos \theta_{c,\text{tube}}/(\rho g r_{\text{tube}})$  along with a measured value of  $\theta_{c,\text{tube}} = 25 \pm 3^\circ$ , the surface tension is estimated to be  $\gamma = 27.4 \pm 0.7$  dyn/cm from photographic measurements of capillary rise heights inside capillary tubes of both  $5 \mu\text{L}$  and  $50 \mu\text{L}$  volumes. Most of the uncertainty in the surface tension measurement results from the uncertainty in the contact angle. The capillary length of the oil is  $l_c = (\rho g/\gamma)^{-1/2} = 1.8 \pm 0.2$  mm.

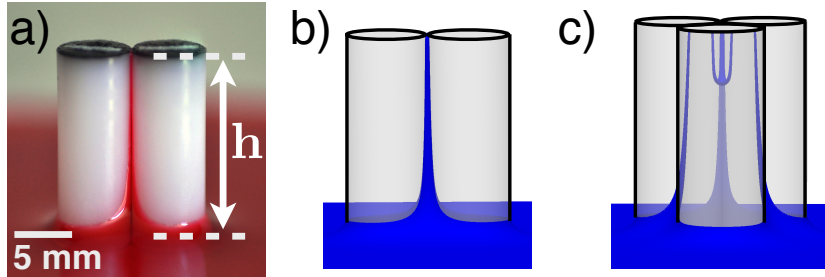


*Figure 2.1: a) A pair of  $R = 3.175$  mm upright cylinders standing in mineral oil (dyed red) viewed from the side. b) Final Surface Evolver output for a pair of cylinders with similar conditions to a), also viewed from the side. c) Final Surface Evolver state for a group of three cylinders. The capillary rise reaches the tops of the cylinders at small separations, causing the resulting cohesive force between to be set by  $h$ , the exposed height of the cylinders above the liquid reservoir.*

A custom-built apparatus, shown in Figure 2.2, is employed to measure oil-induced cohesive interactions between pairs and triplets of identical upright cylinders. The overall dimensions of the apparatus are 56 cm x 71 cm. Two threaded rods are mounted to the surrounding liquid-tight box with only the freedom to rotate. This rotation is driven by a stepper motor at a constant rate, permitting the translational motion of aluminum plate held by the threaded rods. Two force sensors mounted to the aluminum plate, one at each end, are sensitive to deflections perpendicular to the long axis of the plate. Equally spaced vertical cylinders are glued to a rod suspended from the aluminum plate. Neighboring cylinders attached to this rod have center-to-center separations

of  $4R$ , and all cylinder bases are about 1 mm above the box floor, hence there is no static and sliding friction between the cylinders and the surrounding box. The suspended rod hangs between the aluminum plate and the force sensors and is oriented with its long axis parallel to the plate long axis. With oil in the surrounding box, this suspended rod is always partially submerged.

Two rows of cylinders are glued to a stationary steel block, as shown in Figure 2.2, one for measuring the forces between pairs of cylinders and one for measuring the interactions between triplets of cylinders. The setup for pairwise measurements corresponds to the stationary block oriented such that the single white star is in the upper right corner, as shown in Figure 2.2. For each interacting pair, the line connecting the centers of the cylinders is parallel to the direction of driving, indicated by  $\vec{v}$  in Figure 2.2. An example of the geometry for a single cylinder pair viewed from the side is shown in Figure 2.1b. For triplets, the stationary block is oriented such that the two white stars are in the upper right corner. Each cylinder attached to the suspended rod interacts with two cylinders on the stationary block, forming equilateral triangles when the two rows are in contact. An example of the geometry for a single cylinder triplet viewed from the side is depicted in Figure 2.1c.

Cylinders are placed into contact after oil has been added to the surrounding box. Once capillary bridges have formed between the interacting sets of cylinders, the aluminum plate is then driven backward at 0.017 mm/s. The suspended rod resists this driving when capillary bridges are present and is therefore pushed against the force sensors, which are moving with the aluminum plate. The plate displacement,  $y$ , and the resulting force are measured as a function of time. This force is the sum of the individual capillary forces simultaneously acting on each of the cylinder pairs or triplets. Forces are measured with two Omega Engineering LCEB-5 mini-beam load cells, each with an error of 2.2 mN for a single measurement. Forces are recorded at 100 Hz and then temporally averaged with a window of 1.7 s, over which the cylinders move 0.029 mm, resulting in an uncertainty of 0.04 mN per sensor within an averaging window.

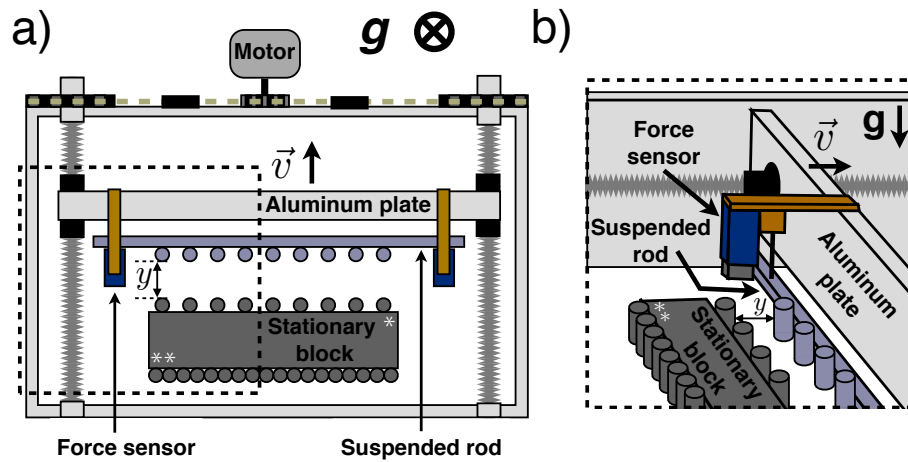


Figure 2.2: a) Top-down view of the setup for measuring cohesive forces between cylinder pairs (single white star in the upper right corner of the stationary block, as shown) and cylinder triplets (the stationary block is rotated 180° so that the two white stars are located in the upper right corner). This schematic not to scale: in the experiments, the entire apparatus measures 56 cm x 71 cm, each cylinder has radius  $R = 3.175$  mm and there are 15 cylinder pairs and 16 cylinder triplets. Another row of cylinders is glued to a rod suspended from a plate attached to a motor. The suspended cylinders are 1 mm above the base of the surrounding box. A known amount of mineral oil is added to the surrounding container for each set of experiments. Initially, the cylinders attached to the suspended rod are moved into contact with the cylinders attached to the stationary block, allowing capillary bridges to form between them. The suspended cylinders are then pulled away from the stationary cylinders. Lateral capillary forces resist this motion, causing the suspended rod to come into contact with and exert a force on the force sensors. b) Side view of the region enclosed by the dashed box in a).

### 2.2.2 Numerical Calculations

Numerical computations are performed using Surface Evolver [9, 14], a finite element modeling software package. Once the configuration geometry is defined along with relevant physical parameters and constraints, Surface Evolver uses the method of gradient descent to iteratively evolve the fluid surface toward the minimum total energy state. The fluid surface is represented by triangular elements, the size and density of which can be adjusted in between evolution steps.

For each computation, the configuration of upright cylinder pairs or triplets is defined by specifying the cylinder separations and exposed heights above the fluid. The undisturbed fluid resides in the  $z = 0$  plane, and the exposed cylinder height,  $h$ , is varied by adjusting the height of the cylinders above the  $z = 0$  plane. The size of the surrounding box containing fluid is set to be  $20R$  and is kept constant in all configurations. Constraints on the fluid-cylinder surface prevent the fluid from penetrating cylinder walls and constraints at the edges of the box fix the fluid vertices to  $z = 0$ . An additional constraint is imposed at the fluid-cylinder surface to model the interactions between cylinders of finite height: the fluid vertices in contact with the cylinders are not allowed to exceed the exposed cylinder height.

For a given exposed cylinder height,  $h$  (see Figure 2.1a), configurations are defined with surface separations ranging from  $d = 0.01$  mm to  $d = 10.0$  mm, and a separate energy-minimization is performed for each configuration. The treatment of each separation as an independent minimization is valid in the quasi-static limit of cylinder separation, which holds for slower separations speeds. Within a given configuration, the cylinder positions are fixed and only the fluid is allowed to evolve. The fluid is initially a flat surface in the  $z = 0$  plane. After a few mesh refinements, each of which divides each fluid element into four new elements, and a few evolution iterations, each of which moves the fluid surface to a lower-energy configuration, the fluid begins to rise up between the cylinders. Triangle elements with area less than  $5 \times 10^{-13}$  m<sup>2</sup> are regularly removed from the mesh to prevent instability of the gradient descent method. Once the fluid motion be-

comes small, indicating the capillary rise has nearly reached the equilibrium rise height, then the surface is further refined and evolved until the energy difference between successive iterations,  $\Delta E$ , is on the order of  $10^{-13}$  J and the relative energy change between successive iterations is  $\Delta E/E \sim 10^{-10}$ . Examples of the minimized surfaces are depicted in Figure 2.1b for pairs and Figure 2.1c for triplets.

### 2.2.3 Theoretical Model

We aim to develop a model for the lateral capillary forces between upright cylinders of finite height, such as those shown in Figure 2.3, that will provide insight into the origin and relative importance of various contributions to the total attractive force. To understand and characterize these lateral forces, we need to determine the region of the cylinder over which fluid forces are acting, and then integrate local lateral forces over this region to determine the total attractive force between two cylinders.

Princen [73] developed a model to estimate the capillary rise between two vertical cylinders of infinite height partially submerged in a fluid. This model assumes that the capillary rise height,  $z_2$ , is much greater than the cylinder radius,  $R$ . In this regime, changes in the vertical curvature of the fluid are small, so fluid between the cylinders is treated as a perfectly vertical column wherein the horizontal cross-section of the fluid at height  $z$  is equal to the cross-section at  $z_2$  for all  $z$ . It follows from this assumption that the geometry of the system can be completely described by a horizontal cross-section of the fluid, as shown in Figure 2.3b, and that the fluid radius of curvature in the vertical direction is infinite. This approach permits the hydrostatic pressure across the fluid interface to be described completely by the horizontal radius of curvature,  $R_2$ ,

$$\gamma/R_2(z, d) = \rho g z, \quad (2.2.1)$$

where  $\gamma$  is the surface tension,  $\rho$  is the fluid density,  $g$  is the acceleration due to gravity, and  $z$  is the height from which the cross-section is taken.

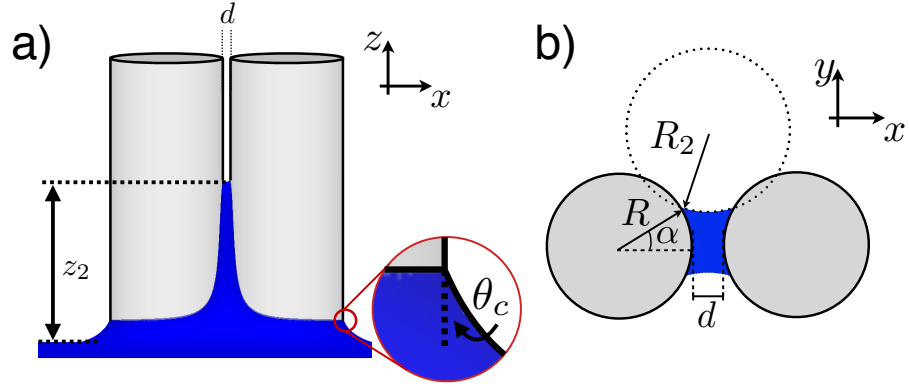


Figure 2.3: a) Side view of a capillary bridge between two upright cylinders, where  $z_2$  is the equilibrium rise height for a fluid with contact angle  $\theta_c$  between two cylinders, each of radius  $R$ , with surface separation  $d$ . b) View of the horizontal slice in the  $z = z_2$  plane.  $R_2$  is the radius of curvature of the fluid free surface in this horizontal plane, and  $\alpha$  is the angle between the line connecting the centers of the cylinders and the line from the center of the cylinder to the contact line.

We begin, as Princen did, by estimating the capillary rise height from vertical force balance. The total vertical force must vanish at the equilibrium capillary rise height, so we solve the following equation for the capillary rise height,  $z = z_2$ , at which the weight of the fluid between the cylinders is equal to the surface tension forces acting at the interfaces:

$$z_2 \rho g A(z_2, d) = 4\gamma R \alpha(z_2, d) \cos[\theta_c] - 4\gamma[\pi/2 - \theta_c - \alpha(z_2, d)] R_2(z_2, d), \quad (2.2.2)$$

where  $\theta_c$  is the contact angle,  $A(z_2, d)$  is the area of a horizontal cross-section of the fluid,  $d$  is the separation between cylinder surfaces,  $z_2$  is the height from which the horizontal cross-section is taken, and  $\alpha(z_2, d)$  is the horizontal angle between the line connecting the cylinder centers and a line from the center of a cylinder to the contact line on the surface of that cylinder, see Figure 2.3b. The left-hand side of Eq. (2.2.2) is an approximation of the weight of a fluid column between the cylinders in Figure 2.3a that reaches a height  $z_2$ . The first term on the right-hand

side describes the upward-directed surface tension force along the fluid-air-cylinder contact lines and the second term corresponds to the downward-directed surface tension force resulting from the free surfaces. Expressions for  $A(z, d)$  and  $R_2(z, d)$  can be determined from geometry [73].

We use Eq. (2.2.1) and the expression for  $R_2(z, d)$  to determine  $\alpha(z, d)$ , which, when substituted into Eq. (2.2.2) along with expressions for  $A(z, d)$  and  $R_2(z, d)$ , yields a transcendental equation that can be numerically solved for the capillary rise height,  $z_2$ :

$$\begin{aligned}
0 = & \left( \frac{\gamma}{\rho g z_2 R} \right)^2 \left\{ \frac{\pi}{2} - \theta_c + \alpha(z_2, d) + \sin[\theta_c + \alpha(z_2, d)] \cos[\theta_c + \alpha(z_2, d)] \right\} \\
& + 2 \frac{\gamma}{\rho g z_2 R} \left\{ \sin[\alpha(z_2, d)] \cos[\theta_c + \alpha(z_2, d)] - \alpha(z_2, d) \cos[\theta_c] \right\} \\
& + \sin[\alpha(z_2, d)] \cos[\alpha(z_2, d)] - \alpha(z_2, d). \tag{2.2.3}
\end{aligned}$$

Unlike Princen, our cylinders have finite height,  $h$ , above the liquid in which they are partially submerged. If the calculated  $z_2$  exceeds  $h$ , as it often tends to for small separations, we set  $z_2 = h$ .

Using this capillary rise height, we can estimate the lateral attractive force between the cylinders. Both pressure and surface tension contribute to the total capillary-induced attractive force on one cylinder, which is given by

$$\begin{aligned}
F_{\text{total}}(z_2, d) = & 2 \int_0^{z_2} \rho g z R \sin[\alpha(z, d)] dz \\
& + 2\gamma R \sin[\theta_c] \sin[\alpha(z_2, d)] + 2\gamma \int_0^{z_2} \sin[\alpha(z, d) + \theta_c] dz. \tag{2.2.4}
\end{aligned}$$

The first term is the pressure contribution, which acts over the cylinder-fluid contact area, the second term comes from the surface tension acting at the fluid-air-cylinder interface along the top of the capillary bridge, and the third term arises from the surface tension acting at the fluid-air-cylinder interface along the height of the cylinder. The model allows us to examine the relative importance of the independent force contributions, something we do not have access to from our other measurements or calculations.

Note we relax the  $z_2 \gg R$  assumption only after determining the rise height,  $z_2$ . We allow the horizontal cross-section to vary with  $z$  for the lateral force calculation, while at the same time still

assuming that the each horizontal cross-section can be treated independently and summed over to yield the total attractive force. Despite this technical inconsistency, we show in the results section that the total force from this model agrees well with experimentally-measured and numerically-computed forces.

It is also important to note that the model breaks down for  $\alpha(z, d) > \pi/2 - \theta_c$ . Given that  $\alpha(z, d)$  increases with  $d$ , there is a corresponding maximum  $d$  for which the model is valid. At  $\alpha = \pi/2 - \theta_c$ ,  $R_2 = \infty$  and  $z_2 = 0$ . Here, the capillary pressure contribution to the vertical force is zero, therefore, the total surface tension contribution to the vertical force must also equal zero. Equivalently, both sides of Eq. 2.2.2 must equal zero independently. In this case, the free interface in Figure 2.3b becomes a straight line, and the second term on the right-hand side of Eq. 2.2.2 must be re-written to have a finite value. The the maximum  $d$  for which the model is valid,  $d_{\max} = 2R[(\pi/2 - \theta_c) \cos \theta_c + \sin \theta_c - 1]$ , is then given by setting the modified right-hand side of Eq. 2.2.2 to zero. For the parameters in our system,  $d_{\max} = 3.3 \text{ mm} \approx 2l_c$ . Therefore, comparisons with previous long-range asymptotic solutions is not possible.

## 2.3 Results and Discussion

### 2.3.1 Interactions Between Cylinder Pairs

For a given exposed cylinder height, five independent experiments each measure the force as a function of separation. Temporal averages are performed on data from each experiment separately, the result of which can be seen in the inset of Figure 2.4. For an individual experiment, the error associated with one cylinder pair is 0.05 mN, and the standard deviation of the forces measured from five experiments is 0.1 mN. We note that these uncertainties are about the same as those resulting from the limitations of the force sensors discussed in the Experimental Setup part of the Methods section.

Force curves for 12 different exposed cylinder heights,  $h$ , can be seen in the main plot of

Figure 2.4. Note that the contribution from adjacent cylinder pairs is negligible as the forces in Figure 2.4 fall to zero by  $d = 2$  mm while the minimum surface-to-surface separation between adjacent pairs is  $2R = 6.4$  mm. Due to the nature of the setup, we cannot reliably measure forces for separations smaller than  $80 \mu\text{m}$ . While the cylinders are initially in contact, it takes a finite but small amount of time for the suspended rod to establish full contact with and subsequently push on the force sensors. Once this occurs, the forces quickly jump to a maximal value and then slowly decrease as separation increases. As a result, we exclude force data for separations smaller than  $d = 80 \mu\text{m}$ , which is the separation at which this maximal force occurs.

The capillary bridges reach the tops of the cylinders for small surface separations, causing the force to deviate from the infinite-height cylinder predictions at small separations. This effect causes the force to depend on the height of the exposed cylinder above the oil. Not surprisingly, the maximum attractive force is greater for larger exposed cylinder heights. Forces for all  $h$  collapse at large separations, which is expected. The dependence of the forces on  $h$  arises when the equilibrium capillary rise height exceeds the cylinder height. At large separations capillary rise height never reaches the cylinder tops, causing the dependence on  $h$  to vanish. In the intermediate-separation regime, forces for larger cylinder height  $h$  collapse at lower  $d$  than corresponding forces for smaller  $h$ . This effect is also expected, because the capillary bridge height will fall below  $h$  sooner for larger exposed cylinder heights.

We perform a global fit of the model to the measured forces up to  $d = 1.5$  mm for the eight largest  $h$  values and extract the surface tension and contact angle that best describe the data, as well as the  $h$  value that best fits each of the eight data sets. The global fit is achieved using the interior-point algorithm for constrained minimization of sum of the squares of the difference between the data and the model. The contact angle and the surface tension are treated as global parameters, and the exposed cylinder heights are treated as local parameters. The resulting best-fit contact angle is  $\theta_{\text{fit}} = 14.8^\circ \pm 4.0^\circ$  and the surface tension is  $\gamma_{\text{fit}} = 27.0 \pm 0.7$  dyn/cm, both of which are close to the experimentally measured values. The values for each of the exposed

cylinder heights,  $h_{\text{fit}}$ , are within the uncertainty of experimentally measured values and have 95% confidence intervals of  $\pm 0.1$  mm. Though the model is overly-simplistic, it nevertheless agrees remarkably well with the experimental data, both in terms of the fits and the values of the fitting parameters. Given the smaller bounds on the fit values for the exposed cylinder heights, we use the model fit parameters in all numerical computations.

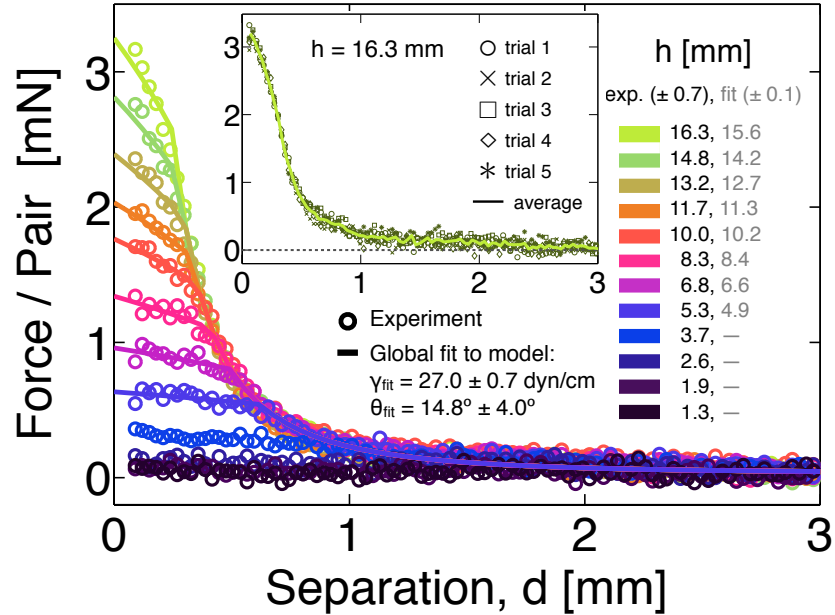


Figure 2.4: Experimentally measured attractive forces between cylinder pairs (circles) as a function of separation for many exposed cylinder heights,  $h$  as labeled. Each curve is the result of averaging five experimental trials together. Raw data and the resulting average curve for  $h = 16.3$  mm are shown in the inset. The uncertainty in the depth measurements is  $\pm 0.7$  mm, and forces for  $d < 80 \mu\text{m}$  are excluded because they cannot be measured reliably. Lines represent the result of a global fit of the model to the eight largest exposed cylinder heights.

Fluid-mediated interactions between a pair of upright cylinders are also explored numerically using Surface Evolver [9,14]. The minimized energy values as a function of separation are shown in Figure 2.5 for three values of exposed cylinder height. Each open circle is the result of an

energy-minimization calculation for a given surface separation,  $d$ , and exposed cylinder height,  $h$ . Smoothing splines are fit to each data set for a particular  $h$  and differentiated to obtain the attractive forces between the cylinders. There is a small though systematic underestimation of the Surface Evolver attractive forces when compared to the experimental values. This slight discrepancy is likely a result of the best-fit parameters from overly-simplistic model, which are used in Surface Evolver computations.

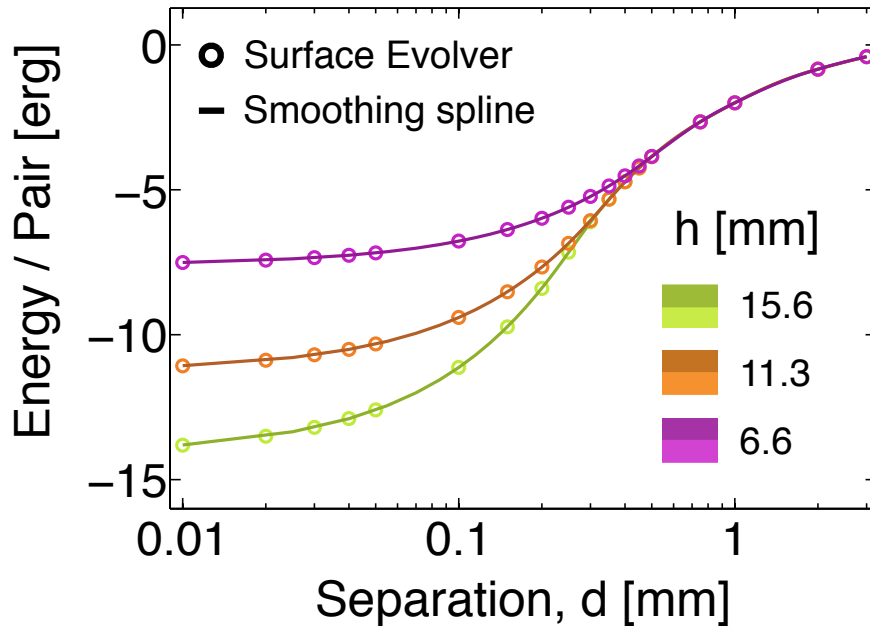


Figure 2.5: Surface energies as a function of cylinder separation determined using Surface Evolver, using best-fit parameters from the model. Each data point (circle) corresponds to one simulation. The simulation data for each exposed cylinder height is fit to a smoothing spline (solid lines), which is then differentiated to determine the force of attraction between cylinder pairs as a function of  $d$ , the separation of the cylinder surfaces.

The model discussed in the Theoretical Model part of the Methods section divides the total attractive force into two contributions: a force due to hydrostatic pressure inside the fluid and a force due to surface tension along the air-fluid-cylinder interfaces. The resulting attractive force

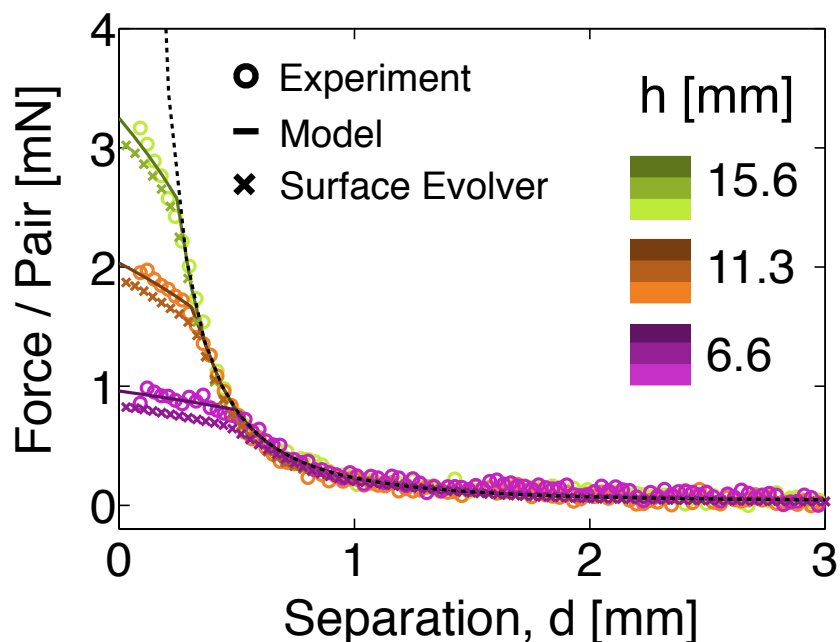


Figure 2.6: Attractive forces between cylinder pairs: experimental measurements (circles), Surface Evolver energy derivatives (lines), and model calculations (squares) for three different liquid levels. The dashed line indicates force predicted by the model discussed in the Theoretical Model part of the Methods section for infinitely tall cylinders. Deviations from this line occur at small separations,  $d$ , because the capillary rise has reached the tops of the cylinders.

predictions are compared for three exposed cylinder heights in Figure 2.6. The corresponding experimental measurements and numerical computations are shown as well, and all are in reasonable agreement. The dashed line on the plot shows the result of the model for infinitely tall cylinders. Deviations from this line at small separations,  $d$ , are caused by the finite cylinder height, specifically when the equilibrium capillary rise height exceeds the cylinder height. While the cylinder height does not explicitly enter into the model calculation, it is imposed by not allowing the capillary rise height to exceed the cylinder height. The resulting maximum fluid heights are consistent with those measured from the final states of Surface Evolver calculations, and the resulting force curves capture reasonably well the small-separation behavior observed in

experimental measurements as well as numerical calculations.

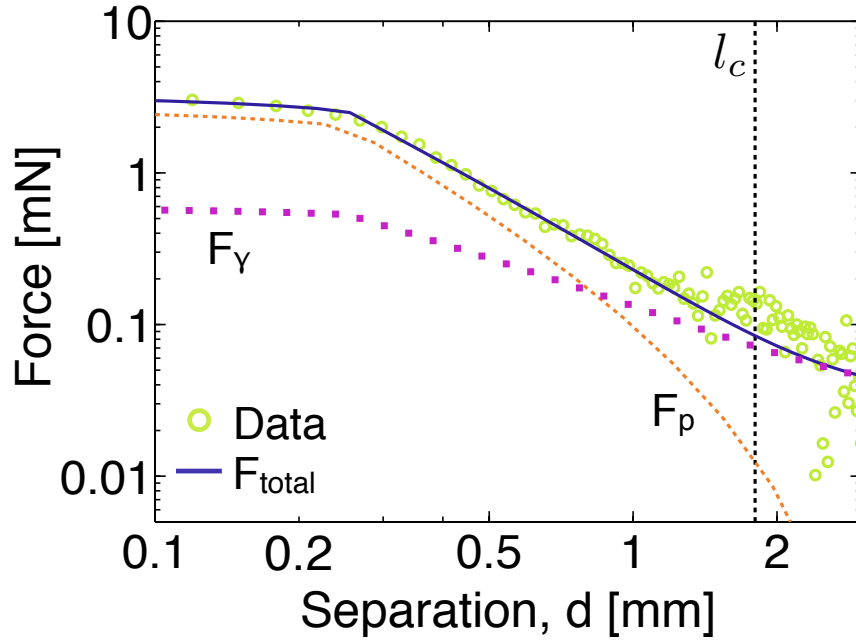


Figure 2.7: Experimental data for  $h = 16.3$  mm shown (circles) along with total predicted force from the model using best-fit parameters from the model (solid line). The total predicted force, given in Eq. (2.2.4), is the sum of three terms. The first term in Eq. (2.2.4) is the force contribution from the pressure inside the fluid (dashed line) and remaining two terms describe the surface tension force (dotted line). The force is dominated by pressure for small separations, while surface tension is more important for large separations. There is a cross-over in the dominant contribution to the total force around  $0.5l_c$ . The near-plateau at small separations,  $d$ , is due to the finite height of the cylinders. In this entire region, the capillary rise height reaches the tops of the cylinders, so the increase of force here is caused only by an increase in the thickness of the capillary bridge as the separation between the cylinders decreases.

The model provides insight into the relative importance of the force resulting from surface tension acting along the contact line as well as the force from the fluid pressure acting along the wetted surface. Figure 2.7 shows experimentally measured forces for one exposed cylinder height,

along with both the total force predicted by the model as well as the individual components that contribute to the total force. The pressure term dominates the force at small separations, there is a crossover around  $d = 0.5l_c$ , and then surface tension dominates for  $d \gtrsim l_c$ . One limitation of the model is that breaks down for  $d > 2l_c$ ; thus we are unable to predict how these forces behave at very large separations.

### 2.3.2 Interactions Between Cylinder Triplets

To test pairwise additivity, we also measure the force required to pull one cylinder away from two neighbors, with all three initially in mutual contact. The setup is similar to the one depicted in Figure 2.2, the only difference being that the stationary block is rotated  $180^\circ$  so that the two white stars are in the upper right corner. Forces are measured as a function of aluminum-plate displacement,  $y$ , using the same procedure as for pairs. For triplets, however, the surface separation,  $d$ , is not equivalent to  $y$ , though they are geometrically related through the equation  $d = -2R + \sqrt{4R^2 + 2\sqrt{3}Ry + y^2}$ . Figure 2.8a shows the final force curves, each of which is the average of five independent experiments, as a function of  $d$  for numerous exposed cylinder heights.

Surface Evolver is used to numerically determine the minimum energy of a fluid surface disturbed by the presence of three upright cylinders. Energy minimizations are performed for numerous configurations, such as the one shown in Figure 2.1c, each with fixed values of  $h$  and  $y$ . For each value of  $h$ , a smoothing spline is fit to corresponding energy data points and differentiated to obtain the attractive forces between cylinder triplets. Figure 2.8b shows reasonable agreement between differentiated Surface Evolver energies for three values of  $h$  and the corresponding experimental data.

We can determine the importance of non-pairwise terms to the overall force by comparing the pairwise and triplet force data. The forces measured for each cylinder triplet have a contribution from the capillary bridges between two cylinder pairs as well as the liquid that rises up in the center of the triangle formed by the three cylinders. An example of these capillary bridges can be

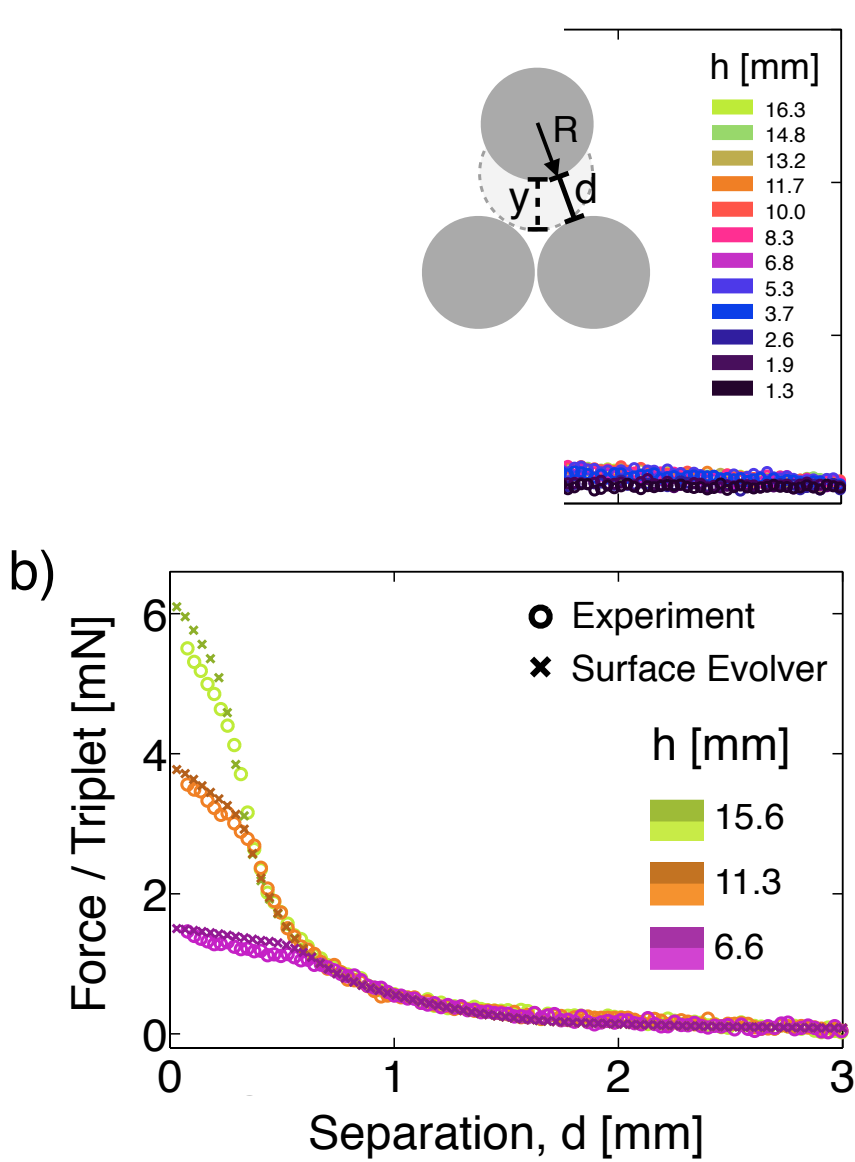


Figure 2.8: a) Force vs separation for a group of three cylinders for many exposed cylinder heights,  $h$ . b) Experimental force data and Surface Evolver energy derivatives (using parameters from model fit) show reasonable agreement for three different  $h$  values.

seen in the final state of a Surface Evolver energy minimization in Figure 2.1c as though viewed from the side, through translucent cylinders.

We compare triplet forces with the expected forces for two interacting pairs in Figure 2.9. To

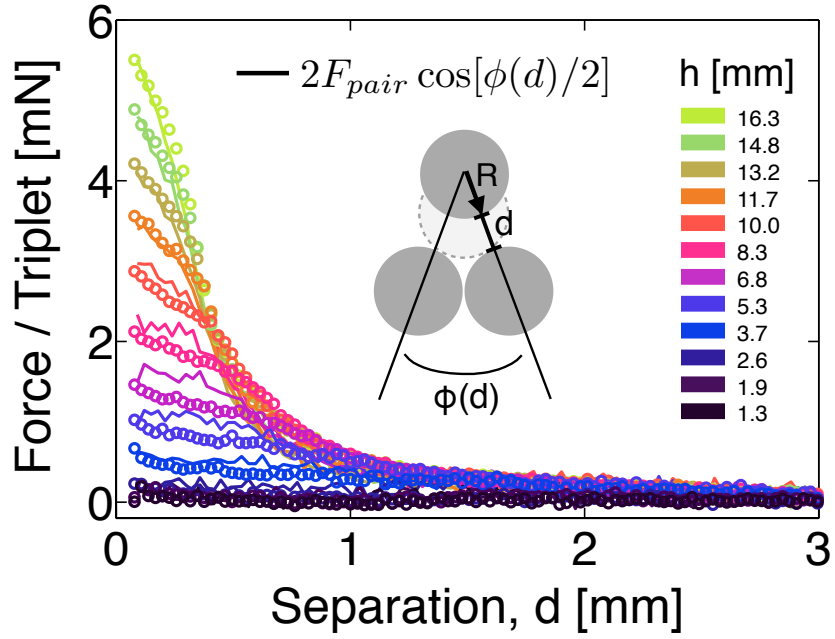


Figure 2.9: Force vs separation data are shown for triplets (circles) for numerous exposed cylinder heights. Forces between triplets will have contributions from the two pair-wise interactions acting in the directions  $\pm\phi(d)/2 = \pm \arctan(R/\sqrt{d^2 + 4Rd + 3R^2})$  relative to the direction of separation as well as a contribution from a capillary rise that occurs in the middle of the three cylinders. Contributions expected from the two pairwise interactions (solid lines) account for nearly all of the measured triplet interactions.

make this comparison, we must account for the fact that the force sensors are only measuring the component of the force in the direction of the motion. For the measurements between cylinder pairs, the direction of the maximum force and the direction of motion are the same. For the triplets, however, these directions differ by the angle  $\phi(d)/2 = \arctan(R/\sqrt{d^2 + 4Rd + 3R^2})$ , so we compare  $F_{\text{triplet}}$  to  $2F_{\text{pair}} \cos[\phi(d)/2]$  in Figure 2.9. Forces between triplets are reasonably well-described by the pairwise interactions, though the pairwise data falls off a bit faster in the 0.5 to 1 mm range. Discrepancies for low  $h$  may be due to the  $\pm 0.7$  mm uncertainty in the depth measurements. The overall agreement indicates that the contribution from lower capillary bridge

in the center of the three cylinders is comparatively small and can be neglected. The overall agreement indicates that the contribution from the lower capillary bridge in the center of the three cylinders is comparatively small and can be neglected. We expect that the capillary rise will be even smaller in the center of four or more cylinders and that, therefore, pairwise additivity is a reasonable approximation for arbitrary configurations of upright cylinders.

### 2.3.3 Hysteresis Between Cylinder Pairs

Contact angle dependence on the velocity of the contact line has long been observed in systems with relative motion between a solid and a fluid [1, 4, 25–27, 42, 45, 46, 48, 77, 80, 87, 92, 94, 104]. The advancing contact angle,  $\theta_A$ , measured when the fluid-solid contact area increases, is always measured to be greater than the receding contact angle,  $\theta_R$ , which is measured when the fluid-solid contact area decreases.  $\theta_A$  is observed to increase with increasing speed, and  $\theta_R$  has been observed to decrease with increasing speed in some experiments, though the  $\theta_R$  data tends to be more scattered.

The experimental setup used to measure attractive forces between cylinder pairs, shown in Figure 2.2, is also used to characterize the hysteresis in these attractive forces. Cylinders are initially placed into contact and, after capillary bridges form between all fifteen cylinder pairs, the aluminum plate is driven away from the stationary block to a distance of 6 mm. The aluminum plate remains static for one minute, after which the plate is driven back to its original position at the same speed. Averages of at least five experiments for each of four different speeds are shown in Figure 2.10. For small separations, forces measured while increasing separation are always larger than the corresponding forces measured for decreasing separation.

Given that the forces at large separations do not depend on the direction of driving, we expect that viscous drag and lubrication forces are negligible. We estimate the maximum drag force by  $F_{\text{drag}} \sim \pi R^2 \eta v_{\text{max}} / \delta z$ , where  $\eta \sim 65$  cP is the oil viscosity of the oil,  $R = 3.175$  mm is the cylinder radius,  $v_{\text{max}} = 0.136$  mm/s is the maximum speed of driving,  $\delta z \sim 1$  mm is the size

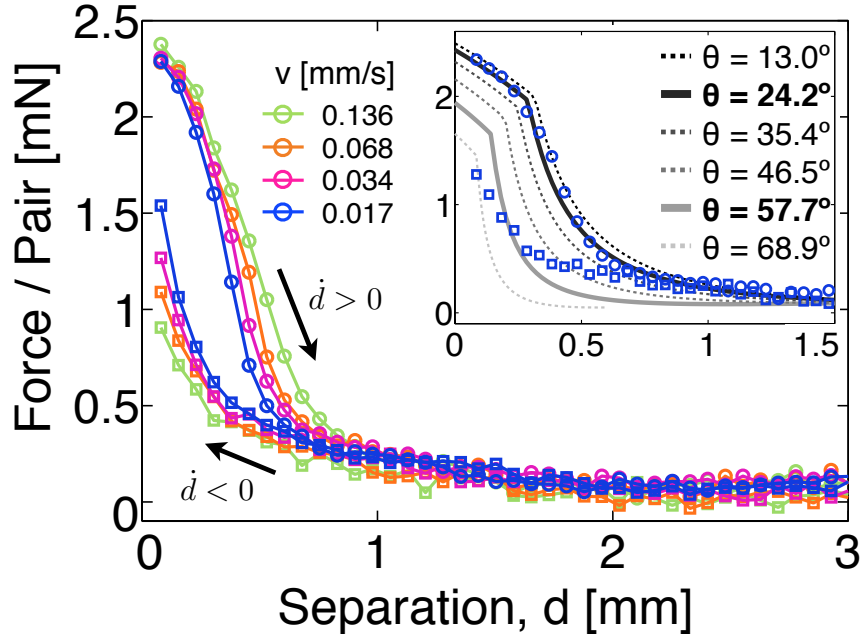


Figure 2.10: Measured force vs separation for cylinder pairs at different speeds for  $h = 14.1 \pm 0.7$  mm. A direction-of-motion-dependent hysteresis is observed, the strength of which is dependent upon the speed of the motion. The top curves (circles) are measured when the cylinder separation is increasing and the bottom curves (squares) are measured as the cylinders are pushed together. Lines represent the average of five to fifteen experiments, and the size of the points is indicative of the uncertainty. In the inset, experimental data for the slowest speed is plotted along with six evaluations of the model. The best-fit force curves are shown as the solid lines. Both contact angle and  $h$  are fit parameters for increasing separation data (circles). For the decreasing separation data,  $h$  is fixed and contact angle is the only fit parameter.

of the gap between the base of cylinders and the surrounding box floor. For our experimental conditions,  $F_{\text{drag}} \sim 10^{-7}$  N. We estimate the maximum order of magnitude of the lubrication forces between the cylinders by  $F_{\text{lub}} \sim \eta R H v_{\text{max}} / d_{\text{min}}$ , where  $H = 19.05$  mm is the maximum possible exposed cylinder height and  $d_{\text{min}} = 0.08$  mm is the smallest separation for which we are able to measure forces. From this, we obtain that the maximum possible force due to lubrication

is  $\sim 0.007$  mN. Both viscous drag and lubrication are significantly smaller than the observed hysteresis and therefore do not account for the observed behavior.

Our data is qualitatively consistent with previous work [98], in which the forces between approaching sub-millimeter cylinders at a separation of  $0.5l_c$  were found to be 10 – 15% smaller than the corresponding forces between separating cylinders. We also observe forces measured during separation to be higher than those measured while pushing cylinders together, though the magnitude of this difference is speed-dependent. This hysteresis in the measured forces is also qualitatively consistent with what is known about contact angle hysteresis. The contact line is receding down the cylinder surface when the separation between cylinders is increasing. This reduces the contact angle and leads to an increased force. Similarly, the contact line is advancing up the cylinders when cylinder separation is decreasing, causing an increase in the contact angle and leading to a decrease in the measured force.

The hysteresis measurements for the slowest speed are compared to the model in the inset of Figure 2.10. In these experiments, the exposed cylinder height is measured to be  $h = 14.1 \pm 0.7$  mm, and the static contact angle is estimated to be  $\theta = 20^\circ \pm 5^\circ$  from numerous photographs of a single cylinder in oil. The surface tension is measured to be  $\gamma = 28.6 \pm 0.7$  dyn/cm using the procedure described in the Experimental Setup part of the Methods section. Using these experimentally measured values, we simultaneously fit the model to increasing separation data at speed  $v = 0.017$  mm/s for two different liquid depths. Given the uncertainty in  $h$ , we allow both  $h$  and  $\theta$  to vary in the fitting, and find the best-fit contact angle to be  $\theta_{R,\text{fit}} = 24.2^\circ \pm 1.6^\circ$  and the best-fit exposed cylinder height for the data shown in the inset of Figure 2.10 to be  $h_{\text{fit}} = 12.7 \pm 0.3$  mm. We then fix the fit parameter  $h_{\text{fit}}$  to find the best-fit contact angle for the decreasing separation cylinder data,  $\theta_{A,\text{fit}} = 57.7^\circ \pm 3.4^\circ$ .

The best-fit model force curves are shown as the thick solid lines in the inset Figure 2.10, and curves from two intermediate angles, as well as one below  $\theta_{R,\text{fit}}$  and one above  $\theta_{A,\text{fit}}$ , are shown as dashed lines to give a sense of the model force dependence on the contact angle. The dark

solid line is the result for the increasing separation data, and the fit captures the behavior of the experimental data pretty well. The best fit of the model to the decreasing separation data, shown as the light solid line, does not describe the data well, which perhaps indicates that the decreasing cylinder separation forces cannot be described by a single contact angle.

The speed dependence of the separating cylinder data can be seen in Figure 2.10. As the speed increases, the force curves become broader and the forces fall off more slowly, especially for the two fastest speeds. Comparing this data with the model behavior in the inset, we see that a smaller contact angle is not enough to account for the changes observed in the force curves, indicating perhaps that the quasi-static assumption is not valid at faster speeds.

## 2.4 Conclusion

In this paper, we have characterized capillary-induced attractive forces between millimeter-sized cylinder pairs and triplets. Experimental measurements made with a custom-built apparatus are in reasonable agreement with numerical computations and a simple theoretical model. The model enables us to ascertain the surface tension and pressure contributions to the total force separately, and therefore compare their relative importance. We find that, at small separations, the pressure term dominates the total force, and at large separations, the surface tension force dominates.

The forces between triplets are reasonably well-described by the pairwise interactions. While some small discrepancies between the triplet and scaled-pair forces were found, we expect that these will monotonically decrease as the number of cylinders is increased. Therefore, pairwise additivity is a reasonable approximation for descriptions of the forces in a system with similar physical parameters and an arbitrary number of cylinders.

We also observed a velocity-dependent hysteresis of force measurements between cylinder pairs. For separations less than 1 mm, forces measured while separating cylinders are always larger than the corresponding forces measured for approaching cylinders. This finding is qualitatively

consistent with previous observations. The size of the hysteresis is observed to increase with increasing speed. We demonstrate that the simple model does not fit the data when the cylinder surfaces are approaching one another, which may suggest that a single contact angle is not enough to describe the data. We also show that the speed dependence of the separating cylinder data is not described by the model, perhaps indicating that the quasi-static assumption is no longer valid for the faster speeds.

Lastly, we observe that when the capillary rise height is greater than the cylinder height, the attractive force between cylinders depends the height of the cylinder above the liquid level. This effect can be employed to create a tunable cohesion. One benefit of such a force is that the liquid is distributed evenly throughout an array of cylinders or other particles, so that the force of attraction is known everywhere.

## Chapter 3

# Threshold-free characterization of local structure in amorphous materials

This work was performed in collaboration with Carl Goodrich and Andrea Liu.

### Abstract

Characterizing structural anisotropy is an essential step in understanding the mechanical response of amorphous materials. We introduce a new, threshold-free measure based on the observation that local disorder is reflected in the asymmetry of the Voronoi network, which is well-described by vectors originating from each particle center pointing to the centroid of the Voronoi cell in which the particle resides. These vectors tend to point in toward regions of high free volume and away regions of low free volume, reminiscent of sinks and sources in a vector field. We compute the local divergence of these vectors and find positive values correspond to *overpacked* regions and negative

values identify *underpacked* regions within the material. Distributions of this divergence are nearly Gaussian, allowing for structural characterization using only the moments of the distribution. We explore how the standard deviation and skewness vary with packing fraction in bidisperse systems and find a kink in these moments that coincides with the jamming transition.

### 3.1 Introduction

In this chapter, we introduce a new, threshold-free measure of structural anisotropy based upon the asymmetry of individual cells in the radical Voronoi tessellation. This measure is general as it is well defined in hard-sphere systems for which contact information is not available. In addition, this measure holds for systems with particle interactions governed by a potential, for which the concept of a particle contact is ill-defined. Distributions of this measure are nearly Gaussian, allowing for straightforward interpretation of the moments. We explore how the first two non-zero moments, the standard deviation and the skewness, vary with packing fraction for numerically generated packings.

### 3.2 Structural characterization

Our local structural characterization begins by constructing the network of nearest neighbors given by the radical Voronoi tessellation, sometimes referred to as the Laguerre or power tessellation, a space-filling generalization of the standard Voronoi tessellation. [3, 32, 33, 44] In this framework, space is divided into cells based on a given set of fixed points and associated weights, i.e, particle centers and radii, respectively. The power,  $\chi$ , at a point  $x$  due to the presence of particle  $p$  centered at point  $x_p$  with radius  $r$  is defined by

$$\chi(x, p(x_p, r)) = ||x - x_p||^2 - r^2. \tag{3.2.1}$$

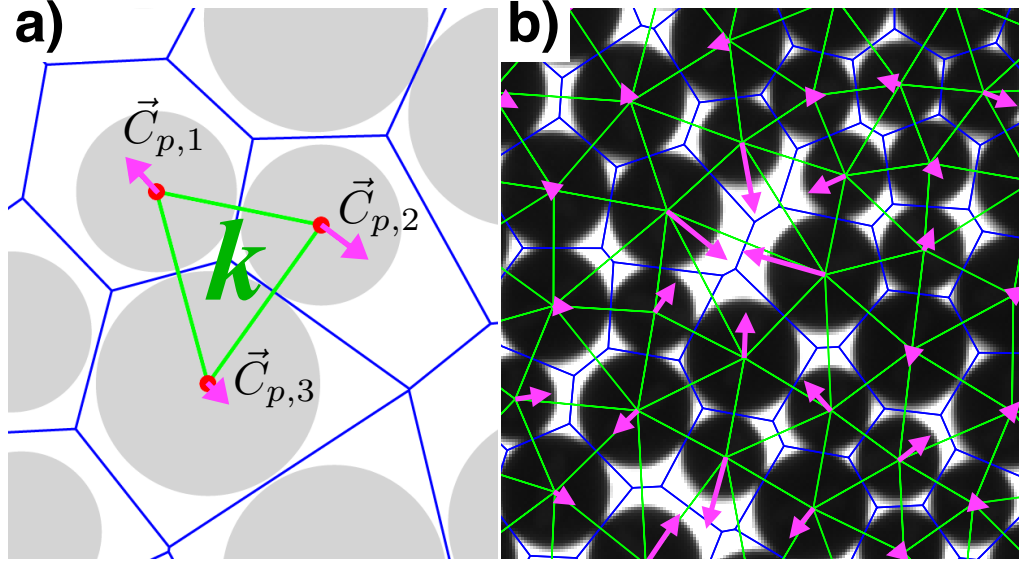


Figure 3.1: a) Three particles inside Voronoi cells (blue) and the corresponding Delaunay triangulation (green). Local anisotropy is characterized by the vectors (magenta) pointing from each particle center (red circle) to each Voronoi-cell centroid. b) Zoomed-in region of a disordered packing with super-imposed Radical Voronoi tessellation (blue) and resulting triangulation (green). Center-to-centroid vectors (magenta) are elongated by a factor of eight for ease of visualization.

Polygon boundaries are defined by the straight-line segments along which  $\chi$  from adjacent particles is equal. The benefit of this generalized method over standard Voronoi is that all particles are associated with exactly one cell, instead of being divided up amongst several cells. If all particle radii are equal, the standard Voronoi tessellation is recovered.

The software package `voropp` [81] is used to compute the radical Voronoi cell associated with each particle. Resulting Voronoi cells for the particles shown in Fig. 3.1 are overlaid in blue. Any two particles with a shared Voronoi cell edge are defined as neighbors, and from this, we generate a generalized Delaunay triangulation by connecting groups of three mutual neighbors into triangles, as shown in green in Fig. 3.1.

The position of a particle within its Voronoi cell is an indicator of local variation in the packing. This motivates us to define a local Voronoi anisotropy vector,  $\vec{C}_p$ , for each particle  $p$  that points

from the center of particle  $p$  to the centroid of the Voronoi cell that contains particle  $p$ , as shown by the magenta arrows in Fig. 3.1. In ordered packings, the particle center and the Voronoi cell centroid coincide, resulting in  $\vec{C}_p$  being identically zero for all  $p$ , which is consistent with the idea that  $\vec{C}_p$  is a measure of the structural anisotropy. While this vector has been mentioned before, as a Minkowski vector associated with a Voronoi cell [85] as well as in the context of liquid structure [30, 76] and granular fluids [88]. It has been shown in the fluid systems that particle motion is correlated with  $\vec{C}_p$ , which is consistent with what we might expect:  $\vec{C}_p$  points in the direction of excess free volume, indicating the direction in which the particle has the most space to move. However, local spatial variations of this vector have not been previously explored. Fig. 3.1b shows a typical example of  $\vec{C}_p$  vectors for several particles in a bidisperse packing with particle size ratio of 3: 4 and hard-sphere interactions. Vectors tend to point in toward (away from) locally less (more) well packed regions of the packing, reminiscent of sinks (sources) in a vector field. This analogy leads us to think about the local divergence of these vectors, which we will define for each triangle,  $k$ , as  $D_k = \vec{\nabla} \cdot \vec{C}_{p \in k}$ , where the three  $\vec{C}_p$  vectors originate at the particle centers,  $p$ , that make up the vertices of the triangle.

To determine the spatial variation of  $\vec{C}_p$ , and in particular, the divergence  $D_k$ , we use the framework of the constant strain triangle of finite element analysis [31, 58]. We consider each triangle in the generalized Delaunay triangulation independently and we now assume that the  $\vec{C}_p$  vectors associated with triangle  $k$  define a vector field  $\vec{C}_k = (C_1, C_2)$  that varies linearly over the triangle. It follows from this that  $C_1$  and  $C_2$  must be defined as

$$\begin{aligned} C_1(x_1, x_2) &= d_1 + d_{11}x_1 + d_{12}x_2 \\ C_2(x_1, x_2) &= d_2 + d_{21}x_1 + d_{22}x_2, \end{aligned} \tag{3.2.2}$$

and that the spatial derivatives of  $\vec{C}_k$  are constants. The six unknowns  $d_1, d_2, d_{11}, d_{12}, d_{21}$ , and  $d_{22}$  can be determined by evaluating Eq. (3.2.2) at the triangle vertices and inverting the resulting matrix equation. If the triangle coordinates are shifted so that the centroid of the triangle is

located at the origin, the vector  $(d_1, d_2) = (\langle C_1 \rangle, \langle C_2 \rangle)$ , where the averages are taken over the triangle vertices. The tensor  $d_{ij} = \partial C_i / \partial x_j$  is independent of the origin location and describes the spatial variation of the  $\vec{C}_k$  field over the triangle, with  $D_k = \text{Tr}(d_{ij})$ .

For each triangle,  $k$ , we define  $Q_k \equiv D_k A_k / \langle A_k \rangle$ , where  $A_k$  is the area of the triangle and  $\langle A_k \rangle$  is the average area over all triangles. As one might expect from the divergence theorem, all contributions from interior particles cancel upon performing the sum  $\sum_k Q_k$  over all triangles in a packing, leaving only contributions from the boundary particles. This results in  $\langle Q_k \rangle = 0$  in an infinite packing or a packing with periodic boundary conditions. The interpretation of  $Q_k$  is intuitive: triangles with  $Q_k < 0$  are less well packed than their surroundings, so we label these regions as *underpacked*, while triangles with  $Q_k > 0$  are locally more tightly packed than their surroundings, so we refer to these regions as *overpacked*.

Fig. 3.2a shows the nearly-Gaussian PDF of  $Q_k$  for the bidisperse system shown in Fig. 3.1b. PDFs of typical measures of free area are shown in Fig. 3.2b, and the inset shows that  $Q_k$  and standard free area fraction are related. There is a strong correlation between the fractional deviation of the local packing fraction  $\phi_{tri}$  from the global packing fraction,  $\phi$ , and  $Q_k$ , indicating that  $Q_k$  is akin to a relative free area fraction. This is consistent with our intuition and our classification of triangles based on the sign of  $Q_k$ . The benefit of  $Q_k$  over the standard free area fractions is that interpretation of  $Q_k$  is much more intuitive, and given that it is nearly Gaussian, moments of the distribution are much easier to interpret.

### 3.3 Dependence on packing fraction

To explore the behavior of  $Q_k$  as a function of  $\phi$ , we consider numerically generated systems composed of  $N = 2048$  soft repulsive disks with mass  $M$ . Two particles  $i$  and  $j$  interact with the pairwise potential

$$V_{ij} = \frac{\epsilon}{2} \left( 1 - \frac{r_{ij}}{R_i + R_j} \right)^2 \Theta \left( 1 - \frac{r_{ij}}{R_i + R_j} \right), \quad (3.3.1)$$

where  $r_{ij}$  is the distance between the particles' centers,  $R_i$  and  $R_j$  are the particles' radii,  $\Theta(x)$  is the Heaviside step function, and  $\epsilon$  sets the energy scale. To prevent crystallization, we use a 50 – 50 mixture of particles with a size ratio of 1.4. The disks are initially placed at random in a periodic simulation box with a packing fraction  $\phi$ . The units of length, mass, and energy are  $D_{\text{avg}}$ ,  $M$ , and  $\epsilon$  respectively, where  $D_{\text{avg}} \equiv N^{-1} \sum_m 2R_m$  is the average particle diameter.

Two ensembles were generated using different preparation protocols. First, thermalized configurations are generated at a very low temperature using molecular dynamics simulations at constant NVT, performed using LAMMPS [69]. Beginning at a temperature of  $T_{\text{start}} = 0.05$ , we slowly cool the system to  $T = 10^{-7}$  over  $5 \times 10^6$  time steps. The system then remains at  $T = 10^{-7}$  for an additional  $10^7$  time steps, after which we confirm from average particle mean-squared displacements that the particles are no longer behaving ballistically. Our second protocol corresponds to an infinitely fast quench to zero temperature. Beginning with the particles randomly placed in the simulation box, we minimize the total energy to a local minimum. Energy minimization is performed with the FIRE algorithm [10]. Each protocol was repeated 500 times at each packing fraction.

We first determine the  $Q_k$  for all triangles within a configuration, then we find the standard deviation and skewness of these  $Q_k$  values. Averages of these moments over 500 configurations per  $\phi$  are shown in Fig. 3.3. The main plots in Fig. 3.3 show the low  $\phi$  behavior of the standard deviation and the skewness for the packing generation protocols described above, as well as randomly placed non-overlapping monodisperse circles. To generate the non-overlapping monodisperse circle packings, a new circle can only be placed in a random position if there is no overlap when taking into account the radius the proposed new circle and the radii of all existing circles. If there is any overlap, the proposed circle is rejected.

The low  $\phi$  behavior of the standard deviation is shown in the main plot in Fig. 3.3a. All packings converge to a single value of  $0.5746 \pm 0.0002$ , which is equivalent to the value obtained for random point patterns. We intuitively expect this convergence as the packing generation

protocols are equivalent in the low  $\phi$  limit. As  $\phi$  increases, the decrease of the standard deviation away from this low  $\phi$  limit is dependent upon packing generation protocol, with quenched systems remaining at this upper bound for larger  $\phi$  than the other protocols. The standard deviation of the monodisperse non-overlapping circles and the thermalized data remain fairly close up to around  $\phi = 0.5$ , which is the largest packing fraction for which we are able to create the non-overlapping packings.

The inset in Fig. 3.3a shows the standard deviation behavior near  $\phi_c$  for the two thermalized and infinitely fast quenched systems, along with the  $\phi_c$  distributions, rescaled so that the peaks are just below the corresponding curve. The  $\phi_c$  distributions are obtained by finding the number of jammed configurations for a given  $\phi$ , and differentiating this with respect to  $\phi$ . The thermalized data has time to relax and explore unoccupied space near the particles, whereas the quenched data stops as soon as all overlaps are minimized, so we expect more heterogeneity in the quenched systems, and indeed the standard deviation for this protocol is always larger than thermalized data. Above  $\phi_c$ , both standard deviations are linear with similar slope. There is a kink for both protocols that coincides with the peak in the corresponding  $\phi_c$  distribution, indicating that there is a change in the distribution at the transition. In the thermalized data, there is a local minimum in the standard deviation around  $\phi \approx 0.83$  well below  $\phi_c \approx 0.846$  and below the  $\phi$  for which number of jammed configurations becomes nonzero.

The main plot in Fig. 3.3b shows the skewness of the  $Q_k$  distribution for thermalized and infinitely fast quenched packings, along with non-overlapping monodisperse spheres. As with the standard deviation, the skewness is protocol-independent for very low  $\phi$ , approaching the value of  $-2.086 \pm 0.002$  for random point patterns. This low  $\phi$  behavior is a global minimum for the thermalized and non-overlapping circles, however, the quenched data dips below this value until  $\phi \approx 0.6$ . This is not surprising as there is a much larger degree of spatial heterogeneity in the quenched systems. The inset in Fig. 3.3b shows the behavior near  $\phi_c$  for the thermalized and quenched data, along with rescaled  $\phi_c$  distributions. Again there is a kink for each protocol that

coincides with the peak in the corresponding  $\phi_c$  distribution.

### 3.4 Conclusion

For packings analyzed here, the low  $\phi$  behavior of the standard deviation as well as the skewness approach the value obtained for random point patterns and is independent of preparation protocol. For larger  $\phi$  values, we observe a kink in the standard deviation as well as the skewness that coincides with the peak of the  $\phi_c$  distribution. For thermalized systems, we observe a local minimum in the standard deviation below  $\phi_c$ , which is distinct from the jamming transition.

For disordered packings, we have shown  $Q_k$  is an intuitive, threshold-free measure of structure akin to a relative free area fraction. The distributions are nearly Gaussian, making interpretation of the moments straightforward. While our analysis has focused on two-dimensional packings, extending this measure to three dimensions should be straight-forward, with the addition of an extra term to each equation in Eq. 3.2.2 as well as the addition of one more equation. The focus of this paper has been on structure alone, though it would be interesting to compare this structural measure with local and extended dynamics to see what insight could be gained in the deformation of disordered systems.

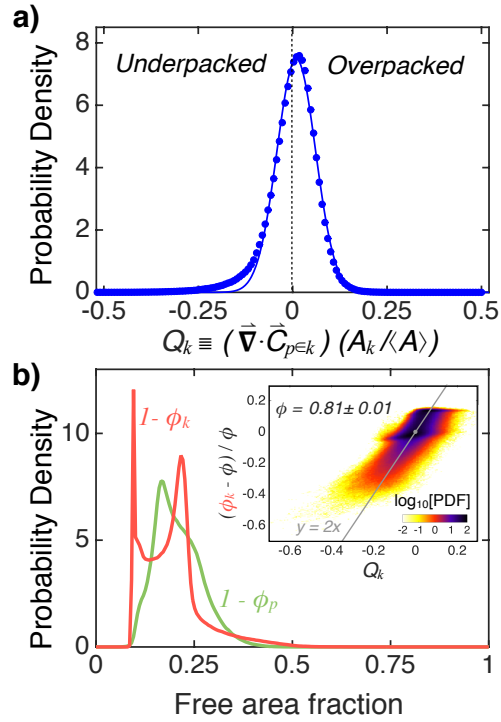


Figure 3.2: a) PDF of  $Q_k$  for a bidisperse packing of hard spheres with particle size ratio 3:4 (circles) and best-fit Gaussian (solid line).  $Q_k > 0$  regions are more tightly packed than their surroundings, hence we call these regions overpacked.  $Q_k < 0$  regions are more loosely packed than their surroundings, and are therefore labeled underpacked. b) PDFs of standard measures of free area fraction for the same packing. These distributions are more complicated and less intuitive than  $Q_k$ . Inset:  $Q_k$  correlates well with a fractional deviation from the global packing fraction, therefore is similar to a relative free area.

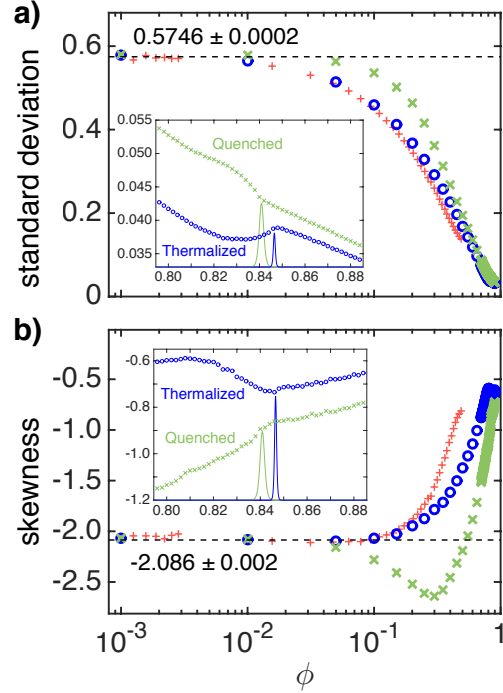


Figure 3.3: Average moments of  $Q_k$  distributions as a function of global packing fraction,  $\phi$ . In all plots, each data point represents the average value of the specified moment over several configurations, with the size of the point indicating the uncertainty in the average. The main plots show the low  $\phi$  behavior, which approaches the same constant value for all preparation protocols shown: infinitely-fast quench ( $\times$ ), thermal ( $\circ$ ), randomly placed non-overlapping monodisperse circles ( $+$ ), and random point patterns (dashed line). Insets show behavior near  $\phi_c$  for quenched ( $\times$ ) and thermalized ( $\circ$ ) configurations. Rescaled distributions of  $\phi_c$  are plotted as the solid lines, with color indicating preparation protocol from which they were determined. a) Standard deviation vs  $\phi$ . b) Skewness vs  $\phi$ . Both preparation protocols in a) and b) have a kink in the data that coincides with the peak in the respective  $\phi_c$  distribution.

# Chapter 4

## Local dynamics and structure

### 4.1 Introduction

The main focus of this chapter is the local dynamics within a two-dimensional granular pillar subjected to uniaxial compression, and how these dynamics relate to local structure for both cohesive and non-cohesive pillars. Uniaxial compression is chosen because it is similar to one of the common configurations for testing the mechanical response of metallic glasses [18, 36]. The two-dimensionality of the setup allows for direct visualization of all particles throughout the experiment, providing information that is not accessible in metallic glass compression studies. Details of the experimental setup are discussed in Chapter 1, and a schematic is shown in Fig. 1.2. Information about grain-grain interactions for the cohesive pillars can be found in Chapter 2.

For pillar compression data presented in this chapter, the strength of the forces in the cohesive pillars are given by the inset and top curve in Fig. 2.4. Non-cohesive pillars are created by completely submerging all particles. Pillars have 1523 grains, with 759 big grains and 764 small grains. This chapter is laid out as follows: Sec. 4.3 briefly discusses global forces measured at the compressing end of the apparatus, Sec. 4.4 explains how local dynamics are characterized, Sec. 4.5 discusses local measures of structure, and Sec. 4.6 focuses on how structure relates to dynamics.

Finally, the chapter concludes with preliminary results for dry indentation experiments.

## 4.2 Global packing fraction

From particle position and size data, we can determine the global packing fraction within the pillar throughout the compression. This is done by dividing the total area of all particles by the total area of each pillar, and is shown in Fig. 4.1 for all pillar compression experiments.

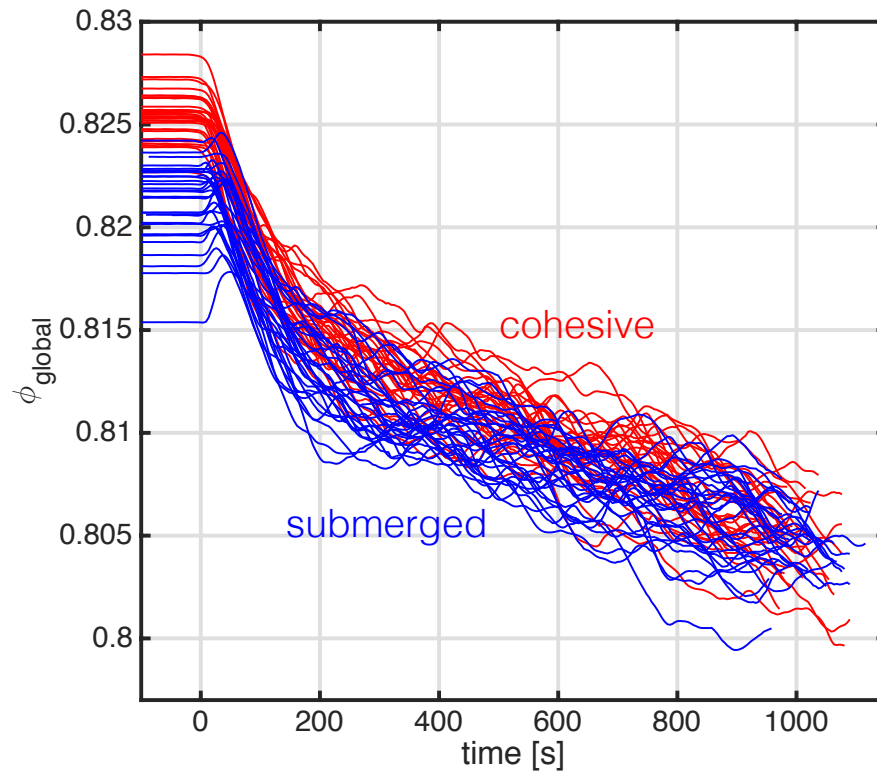


Figure 4.1: Global packing fractions for 30 cohesive pillars and 30 submerged pillars as a function of time. Compression starts at  $t = 0$ .

### 4.3 Global forces

As shown in Fig. 1.2, two force sensors are mounted to the aluminum bar that compresses the pillar, measuring the forces imposed onto the pillar. Force curves for a cohesive and a submerged pillar are shown in Fig. 4.2 as a function of global strain. Numbered points coincide with the corresponding images in Fig. 4.3. Forces measured by the sensors at the static end of the apparatus are not shown because these forces are zero for most of the experiment.

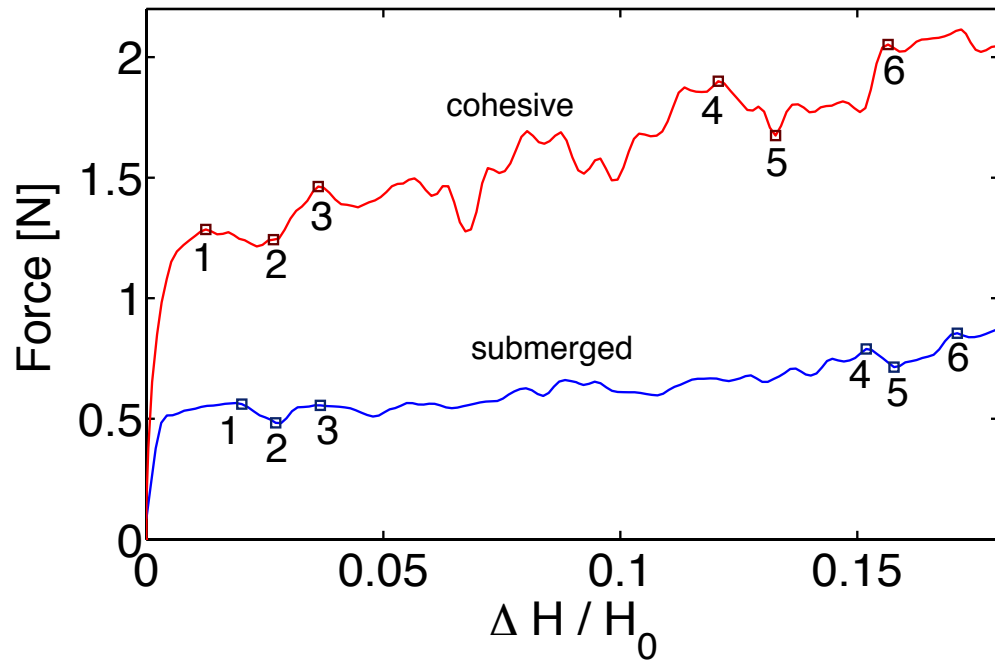


Figure 4.2: Global forces as measured from the moving end of the apparatus. Cohesive forces tend to be higher than the submerged forces. Numbered points correspond to times at which snapshots are shown in Fig. 4.3.

## 4.4 Dynamics

### 4.4.1 Particle velocities

For a single experiment, particle positions are determined in each image and subsequently linked together using custom-written codes, see Chapter 1 for details. The position as a function of time for each particle is then smoothed by convolving with a Gaussian of width  $\sigma = 4.375$  s. A Gaussian is chosen because the Fourier transform of a Gaussian is a Gaussian, resulting in a smoothly and continuously varying filter in both real space as well as Fourier space. Therefore, there are no artifacts introduced into the data from the Fourier transform. Particle velocities are determined by differentiating smoothed positions. For both positions and velocities, only one data point per  $\sigma$  is retained. Snapshots of particle velocities are shown in Fig. 4.3. The top row shows images from a cohesive experiment at six points in time, and the bottom row shows snapshots from a submerged experiment. Numbers here coincide with the numbered squares in Fig. 4.2. Colors indicate the speed of each particle relative to the speed of compression. To highlight the spatial anisotropy of the deformation, we determine the local spatial variation of the velocity vectors at each point in time.

### 4.4.2 Spatial velocity variations

To determine the local spatial variation of the velocity vectors,  $\vec{v}$ , we use the framework of the constant strain triangle of finite element analysis [31, 58]. We consider each triangle in the generalized Delaunay triangulation independently and we now assume that the  $\vec{v}$  vectors associated with triangle  $k$  define a vector field  $\vec{v}_k = (V_x, V_y)$  that varies linearly over the triangle. It follows from this that  $V_x$  and  $V_y$  must be defined as

$$\begin{aligned} V_x(x, y) &= e_x + e_{xx}x + e_{xy}y \\ V_y(x, y) &= e_y + e_{yx}x + e_{yy}y, \end{aligned} \tag{4.4.1}$$

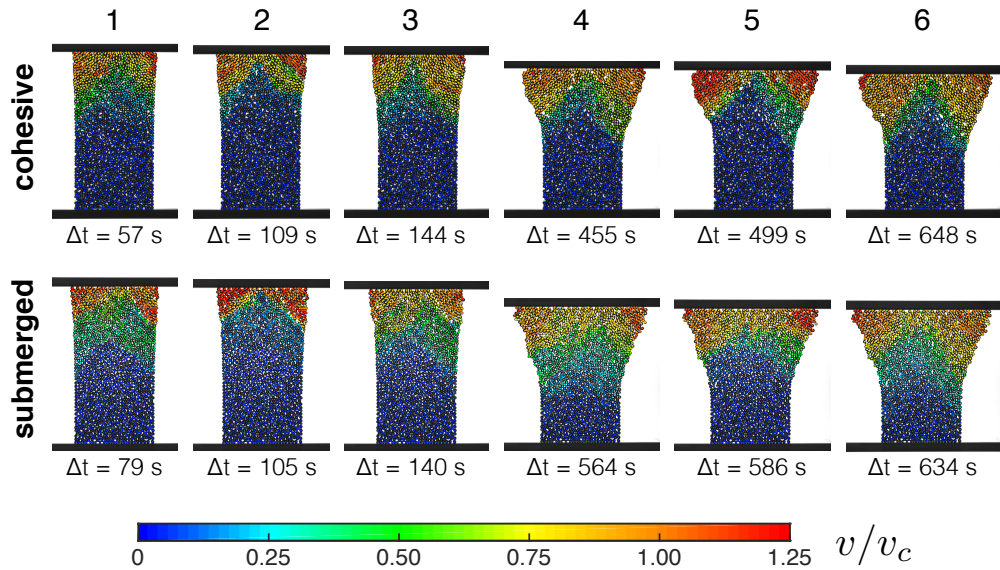


Figure 4.3: Snapshots of particle velocities for cohesive (top row) and submerged (bottom row). Colors indicate speed relative to the particle speed,  $v$ , of the compressing bar,  $v_c$ .  $\Delta t$  indicates time in each experiment relative to the time at which contact between the compressing bar and the pillar is established. In both cohesive and non-cohesive (submerged) experiments, the deformation is spatially anisotropic. Sharp spatial gradients in the velocities occur (as in 2 and 5), though the precise locations fluctuate in time.

and that the spatial derivatives of  $\vec{V}_k$  are constants. The six unknowns  $e_x, e_y, e_{xx}, e_{xy}, e_{yx}$ , and  $e_{yy}$  can be determined by evaluating Eq. (4.4.1) at the triangle vertices and inverting the resulting matrix equation. If the triangle coordinates are shifted so that the centroid of the triangle is located at the origin, the vector  $(e_x, e_y) = (\langle V_x \rangle, \langle V_y \rangle)$ , where the averages are taken over the triangle vertices. The tensor  $e_{ij} = \partial V_i / \partial x_j$ , called the velocity gradient tensor, is independent of the origin location and describes the spatial variation of the  $\vec{V}_k$  field over the triangle.

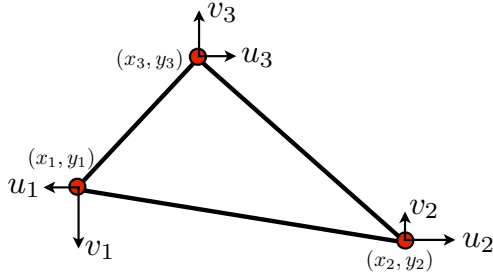


Figure 4.4: A single triangle with vertices given by particle centers.  $u$  and  $v$  represent  $x$  and  $y$  displacements of each vertex. Strains are determined by assuming these displacements represent a linearly-varying velocity field over the triangle.

If the spatial variations are small, then local strain rate tensor,  $\dot{\epsilon}_{ij}$ , can be approximated as the symmetric part of  $e_{ij}$ , given by  $\dot{\epsilon}_{ij} = (e_{ij} + e_{ji})/2$ , and the anti-symmetric part of  $e_{ij}$  approximates the local rotation rate,  $\omega = (e_{ij} - e_{ji})/2$ .

We focus on the invariants of the strain tensor, which do not depend on triangle orientation relative to the coordinate axes. The first invariant is the dilation rate, given by  $\text{Tr}(e_{ij})$ , which describes volumetric changes of the triangle. Examples of dilation rate are shown in Fig. 4.5. The second invariant, the deviatoric strain rate, given by  $\dot{J}_2 = \frac{1}{2}\sqrt{(\dot{\epsilon}_{11} - \dot{\epsilon}_{22})^2 + 4\dot{\epsilon}_{12}^2}$ , describes shape changes of the triangle. Deviatoric strain rates are shown in Fig. 4.6. Unlike dilation rates, the deviatoric strain rates highlight narrow bands of high shear. It is clear from the overall shape of the pillar throughout the deformation as well as the temporal variation in the band location that these shear bands are transient. Transient shear bands have been observed by others as well [52, 54], and in some cases have been noted to precede the formation of permanent shear bands [54].

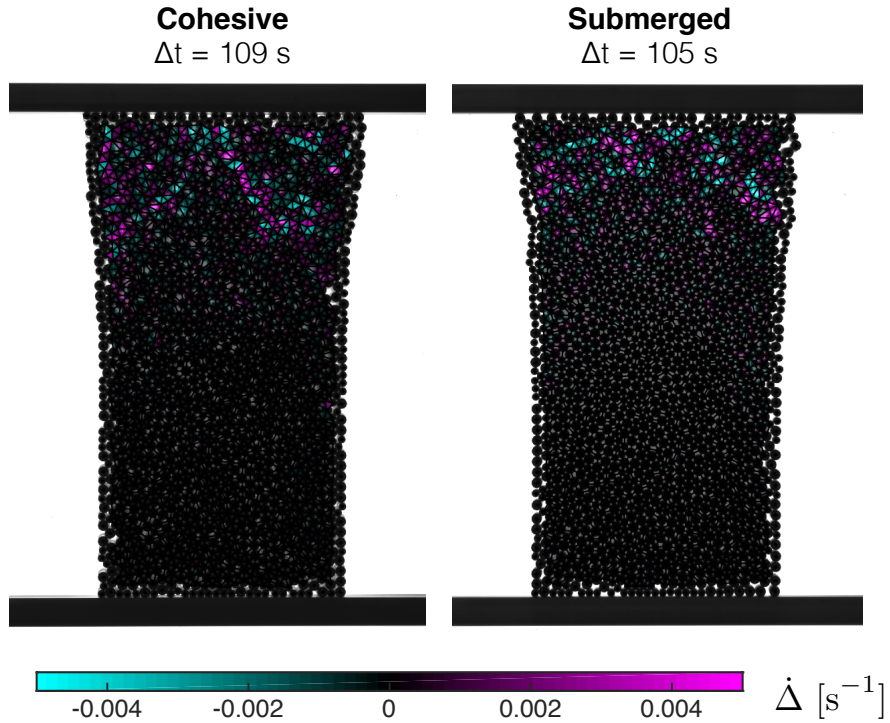


Figure 4.5: Snapshot of dilation rates for cohesive (left) and submerged (right), calculated per triangle.  $\Delta t$  indicates time in each experiment relative to the time at which contact between the compressing bar and the pillar is established.

## 4.5 Structure

Local free volume is has been proposed as an important contributor to material failure [89], with the idea that higher free volume areas tend to be more susceptible to local deformation, causing these places to be the first to yield, resulting in the local creation of more free volume. This feedback loop continues until the material can no longer support the external load, at which point the material yields and a shear band occurs. Local free volume is typically characterized from a nearest neighbor network or a contact network.

The nearest neighbor network is often given by a generalization of the standard Voronoi tessellation. One common generalization, the radical Voronoi or Laguerre tessellation, is shown in

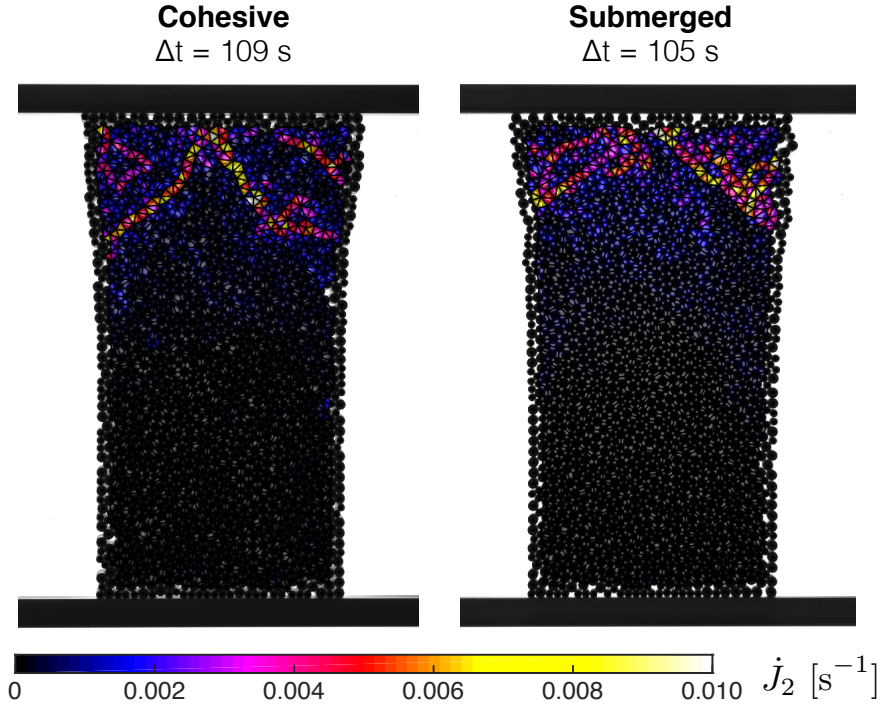
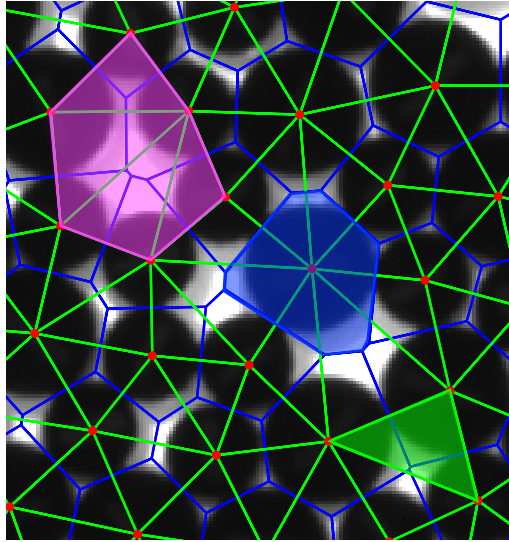


Figure 4.6: Snapshot of deviatoric strain rates for cohesive (left) and submerged (right), calculated per triangle.  $\Delta t$  indicates time in each experiment relative to the time at which contact between the compressing bar and the pillar is established. The sharp spatial gradients in the velocities are well captured by the deviatoric strain rates.

blue in Fig. 4.7. In this generalization, each Voronoi cell contains exactly one particle, and cells are polygons with edges that are straight line segments. The precise method for determining the location of these edges is discussed in Chapter 3. Free volume is then defined as the ratio of the particle area to the cell area. A shaded cell in an area of higher free volume is shown in Fig. 4.7. The actual free volume of the region is divided up amongst several Voronoi cells, which is not ideal as we want to identify these regions of high free volume. From this generalized Voronoi tessellation, a generalized Delaunay triangulation can be generated by connecting groups of three mutual neighbors. This network is shown in green in Fig. 4.7. This network, like the

Voronoi-based network, also divides the local pockets of free volume into multiple triangles, again underestimating the the total free volume in a local area.



*Figure 4.7: Snapshot of the experimental system with the radical Voronoi tessellation (blue) and the resulting generalized Delaunay triangulation (green). These networks provide a natural way to define a local free volume within the material, however, the free volume within a region tends to be distributed amongst several cells/triangles. Another more direct approach is to analyze closed loops in a particle graph or contact network (shaded magenta region), however, this requires precise information about particle contacts.*

Closed loops in a particle graph or contact network, for example the magenta polygon in Fig. 4.7, are the most direct way to characterize free volume. However, as Fig. 4.8 shows, the contact network is extremely sensitive to small uncertainties in precise particle locations. Potential contacts are color coded by particle-particle surface separation in mm in Fig. 4.8, and it is clear from this picture that this network changes drastically for small changes in particle separations. In these experiments, precise contact information is not known. While we could attempt to infer contacts based on particle separations, Fig. 4.8 indicates that this is not a robust way to characterize the local structure within the system.

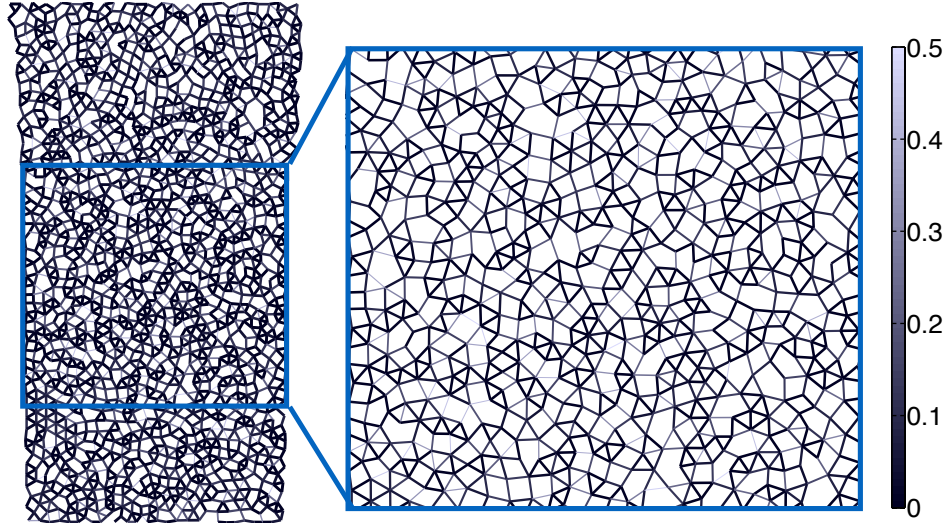


Figure 4.8: Contact network for a single snapshot of the experiment. Lines are drawn between Voronoi neighbors (i.e. any two particles that share an edge in the Voronoi tessellation), and are color-coded by particle-particle surface separation, up to 0.5 mm. Given the uncertainty in particle positions resulting from tracking error, we do not know precise contact information. As a result, we must choose a cutoff if we wish to proceed, and this figure indicates that our results will be quite sensitive to this cutoff.

A new measure of structure was introduced in Chapter 3,  $D_k = \vec{\nabla} \cdot \vec{C}$ , where  $\vec{C}$  is defined per particle as the vector that points from each particle center to the centroid of the Voronoi cell containing the particle. An example of this field is shown in Fig. 3.1, and we note that these vectors point inward toward areas of high free volume and away from areas of low free volume. This inspires us to determine the local divergence of these vectors, which we calculate on a per triangle basis, as explained in Chapter 3. Snapshots of  $D_k$  are overlaid on top of experimental

images for both cohesive and submerged experiments in Fig. 4.9. Notice that less well packed regions have  $D_k < 0$  while tightly packed regions have  $D_k > 0$ , and that there is more spatial heterogeneity in the cohesive case.

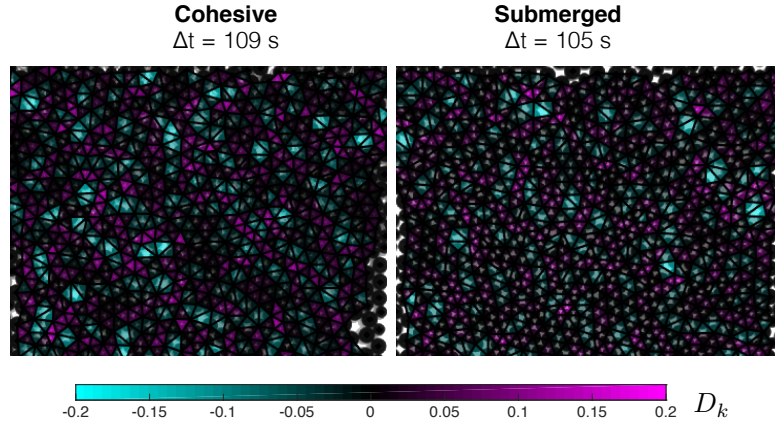


Figure 4.9: Snapshots of  $D_k$ , shown for both cohesive and submerged. A zoomed in region is shown so that details are more visible. The top of the box in each case is just below the compressing bar, and the box width is the entire pillar width. Regions with  $D_k < 0$  (cyan) coincide with regions of locally higher free volume, and regions with  $D_k > 0$  (magenta) coincide with regions of locally lower free volume.

The relation between  $D_k$  and the free volume is quantified in Fig. 4.10. There is a strong correlation between  $D_k$  and a relative free volume, defined per triangle as the difference of the local packing fraction of a central triangle and the average of all triangles that share at least one vertex with the central triangle. Therefore,  $D_k$  provides information about how well packed a region is relative to the surroundings: triangles with negative values are relatively less well-packed while triangles with positive values are relatively more well packed.

The PDFs of  $D_k = \vec{\nabla} \cdot \vec{C}$  for both cohesive and non-cohesive experiments are shown in Fig. 4.11. The initial state PDFs are reasonably well-described by the Gaussians defined by the distribution means and standard deviations. As deformation proceeds, the packing becomes more spatially heterogeneous and the distributions broaden. The cohesive distribution is broader, indicating that

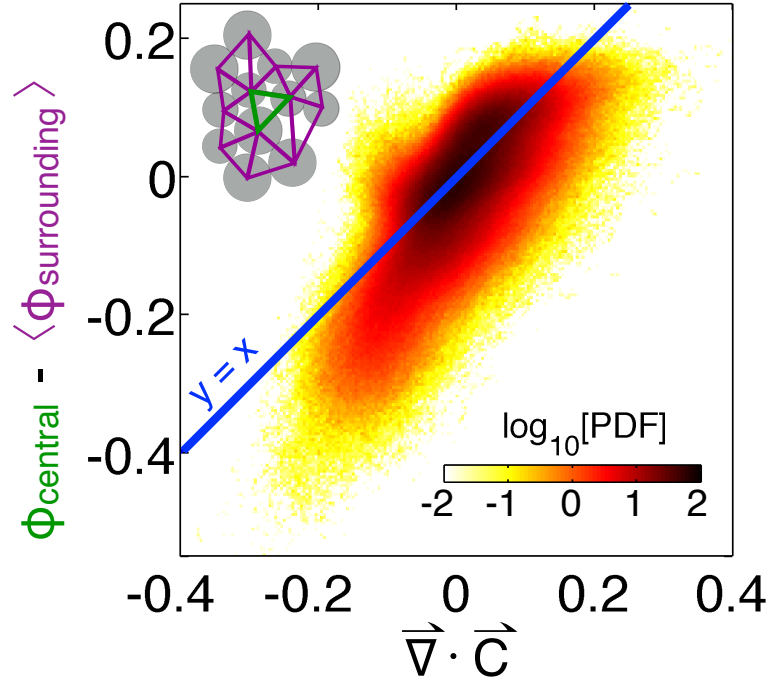


Figure 4.10: Logarithm of two-dimensional PDF of relative free area vs  $D_k = \vec{\nabla} \cdot \vec{C}$ . Relative free area, defined per triangle, is given by the difference of area fraction of the central triangle and the average of the surrounding triangles.

there is more heterogeneity in the presence of cohesion, which is consistent with the observation in Fig. 4.9.

## 4.6 Comparison between structure and dynamics

As pointed out in the previous section, the sign and magnitude  $D_k$  describes how well packed the local structure is relative to the local surroundings. We make equal-time comparisons of  $D_k$  values with strain rate values on a per triangle basis, and we only include triangles containing at least one particle that has moved at least a particle radius. This restriction is used because there is a static region at the base of the pillar that never deforms, not because it is stronger than the rest of the pillar, but simply because the disturbance never reaches that region. We have confirmation

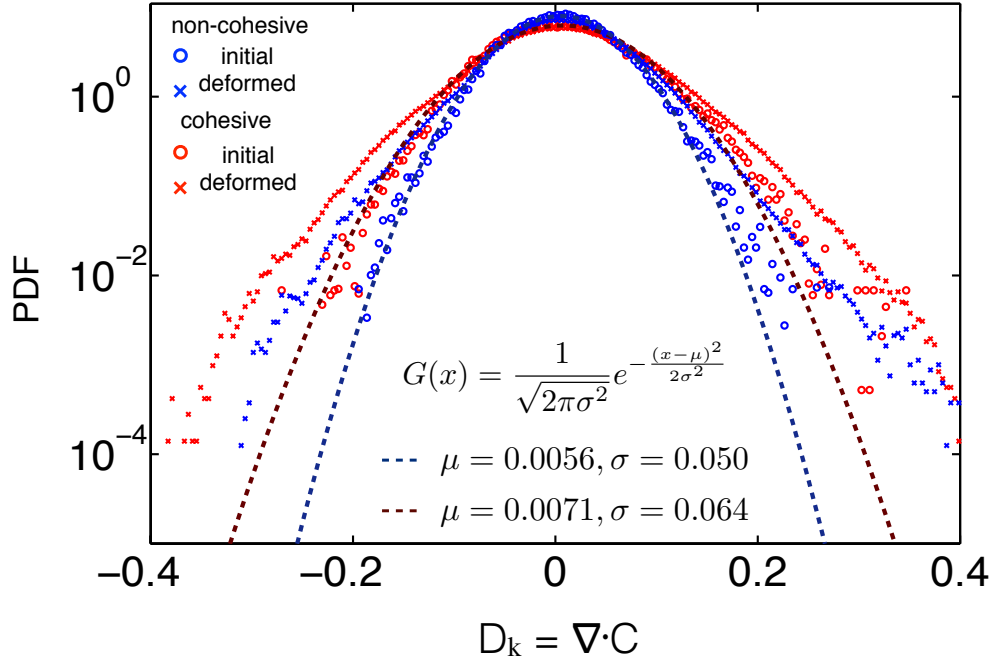


Figure 4.11: PDFs of  $D_k$  for 30 cohesive (red) and 30 submerged (blue) experiments. The initial states ( $\circ$ ) are defined as the prepared initial condition before compression starts. The deformed states ( $\times$ ) only include information from triangles in which at least one particle has moved one radius. The static triangles are not included because the disturbance never reaches them. The dashed lines represent Gaussians described the the mean,  $\mu$ , and the standard deviation,  $\sigma$ , of each initial data set. As deformation proceeds, the tails of the distributions broaden.

of this from the lack of measurable forces at the static end of the pillar.

We expect that regions with locally higher free volume are easier to deform than the surrounding area, and similarly that regions with lower free volume are harder to deform than their surroundings. As this is a relative statement about the strain rate, we define a relative strain rate, given by the difference of the deviatoric strain rate of a central triangle and the average of the surrounding triangles. As with the relative free area, the surrounding area is defined to be all triangles that share at least one vertex with the central triangle.

A two-dimensional PDF of the relative strain rate for each triangle vs the  $D_k$  value is shown

in Fig. 4.12. The color scale represents the logarithm of probability density at each point. The distribution is rather spread out, and it is not clear from this if there is any correlation between the structure and the dynamics. To investigate further, we bin the  $D_k$  values and average the relative strain rates within each bin. The result is shown in Fig. 4.13.  $D_k$  bins are logarithmically spaced, and each bin contains at least 100 data points. Error bars for the relative strain rates represent standard error of the mean within each bin, and  $D_k$  error bars show the width of each bin. As we expect, the relative strain rate is positive for  $D_k < 0$ , indicating that areas with higher free volume are, on average, experiencing higher strain rates than the local surroundings. Similarly, regions with  $D_k > 0$  have a negative relative strain rate, indicating that they are, on average, experiencing lower strain rates than the surrounding area. In addition, we see that, in the presence of cohesion, the resistance of the  $D_k > 0$  triangles to high strain rates levels off later than the non-cohesive data, which is consistent with the expectation that the strength of tightly packed regions is enhanced by the presence of cohesion.

## 4.7 Indentation

To probe the mechanical response of our amorphous granular packing to a more localized disturbance, we perform indentation experiments in which a wedge is driven into the packing, see Sec. 1.2.2 and Fig. 1.4 for details. Snapshots of particle velocities resulting from 45° and 90° indenters into packings containing no liquid are shown in Fig. 4.14. As with compression experiments, there are strong, temporally-varying spatial gradients in the velocities. Corrugations in the top surface of packing develop as a result of these sharp gradients, and they are similar to those observed in other systems. [96, 105]

We have explored how dynamics and structure are related for two different wedge angles, and the results are shown in Fig. 4.15. We see a statistical correlation here that is similar to the correlation shown for compression experiments in Fig. 4.13. Interestingly, we see a dependence on

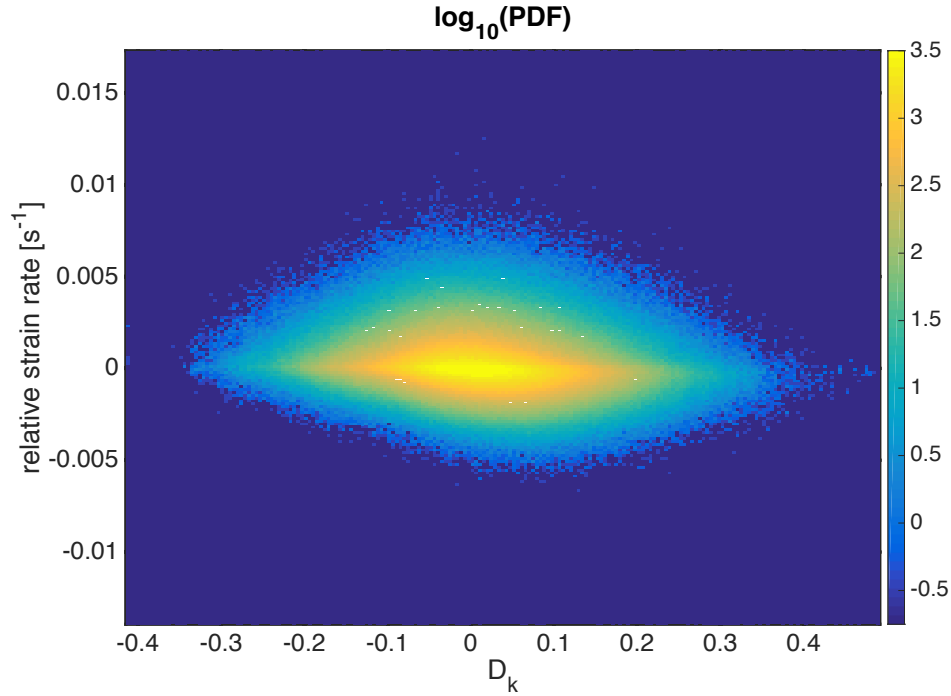


Figure 4.12: Logarithm of the two-dimensional PDF of relative strain rate vs  $D_k$  for 30 cohesive experiments.

wedge angle for the dry experiments, with stronger statistical dependence of the relative strain rate on the value of  $D_k$ . This could be a result of the fact that the  $90^\circ$  indenter imposes a larger disturbance on the granular material. To explore this more systematically, more wedge angles should be explored in addition to varying system size. Note that compression can be thought of as an indentation with a wedge angle of  $180^\circ$ , however, this data has not been added to Fig. 4.15 because the experimental conditions for the two sets of experiments are different: for compression, the particles are all submerged in heavy viscosity mineral oil to eliminate cohesive interactions while in the indentation experiments, all particles are completely dry.

We have not yet performed systematic studies as a function of cohesion, though this could be explored in the future. Interactions between grains can be tuned as described in Chapter 2. It would be interesting to see how the relationship between the structure and dynamics depends on

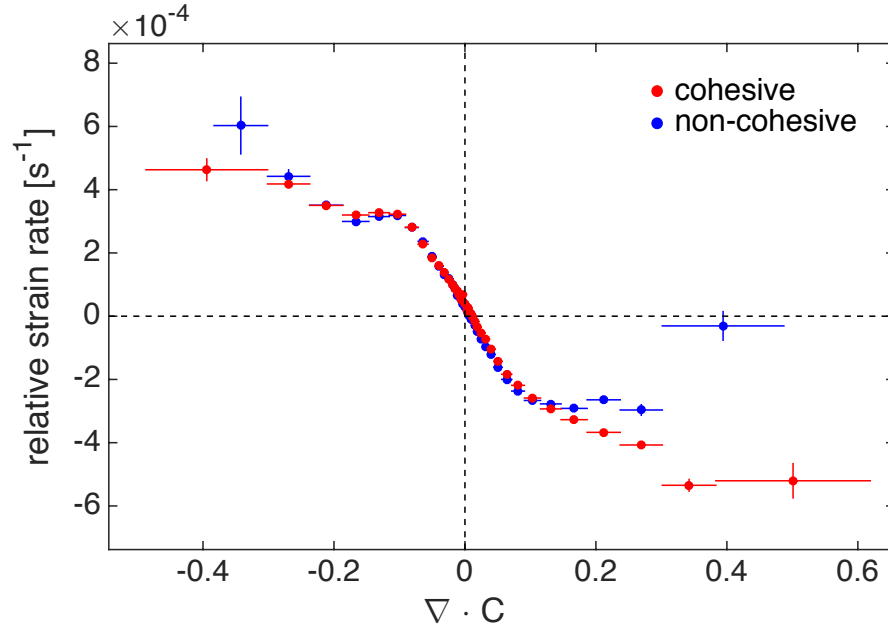


Figure 4.13: Relative deviatoric strain rate vs  $D_k = \vec{\nabla} \cdot \vec{C}$ .  $D_k$  is logarithmically binned, and data points represent the average relative strain rate within each bin. Vertical error bars represent the standard error of the mean of the relative strain rate within each bin, and horizontal error bars represent bin widths. Each bin contains at least 100 data points, and these curves contains data from 30 experiments.

cohesion as well as system size and indenter angle.

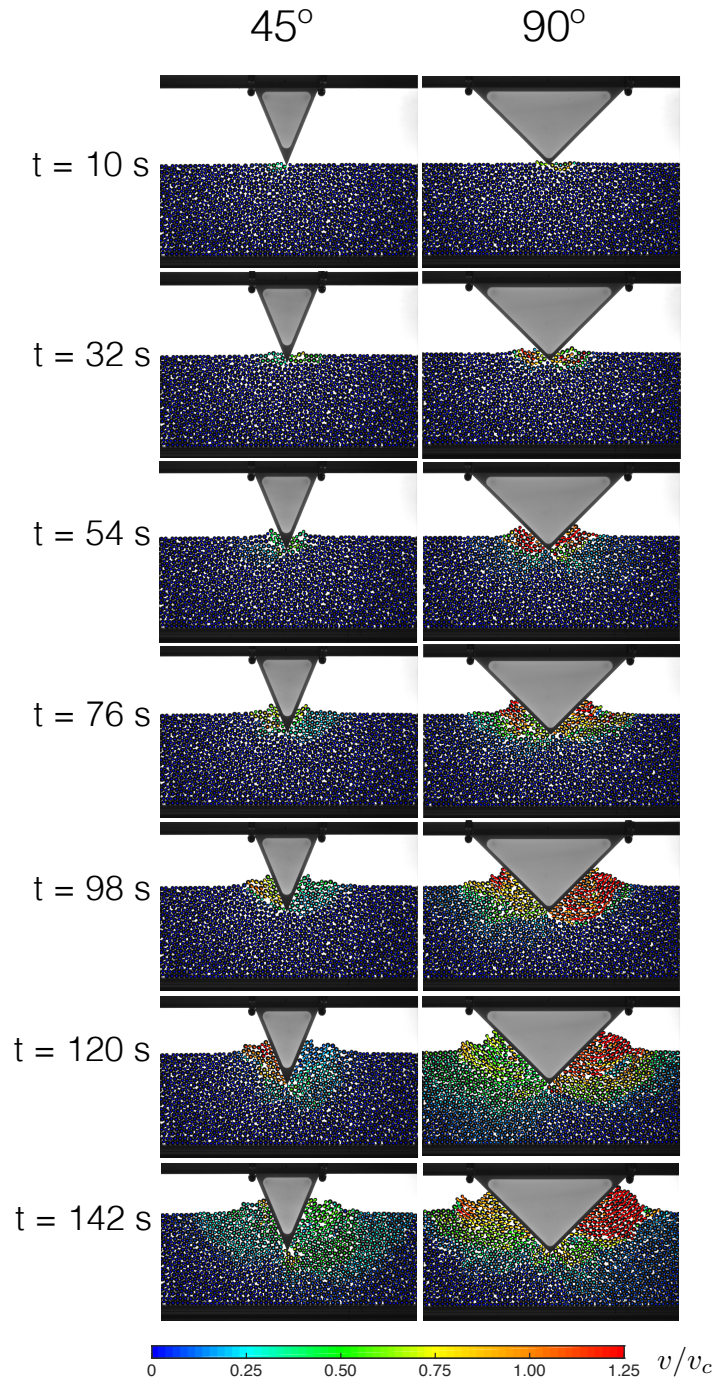


Figure 4.14: Particle velocities for indentation experiments into dry granular packings. Indenter angles are  $45^\circ$  for the experiment shown in the left column  $90^\circ$  for the experiment shown in the right column.

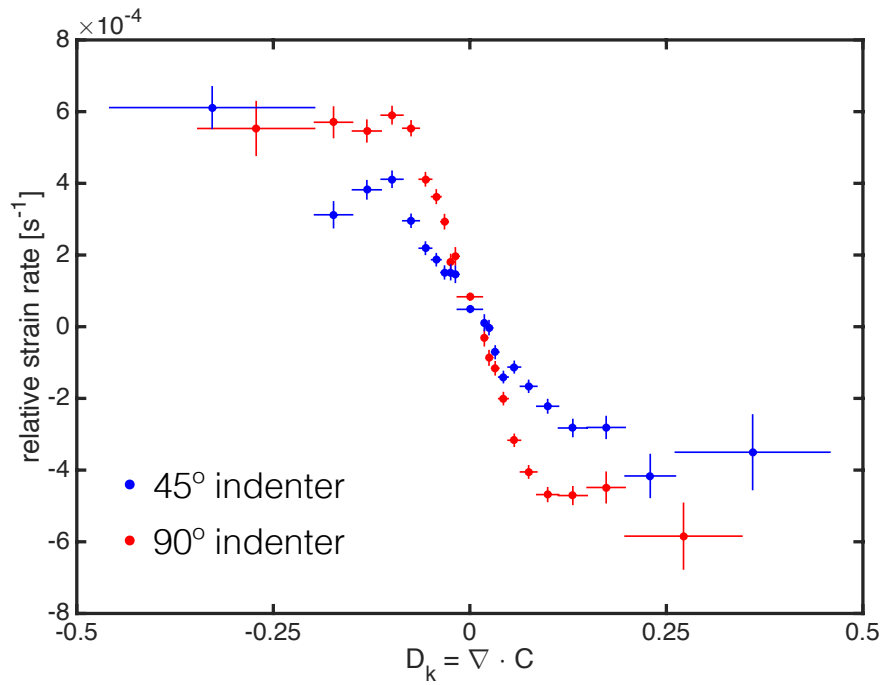


Figure 4.15: Relative strain rate as a function of  $D_k$ .  $D_k$  values are divided into logarithmically-spaced bins, each of which contains at least 100 data points. Relative strain rates for 5 experiments at each indenter angle are averaged within each  $D_k$  bin, shown as circles in the plot. Standard error of the mean for within each bin are shown as vertical errorbars, and horizontal errorbars show bin width for each  $D_k$  bin.

# Chapter 5

## Extended Dynamics

### 5.1 Introduction

While there are statistical correlations between structure and dynamics at the local scale, shear bands are, by definition, extended regions of intense shear. Therefore, it is possible that local information alone is not sufficient to fully understand the mechanical response of amorphous materials. In fact, if we overlay interpolated local structure and dynamics onto the same image, we see longer length-scale correlations. Fig. 5.1a shows an experimental image with an overlay of the local  $D_k$  field, which classifies regions according to their relative free area, with  $D_k < 0$  corresponding to underpacked regions and  $D_k > 0$  identifying overpacked regions. Fig. 5.1b shows the interpolated deviatoric strain rate field and Fig. 5.1c shows  $D_k$  both fields superimposed onto the experimental image. In Fig. 5.1c, it appears that bands may largely avoid overpacked regions and connect underpacked regions. The goal of this chapter is to quantify the extent to which this is true.

We begin our extended analysis by identifying spatially extended features in the strain rate, and exploring how structural quantities vary depending on their location relative to the extended strain rate bands. Because the dynamics are so heterogeneous and not all of the pillar is even aware of the

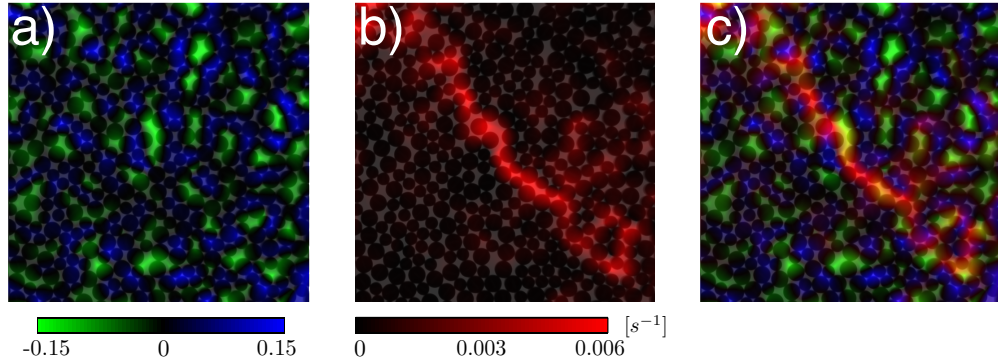


Figure 5.1: Interpolated fields on top of the experimental image. a)  $D_k$ , b) deviatoric strain rate, and c) both  $D_k$  and deviatoric strain rate. A transient shear band winds through the packing, connecting several underpacked regions while largely avoiding the overpacked regions.

imposed disturbance, we find that identifying spatially extended features in the dynamics is much more robust than looking at the structure first. All data presented in this chapter is a preliminary and therefore serves as a status report. Implementation of more sophisticated techniques could improve the analysis and results presented here.

## 5.2 Identifying shear bands

Local strain rates are calculated for triangles with vertices defined by the centers of three particles, all of which are mutual neighbors, see Sec. 4.4 for details. To begin analysis of extended features, the deviatoric strain rate is interpolated to create a field by assigning the strain rate values for each triangle to the centroid of that triangle. The strain rate is then linearly interpolated between the triangle centroids. We next define a region of interest, which is slightly narrower than the original pillar width and about 15 particle radii tall. The size of this window remains constant throughout all experiments, but the location moves down at the speed of the compression. The size is chosen to include as much of the deforming pillar as possible while excluding as much of the static region as possible as well as avoiding effects caused by the pillar boundaries. At each

point in time, the left and right sides of the pillar are treated separately. The interpolated strain rate field along with boxed left and right regions of interest are shown in Fig. 5.2.

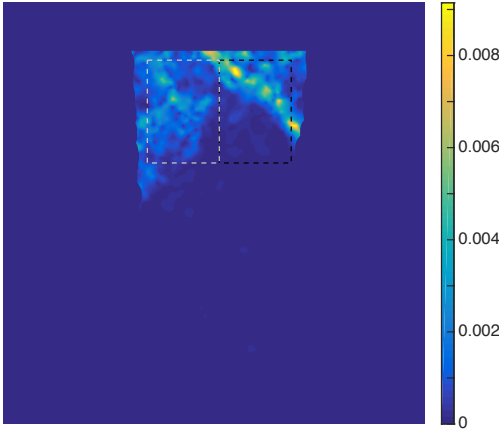


*Figure 5.2: Interpolated deviatoric strain rate field with regions of interest shown as dashed lines. Left and right sides are treated independently throughout the analysis.*

The current procedure for locating a shear band is outlined in Fig. 5.3. A particular region of interest is shown in Fig. 5.3a. The 2D spatial correlation of this region is determined by convolving a zero-padded version of this image with itself, shown in Fig. 5.3b. In the presence of a shear band, there is a line along which this correlation is high. To identify this line, we take the Radon transform [75] of the correlation, shown in Fig. 5.3c. Note that for images in Matlab, the y-axis labeling is consistent with matrix indexing, placing the origin in the upper left corner of the plot. The Radon transform does not accept axis labels as input, therefore there is a relative flip of the y-axis between Radon transform and the input image. This discrepancy is resolved by vertically flipping the input image prior to performing the Radon transform. The angle for which the Radon transform is maximal,  $\theta_{max}$ , is precisely perpendicular to the strongest line in the correlation, thereby providing the orientation of this line, as shown in Fig. 5.3d. Having identified  $\theta_{max}$ , we determine the perpendicular distance of the band,  $x_{\perp}$ , away from the line passing through the center of the image with orientation  $\theta_{band} = 90^{\circ} + \theta_{max}$  from the Radon transform of the strain rate image shown in Fig. 5.3a.  $x_{\perp}$  is defined as the maximal value of this Radon transform along the

column corresponding to  $\theta = \theta_{max}$ , see Fig. 5.3e. The strain rate region along with the identified band are shown in Fig. 5.3f. It is important to note that an assumption made in this analysis is there is exactly one shear band in each region, and that the band spans the region of interest. This could be improved upon by identifying multiple peaks in the radon transform in Fig. 5.3c or by looking at the peaks of the radon transform of the strain rate. Another refinement that would improve results could be to set a minimum allowed strain rate threshold for the existence of a shear band in each region.

### 5.3 Shear band angle

The average shear band angle is estimated using the procedure explained in 5.3a-c. There are 30 cohesive and 30 submerged experiments, each of which is split into left and right regions of interest, and each experiment containing around 200 time points. For a given region and point in time, the two-dimensional spatial cross-correlation is determined. All cohesive cross-correlations for left regions of interest are averaged together, and this average is shown in the upper left panel of Fig. 5.4. Similarly, all cohesive right regions of interest are averaged (upper right in Fig. 5.4), as are all left submerged regions of interest (lower left in Fig. 5.4) and right submerged (lower right in Fig. 5.4). Locating the peak in the Radon transform at zero translation (the line goes through the origin, so translational shift is zero) identifies the angle perpendicular to the band angle. To locate the maximum, a parabola of form  $y = a(x - x_0)^2 + b$  is fit to 10 points surrounding the peak. The fit parameter  $x_0$  identifies the location of the maximum, with the average shear band angle given by  $\theta = 90^\circ + x_0$ , and uncertainties given by the confidence intervals of  $x_0$ . This gives shear band angles of  $47^\circ$  to  $48^\circ$ . This estimate includes all points in time, however, it could be improved by only including time points for which a band is present. In addition, as will be discussed later in this chapter, the shear bands in these experiments often have curvature. This could have an impact on the estimated shear band angle.

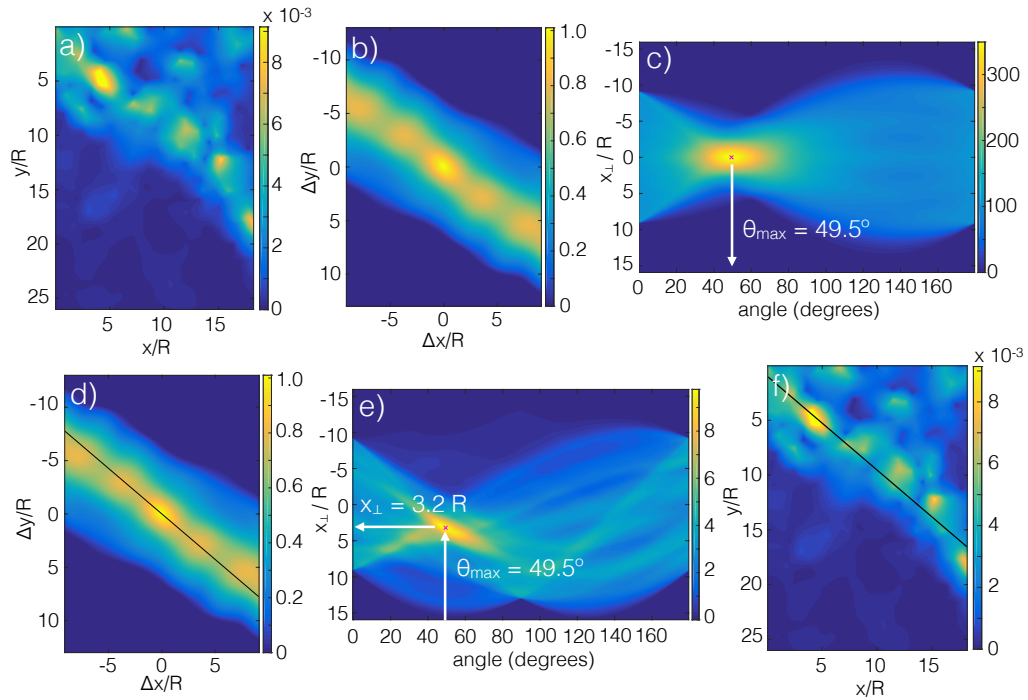


Figure 5.3: Steps to identify a single shear band at each point in time from the interpolated deviatoric strain rate field. a) Interpolated field. b) Two-dimensional spatial cross-correlation of interpolated field. Preferred directions of shear, if present, appear as extended bands in the spatial cross-correlation. c) Radon transform of spatial cross-correlation, the peak of which identifies the strongest line in b). d) Spatial cross-correlation with line identified from Radon transform overlaid. e) Radon transform of the image in a). This is used to locate the position of the shear band, given the orientation determined in c). f) Identified shear band overlaid on top of initial image.

## 5.4 Refining shear bands

Transient shear bands in these experiments, like the one shown in Fig. 5.5a, are often curved. As a result, the identification method presented in Sec. 5.2 needs refinement. To improve upon the initially identified location, the image in Fig. 5.5a is rotated by the band angle identified in Sec. 5.2. This rotated image is shown in Fig. 5.5b, with the band as identified by the previous method shown

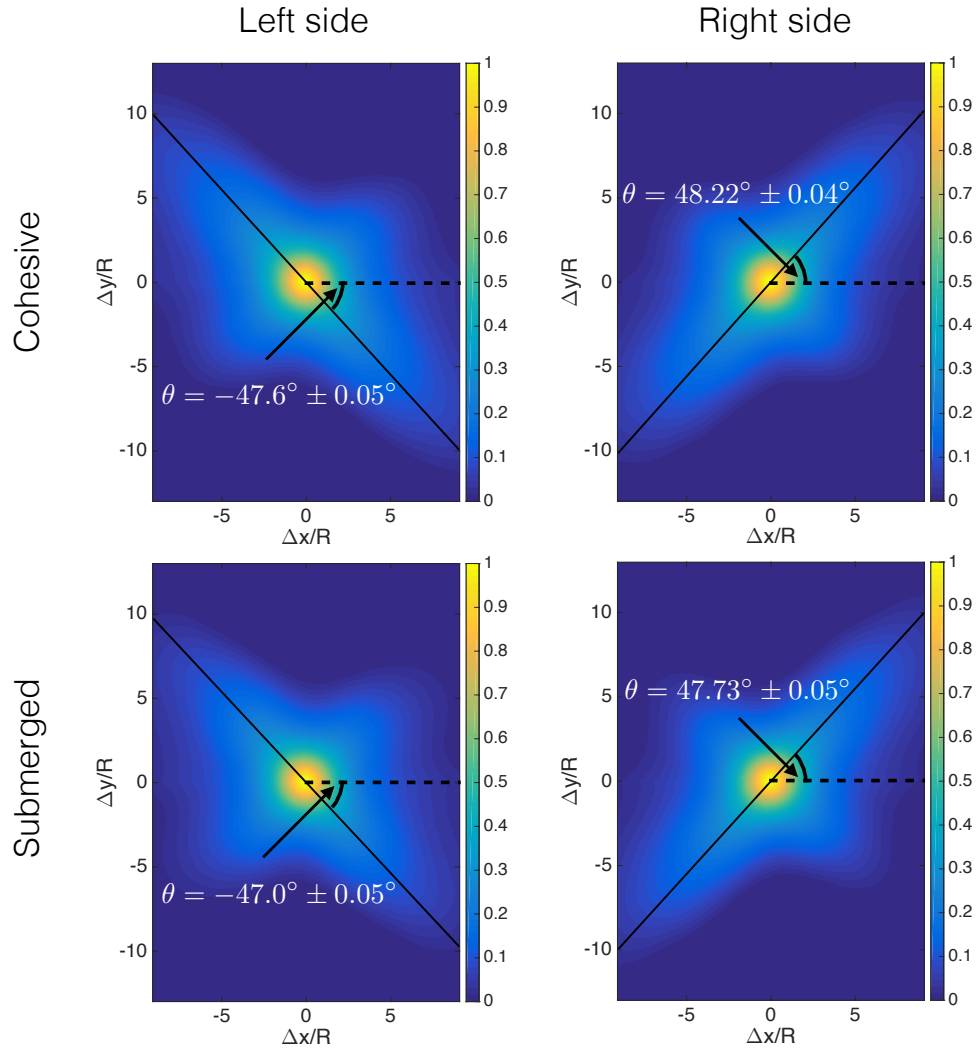


Figure 5.4: Average shear band angles identified independently for left and right sides of the pillar as well as cohesive and non-cohesive experiments. The color in the images represents the averaged two-dimensional spatial cross-correlation for 30 experiments each, with at least 200 time data points per experiment. The orientation of the most extended feature is determined using the Radon transform, as explained in Fig. 5.3. Around 10 points surrounding the peak in the Radon transform are fit to a function of the form  $y = a(x - x_0)^2 + b$ , with  $\theta = 90^\circ - x_0$ . Bounds shown for  $\theta$  are given by the 95% confidence intervals on the fit parameter  $x_0$ .

as the black line. In this rotated frame, the maximum deviatoric strain rate is identified for each column, overlaid as the white dots. White points are only kept if the strain value at the given location is greater than the strain rate value for which the cumulative distribution function of the strain rates in the image is equal to 0.9. The resulting points are linearly interpolated to ensure that they are evenly spaced, then Gaussian-smoothed with a filter window of a large particle radius, as shown by the red curve in 5.5b. The strain rate is averaged by integrating along paths parallel to the red curve. This average strain rate is plotted as a function of perpendicular distance away from the band in Fig. 5.5c. The band width is estimated by finding the full width at half the maximum value of this average curve, and for 25 images in which shear bands are strong, this width tends to be  $\sim 2.5 - 3$  particle radii. The final identified band with width is overlaid on top of the rotated strain image in 5.5d.

The shear band identification and refinement methods sometimes fail. This is typically due to the failure of the assumption that there is one and only one shear band in each image. Fig. 5.6 shows a couple of examples of the methods failing. These situations may be improved upon by allowing for the possibility of more than one band, as is the case in 5.6a, as well as allowing for the possibility that there are no bands in an image, as in 5.6b.

## 5.5 Comparison with structure

To compare the dynamics with the local structure, we begin by interpolating the  $D_k$  field by assigning the value for each triangle to the centroid of the triangle and linearly interpolating onto a grid. Both fields are rotated by the shear band angle as determined using the method presented in Sec. 5.2. Examples of these fields for a few snapshots are shown in Fig. 5.7. At the moment, there is no automated way to determine (1) if a transient shear band is present, and (2) if so, whether it has been well identified. Therefore, the examples in Fig. 5.7 are hand selected examples in which a shear band exists and has been accurately identified. Once rotated into the proper

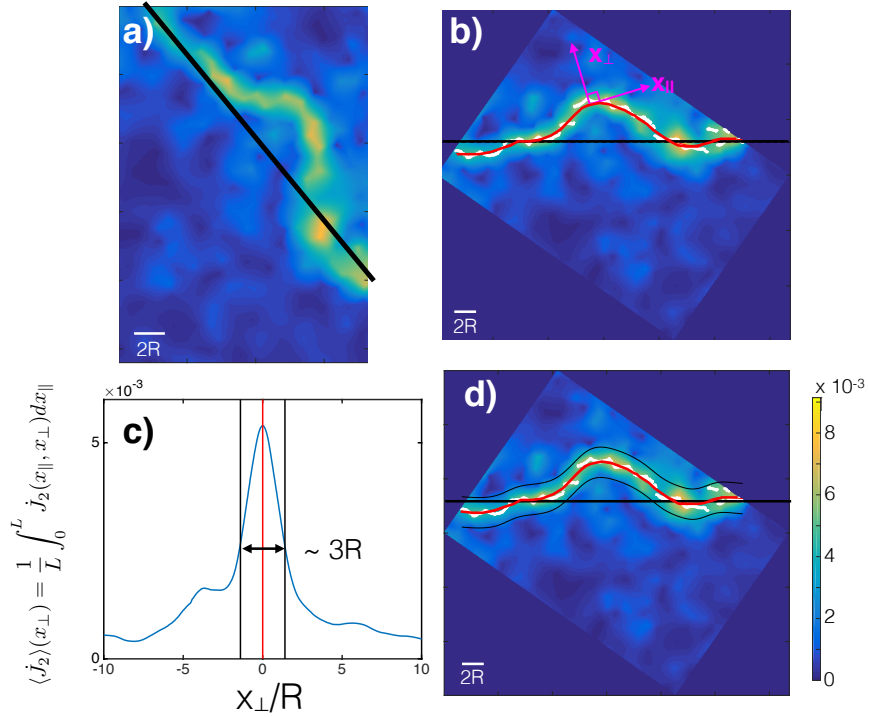


Figure 5.5: Color in all images indicates deviatoric strain rate, and magnitude is given by the color bar in the bottom right of the figure. a) A curved transient shear band with strongest angle identified. b) Image in a) rotated by previously identified band angle. Previously-identified band location is shown as the black line. In this rotated frame, the maximum deviatoric strain rate is identified for each column, overlaid as the white dots, and the resulting group of points is then Gaussian-smoothed, shown as the red curve, with a filter window of a large particle radius. c) Integral of strain along paths parallel to the band, as a function of perpendicular distance to the band. The band width is estimated by finding the full width at half the maximum value d) Final result.

frame, the average value of each field is then determined by integrating along paths parallel to the band and dividing by the path length through the pillar for each band. The averages for one example are shown in Fig. 5.7. Unsurprisingly, the center of the shear band corresponds to

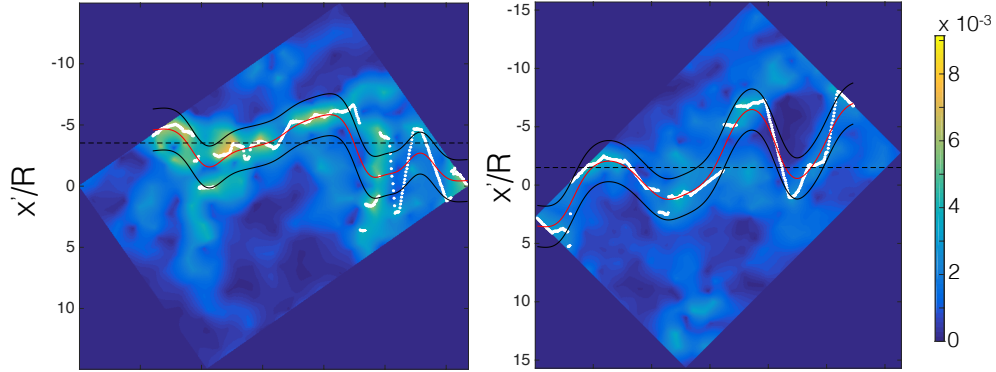


Figure 5.6: Examples of shear band identification method failing. In the picture on the left, there are multiple bands, so the assumption that there is only one is not valid. In the picture on the right, there is no band, so again the assumption that there is one shear band is incorrect.

the maximum average deviatoric strain rate. Interestingly, the location of the band coincides with a local minimum in the  $D_k$  field, at which  $D_k < 0$ , indicating that, at least locally, the path the shear band takes contains more underpacked regions than the immediate surroundings. This observation is consistent with our intuition and supports the idea that shear bands prefer underpacked regions and may avoid overpacked regions, at least for this particular example.

To explore this for more shear bands, we manually select 25 shear bands from 15 experiments, shown in Fig. 5.8. These bands are selected because the strain rates are localized into a band that spans the each image, and the identification algorithm correctly identified each band. The corresponding 25  $D_k$  and overlay the identified shear band, shown in Fig. 5.9. We then integrate each field along each band, as shown in Fig. 5.5 and Fig. 5.7, and average the results from 25 bands together. The green curve in Fig. 5.10 shows the average strain rate and the blue curve shows the average  $D_k$  value as a function of perpendicular distance away from the band. Interestingly, the trend observed in the one example shown in Fig. 5.7 holds up for the average of 25 bands, suggesting that paths with lower average  $D_k$  may be locally preferred, and that shear bands tend to find paths containing more underpacked than overpacked regions, at least for paths parallel to

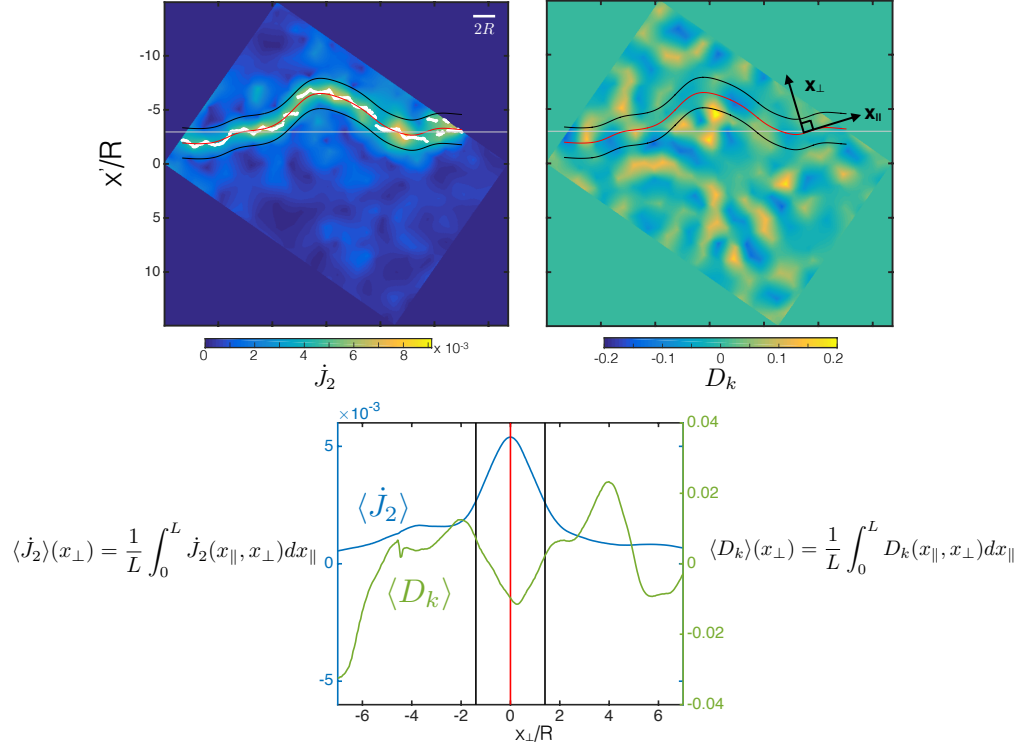


Figure 5.7: Top left: interpolated deviatoric strain rate field, with the identified transient shear bands overlaid. Top right:  $D_k$  field with shear band superimposed on top of the field. Lower plot: average of  $\dot{J}_2$  and  $D_k$  along paths parallel to shear band, as a function of perpendicular distance from the band. The maximum shear location coincides with a local minimum in the values of  $D_k$ , supporting the idea that bands tend to avoid locally overpacked regions.

the path the shear band traversed.

## 5.6 Particle rotations

We can perform the same analysis with other interpolated fields, and in particular we have looked at the magnitude of particle rotations. It has been previously noted that particle rotations tend to be higher inside of shear bands [37, 67]. Interpolated fields of particle rotations for the first 17 shear bands identified in Fig. 5.8 are shown in Fig. 5.11 with corresponding bands overlaid.

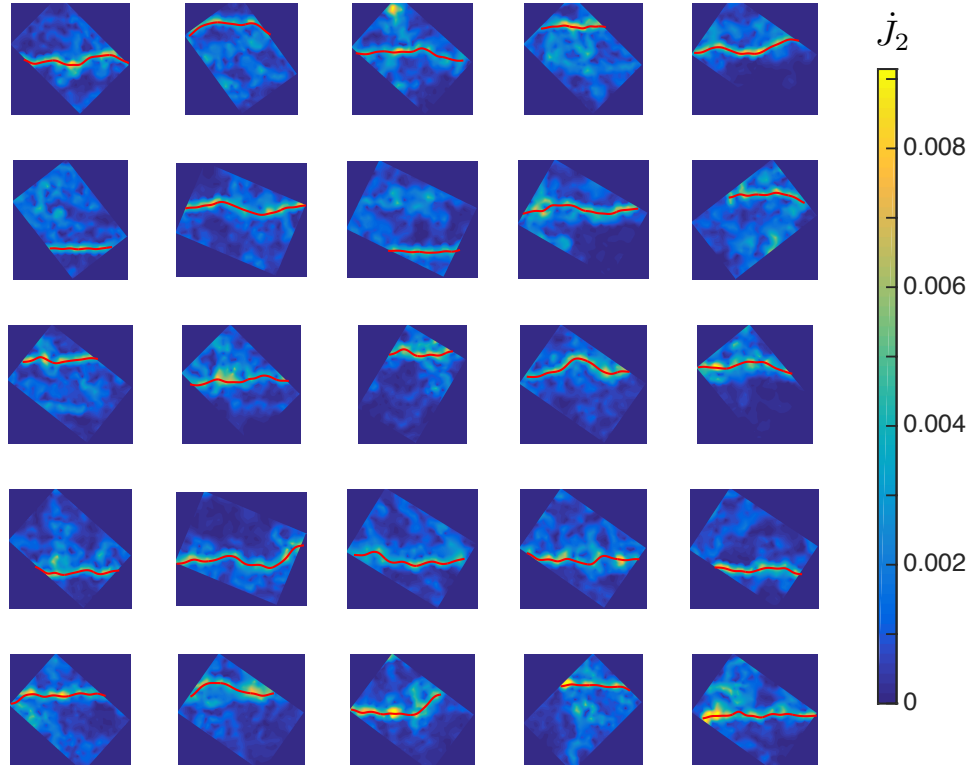


Figure 5.8: 25 snapshots of deviatoric strain rate fields from 15 experiments. Identified band is overlaid on top of each image, and images were manually selected as having strong shear bands.

We integrate the magnitude of the rotation along the band, and average the results from 17 bands together. The resulting curves are shown in Fig. 5.12. We see a peak in the magnitude of the particle rotations which is consistent with previous observations, at least for cohesive grains. Interestingly, previous observations we for asymmetric grains also, so it would be interesting to see if this trend exists in our non-cohesive data.

## 5.7 Future work

For the examples presented here, we have shown that the path the strain takes through the pillar is a local minimum in the  $D_k$  field, at least for paths through the  $D_k$  field that are parallel to the actual strain path taken. What about other paths that meander through the material? It would

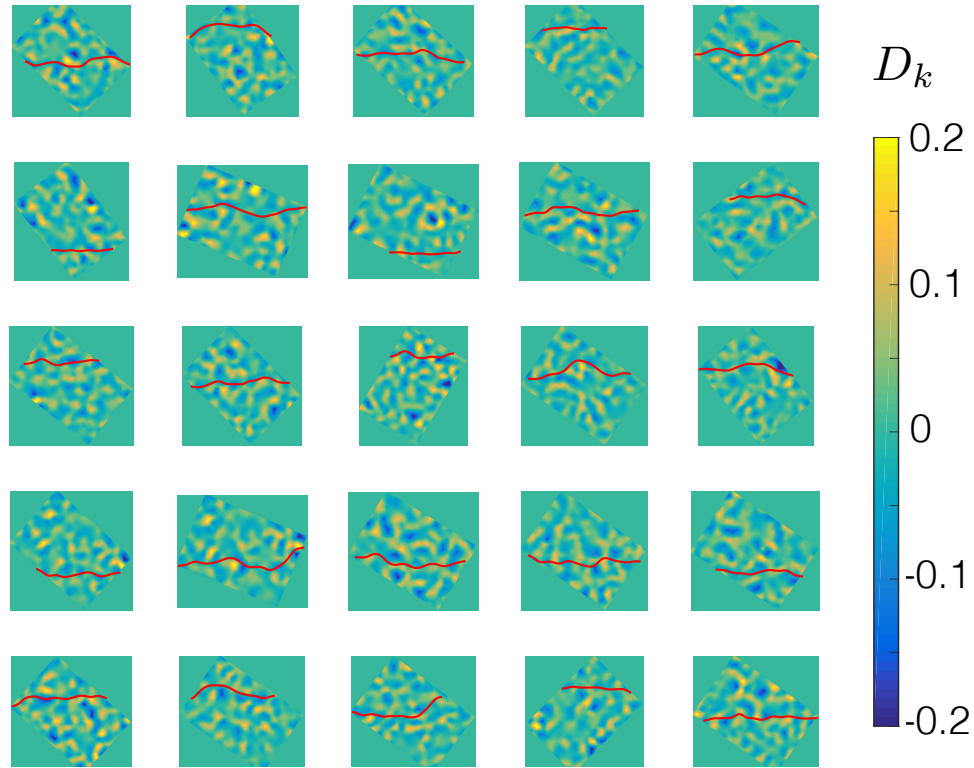


Figure 5.9:  $D_k$  fields corresponding to the 25 snapshots in Fig. 5.8. Bands identified from strain rate are overlaid in red.

be great to predict where the shear band should form based on the structure alone. One potential approach to this could be to define an energy landscape based on the  $D_k$  field, or even use the  $D_k$  field as an energy landscape, search for energy-minimizing paths through this landscape, and compare the results to the paths the shear bands take. This could be quite interesting, though it is likely challenging to implement and a rather computationally intensive calculation given the complicated structure of the  $D_k$  field. Another approach may be to generate numerous paths and evaluate the energy (first, one must define this energy) along each path to identify low energy or favorable paths through the  $D_k$  field, and to compare these paths to the shear bands.

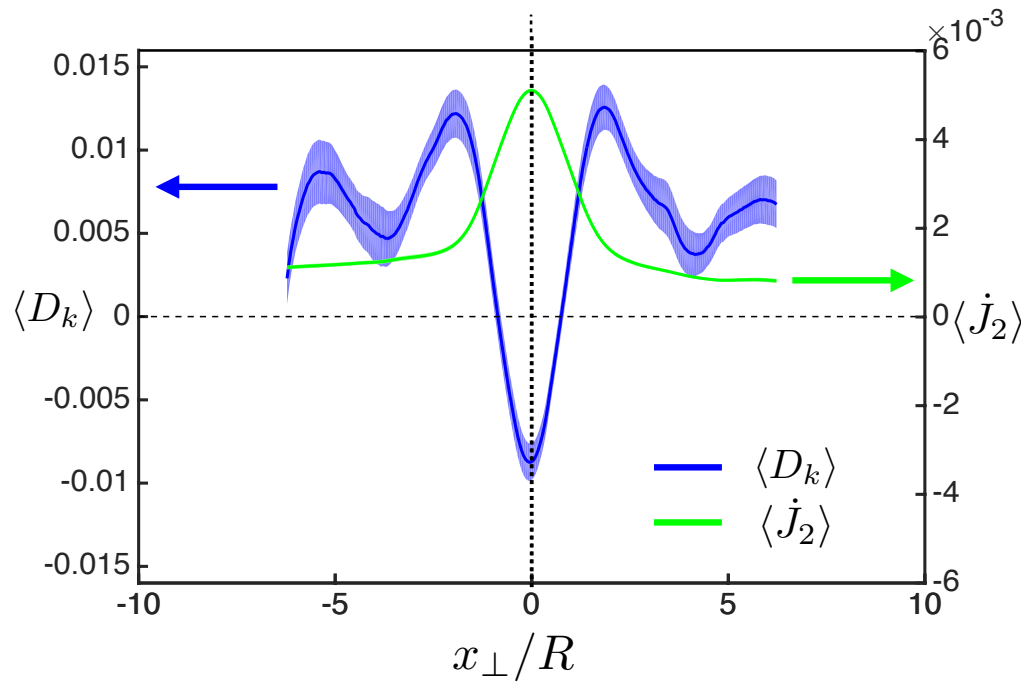
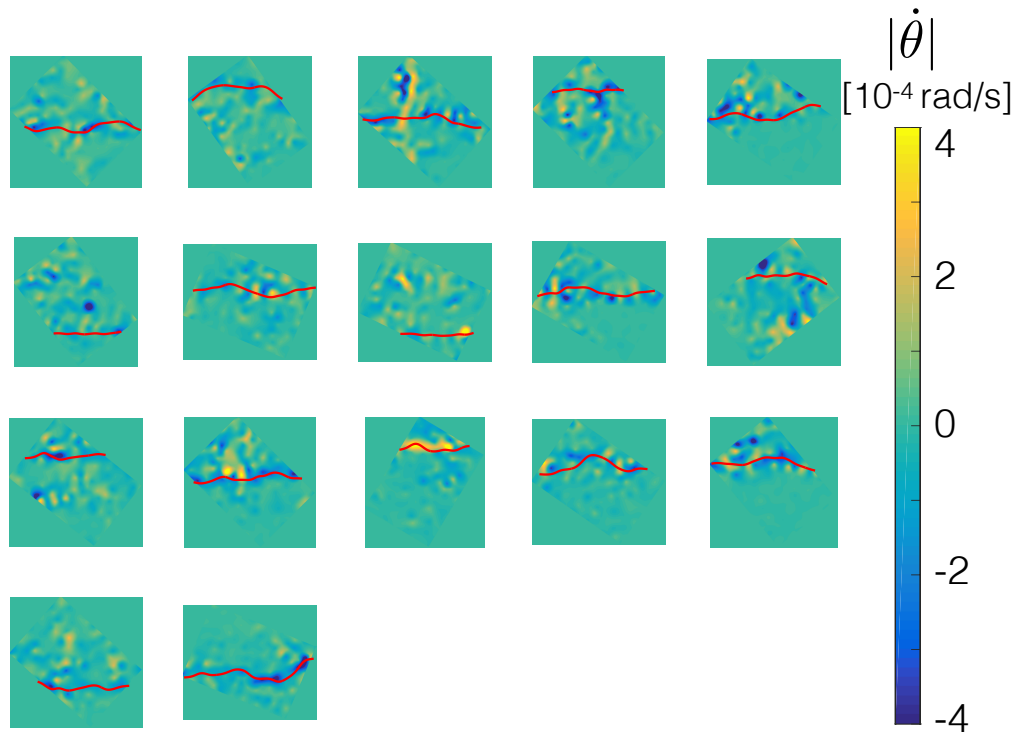


Figure 5.10: The green curve shows the average strain rates (in units of  $s^{-1}$ ) of 25 shear bands as a function of perpendicular distance to each band. As expected, there is a peak in this curve at  $x_{\perp} = 0$ . The blue curve shows the average  $D_k$  field integrated along the bands. The shading around the each curve represents the standard error of the mean. There is a minimum in  $\langle D_k \rangle$  that coincides with the maximum strain rate, suggesting that paths with more negative  $D_k$  regions may be favored for shear bands.



*Figure 5.11: Particle rotation rates for 17 points in time for which there is a shear band, interpolated onto a field. Identified shear band is super-imposed on top of each field.*

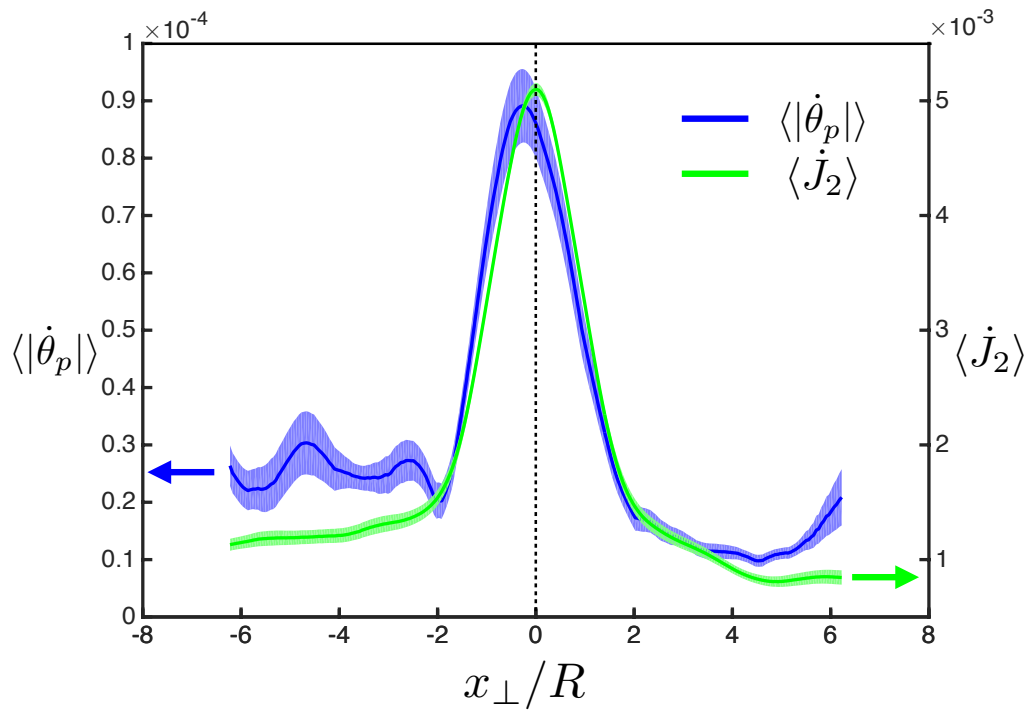


Figure 5.12: The green curve shows the average strain rates of 17 as a function of perpendicular distance to each band. The blue curve shows the average of the magnitude of rotation rate field integrated along the bands. The shading around the each curve represents the standard error of the mean. There is a maximum in the magnitude of the rotation rates that coincides with the maximum strain rate, suggesting particles tend to rotate more inside shear bands.

# Chapter 6

## Conclusion

### 6.1 Summary

The work presented in this thesis was inspired by the limited understanding of how the mechanical response of amorphous materials to an applied load is linked to the microscopic structure within the material. To explore this, we designed an experiment which quasi-statically deforms a granular packing. Grains within this packing are bidisperse, preventing crystallization. All packings are two-dimensional, allowing for direct visualization of all particle positions throughout the experiment. Chapter 1 presented details of the experimental setup as well as an in-depth explanation of image analysis techniques employed to identify particle centers and orientations from experimental images.

The two-dimensionality also enables us to introduce uniformly-distributed grain-grain interactions by adding a fluid, allowing us to explore deformation as a function of grain-grain interactions. Our grains are upright cylindrical rods, and when the grain separation is small, capillary forces pull the liquid up between the grains. Near contact, this liquid column reaches the tops of the grains, allowing the interaction to be tuned by depth of the liquid. These cohesive interactions are characterized in Chapter 2. Forces required to quasi-statically separate pairs of grains were mea-

sured as a function of liquid depth, and are shown to be in excellent agreement with our theoretical model and numerical calculations. We also measured these forces for groups of three particles, and we show that pairwise additivity is a reasonable approximation for these forces. Finally, we show that the forces required to separate particle pairs are larger than the forces measured to push pairs together under the same experimental conditions. This hysteresis is consistent with contact angle hysteresis that has been observed previously.

In Chapter 3, we introduced a new geometry-based measure of structural anisotropy in disordered materials. We showed that this measure has a nearly Gaussian distribution is intuitive: negative (positive) values identify regions which are locally less (more) well packed than the surroundings, which we refer to as underpacked (overpacked). Given the near-Gaussianity, we explore how the moments of the distribution depend on the packing fraction for numerically simulated packings of bidisperse soft spheres. We show that there is a kink in the standard deviation that coincides with the jamming transition, suggesting that a purely geometrical signature of jamming exists.

In Chapter 4, we explore the relation between local structure within a compressed granular pillar to the observed dynamics. Local structure is characterized using the new measure introduced in Chapter 3, and local dynamics are characterized by the deviatoric strain rate. We find a statistical correlation between the local structure and dynamics that is consistent with our intuition: locally overpacked regions tend to experience lower strain rates while locally underpacked regions tend to experience higher strain rates. This correlation is stronger for cohesive packings. Preliminary results are also included from experiments imposing a more localized disturbance by quasi-statically indenting the packing with a wedge. Only non-cohesive systems have been explored, but the size of the disturbance has been varied by changing the angle of the wedge. We see a similar correlation between structure and dynamics in these experiments, with the larger wedge angle producing a stronger correlation.

In Chapter 5, we first explain the current procedure for identifying the transient bands ob-

served in our compression experiments. We then make comparisons between structure inside these extended regions of high shear and structure outside. While these results are preliminary, our data suggests that the path the shear bands take tend to have more underpacked regions than overpacked regions. Further, the path the band takes has more underpacked regions than other nearby, parallel paths, and perhaps in this sense, we can think of the path taken as a more favorable path.

## 6.2 Future directions

A more thorough and systematic exploration of how dynamics vary with cohesive strength as well as the size of the imposed disturbance are two natural steps forward from here. Additionally, simulations of pillar deformation can provide information that is not accessible in the experiment, namely the net forces on each particle given the cohesive forces between grains measured in Chapter 2. It would be very interesting to see how local forces in pillar are related the observed structural features and dynamics within the pillar.

Another exciting direction forward is to explore more thoroughly, using interpolated fields in Chapter 5, how the structure inside the transient shear bands differs from the structure outside the bands. The current procedure is a step in the right direction, but refinements could greatly improve the analysis. For instance, the assumption that there is a transient shear band in every image is faulty, and yet that is an underlying assumption built into the analysis.

Finally, it would be great to predict where transient shear bands should form based on the structure alone. One potential approach to this could be to define an energy landscape based on the the interpolated structure, or even use the structure field itself as an energy landscape, search for energy-minimizing paths through this landscape, and compare the results to the paths the shear bands take. This could be quite interesting, though it is likely challenging to implement and a rather computationally intensive calculation given the complicated structure of the structure field. Another approach may be to generate numerous paths and evaluate the energy along each

path. To do this, an energy must first be defined. From this, it would be interesting to identify low energy or favorable paths through the structure field, and to compare these paths to the shear bands.

# Appendix A

## Experimental procedure and image analysis details

### A.1 Experimental details

This section gives step-by-step instructions for running an experiment. First, the CompactRIO, the camera, and the lightbox need to be plugged in, and the power supply should be on and set to about 24 V, see Fig 1.1 for details.

#### A.1.1 Initialization

A custom LabVIEW project, RunMotorAndRecordForceDataTrigger.lvproj, contains everything needed to run the experiment. Upon opening this LabVIEW project, a screen like the one shown in Fig. A.1 will appear. In order to communicate with the CompactRIO and run the experiment, a connection with the CompactRIO needs to be established. This is done by right-clicking on NI-cRIO-9074-0150EB86 and selecting Connect. Note that if the connection cannot be established, it is likely that the IP address of the CompactRIO has changed. The new IP address can be

determined by opening Measurement and Automation Explorer, expanding the Remote Systems menu, and clicking on the CompactRIO. To change the IP address in the LabVIEW project, right-click on NI-cRIO-9074-0150EB86, select Properties, and enter the new address.

Once the connection is established, the Scan Engine Mode needs to be changed to active, which can be done by right-clicking on NI-cRIO-9074-0150EB86 → Utilities → Scan Engine Mode → Switch To Active. This action is typically accompanied by an audible "click" from the motor. Next, to ensure that the motor is ready, right-click on Axis 1 and select Interactive Test Panel. Errors can typically be cleared by clicking on the button to the right of the error code and closing the Interactive Test Panel. Upon reopening, the Interactive Test Panel should be error-free.

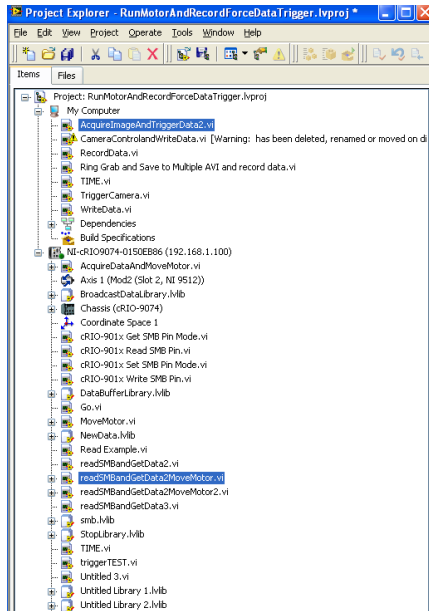


Figure A.1: Project explorer for *RunMotorAndRecordForceDataTrigger.lvproj*, the LabVIEW project that controls the experiment. The two .vi files needed to control the experiment are highlighted.

Two .vi files from the Project Explorer are needed to run the experiments, *AcquireImage-AndTriggerData2.vi* and *readSMBandGetData2MoveMotor.vi*, which are highlighted in Fig. A.1.

Both files require user input in the red boxed regions shown in Fig. A.2. The left side of Fig. A.2 shows readSMBandGetData2MoveMotor.vi, which is responsible for moving the motor and collecting force data when triggered to do so. Force data is saved locally on the CompactRIO, and will need to be downloaded to the experimental computer after the experiment is finished. Data path specifies where on the CompactRIO the force data will be saved. Maximum safe force value is an input based on the specifications of the load cells. LabVIEW is instructed to stop the motor if the force measured from any of the sensors exceeds this value. Position to travel to specifies, in steps, how far the motor will rotate. Currently, 50,000 steps is equivalent to one revolution of the motor. The current gear-ratio is 1:3, so three revolutions of the motor equal one revolution of the threaded rods, and the threaded rods have 10 threads per inch. This vi is set up only for constant speed translations, and speed is specified in terms of steps per second. Acceleration and acceleration jerk should be large so that the desired speed is attained quickly.

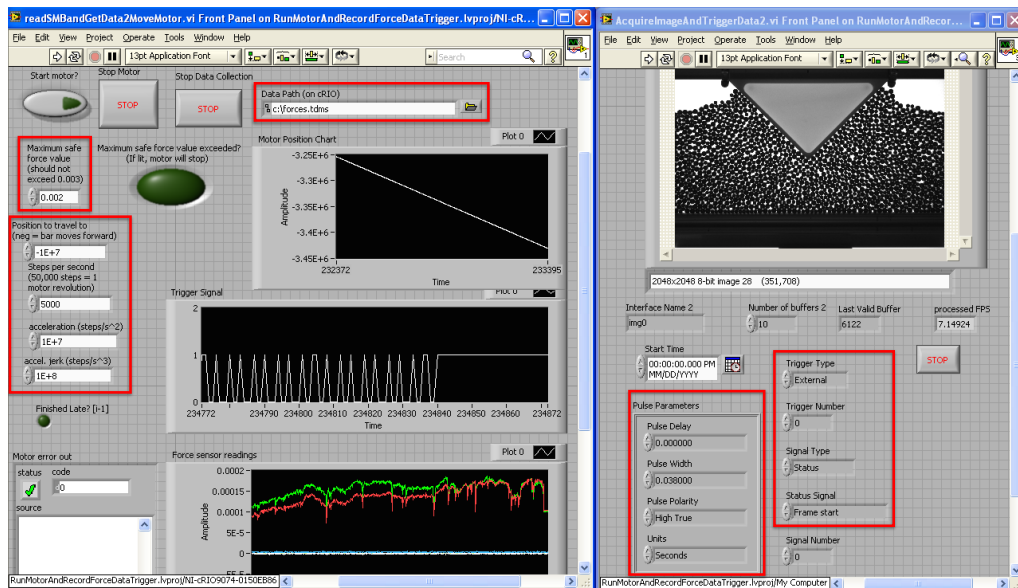


Figure A.2: Two custom LabVIEW files required for data acquisition. User inputs are boxed in red.

The other vi needed is AcquireImageAndTriggerData2.vi, which saves images and triggers the

recording of force data. Fields that require input are again boxed in red on the right side of Fig. A.2. The pulse parameters should be set as shown in the figure. Pulse Width could be modified if desired, though it should be slightly larger than the Scan Engine Scan Period (which can be determined by right-clicking on NI-cRIO-9074-0150EB86 and selecting Properties). The trigger properties should also be set as shown in Fig. A.2. This ensures the frame grabber sends a signal to the CompactRIO every time it begins the acquisition of a new image.

One final note, an error occurs upon deployment of RunMotorAndRecordForceDataTrigger.lvproj if ForceSensorStreaming.lvproj was the most recent project deployed. This seems to be fixed by first changing the Scan Engine Scan Period to 10 ms in RunMotorAndRecordForceDataTrigger.lvproj, deploying, then changing the Scan Period back to 35 ms and re-deploying. The motor does not operate with a Scan Period of only 10 ms, so a larger Scan Period must be used for the experiments.

### A.1.2 Running an experiment

To begin data collection, the "Start motor?" toggle should be switched to off in readSMBandGetData2MoveMotor.vi, see the left side of Fig. A.2. Once that is true, readSMBandGetData2MoveMotor.vi is run by clicking the white arrow button in the upper left. Next, AcquireImageAndTriggerData2.vi is executed by clicking the white arrow. After this starts running, the trigger signal graph in readSMBandGetData2MoveMotor.vi should look like the signal shown on the left of Fig. A.2. Now force and image data are being acquired simultaneously. Finally, the start motor toggle is switched to on.

Once an experiment is completed, if the motor is still going, the "Stop Motor" button is pressed in readSMBandGetData2MoveMotor.vi. Then AcquireImageAndTriggerData2.vi is then stopped by pressing the stop-sign button along the top. Finally, readSMBandGetData2MoveMotor.vi is stopped using the stop-sign button.

### A.1.3 Data types

Images are uncompressed .tif files streamed into .avi files located on a solid state hard drive. Each .avi contains 200 images, which can later be extracted into a sequence of images. Force data is saved as a .tdms file on the CompactRIO. This data can be accessed by entering the IP address of the CompactRIO in a browser on the LabVIEW computer. Using the File Explorer, the data can be found in the location specified in readSMBandGetData2MoveMotor.vi, and can be downloaded to the local computer. This .tdms file has 5 columns of data, columns for each force sensor and a column for global time. A file named positions.tdms is also saved for each experiment, and this contains the positions of the motor throughout the experiment.

## A.2 Force sensor calibration

In the unfortunate but inevitable event that force sensors break, the LabVIEW project ForceSensorStreaming.lvproj contains everything that is needed to calibrate new force sensors. As with running experiments, a connection must first be established with the CompactRIO, see Sec. A.1.1 for instructions. Once connected, two .vi files are needed, WriteToHost.vi and CollectAndSendData.vi. The project explorer and .vi files are shown in Fig. A.3. The only user input required here is the desired save path of the resulting force file. Unlike running experiments, this file will be saved somewhere on the LabVIEW computer. Note that for calibration, the Scan Period for the Scan Engine should be set to 10 ms, see Sec. A.1.1 for details.

The force sensor wires must be connected to the NI-9237 to the NI-9949 RJ50 screw terminal adapters as shown in Fig A.4. The calibration can begin after the sensor is connected to the NI 9237 and is secured in place. Once the desired path is entered into WriteToHost.vi, force sensor data is collected by running CollectAndSendData.vi. This program collects force data at 100 Hz and streams it over the network. WriteToHost.vi, once run, grabs the force data off the network and saves it into the specified file. The calibration procedure has been to add a known mass to the

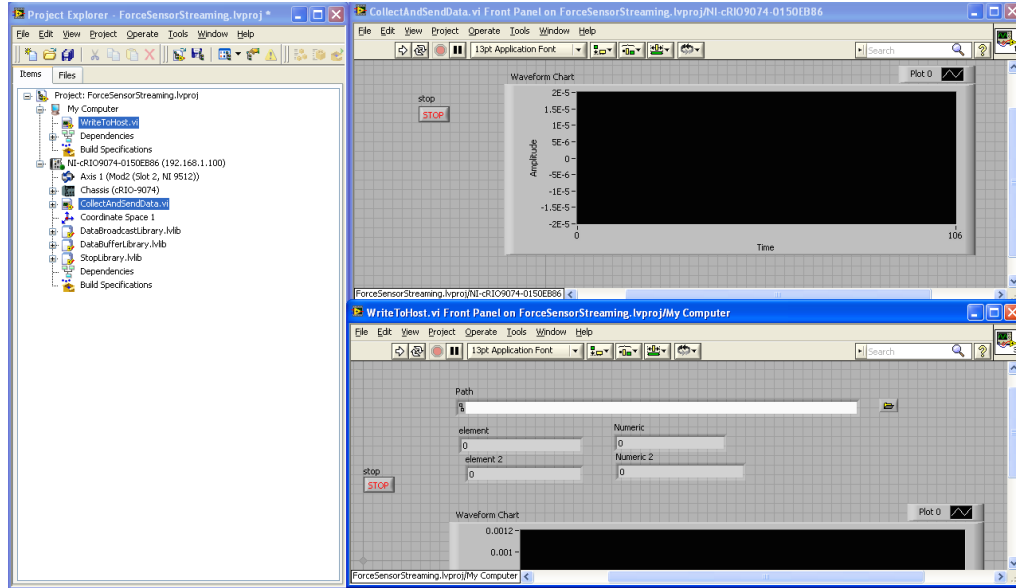


Figure A.3: Project explorer and .vi files needed to calibrate force sensors.

sensor, collect data for a minute or so, then pause WriteToHost.vi while adding or changing the mass. Repeating this procedure for several known masses produces a linear relationship between mass and sensor output, from which the conversion between force and sensor reading can be determined using the custom Matlab code calibrateForceSensor.m.

### A.3 Particle tracking codes

A code tree is shown in Fig A.5. The main function, trackEntireRun60mm.m, calls three other custom functions, which each call other functions, and so on. Image extraction can be performed outside of the tracking routine, and returnCenters60mmXcorr2.m can be used on a small subset of individual images throughout the experiment to determine good values for threshold parameters. After parameter values are chosen, trackEntireRun60mm.m is the only function that needs to be explicitly called.



Figure A.4: NI-9949 RJ50 screw terminal adapters. Omega LCEB mini-beam load cells attach to the terminals in the following way: green wire  $\rightarrow$  2, white wire  $\rightarrow$  3, red wire  $\rightarrow$  6, black wire  $\rightarrow$  7.

## A.4 Orientation codes

A code tree for determining particle orientations is shown in Fig A.6. The main function, `findParticleOrientationsNew.m`, calls three other custom functions. Particles need to be identified before orientations can be found. To explore parameter values, `getLines2.m` can be executed independently. After parameter values are chosen, `findParticleOrientationsNew.m` is the only function that needs to be explicitly called.

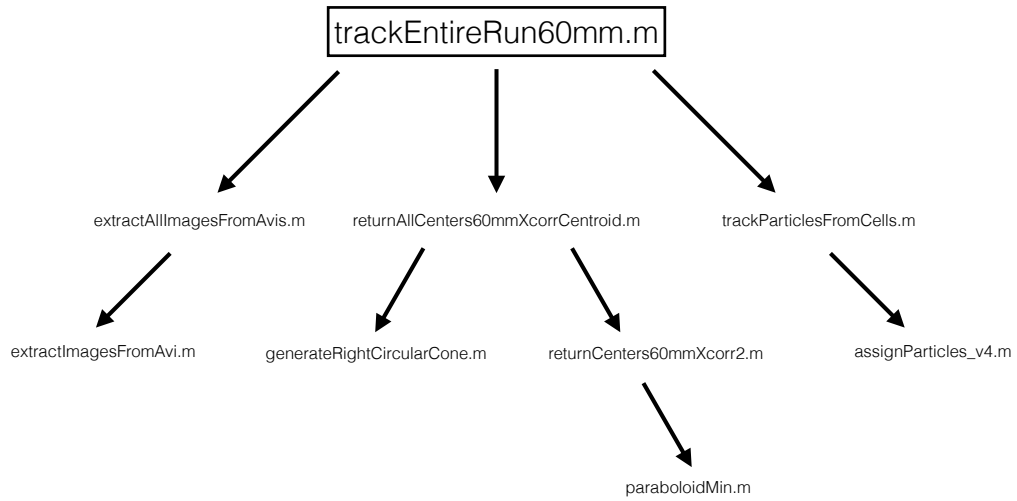


Figure A.5: Code tree showing the main particle tracking function, `trackEntireRun60mm.m`, as well as functions called within the main function.

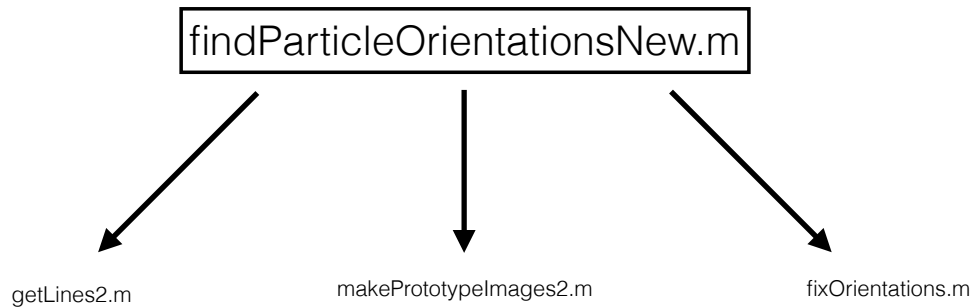


Figure A.6: Code tree showing the main orientation identification function, `findParticleOrientationsNew.m`, as well as functions called within the main function.

# Bibliography

- [1] R Ablett. XXV. An investigation of the angle of contact between paraffin wax and water. *Philosophical Magazine Series 6*, 46(272):244–256, August 1923.
- [2] A S Argon. Plastic deformation in metallic glasses. *Acta metallurgica*, 1979.
- [3] Franz Aurenhammer. Power diagrams: properties, algorithms and applications. *SIAM Journal on Computing*, 16(1):78–96, 1987.
- [4] F E Bartell and Kenneth E Bristol. Wetting Characteristics of Solid Surfaces Covered with Adsorbed Films. *Journal of Physical Chemistry*, 44(1):86–101, 1940.
- [5] Michael Berhanu and Arshad Kudrolli. Heterogeneous Structure of Granular Aggregates with Capillary Interactions. *Physical Review Letters*, 105(9):098002, August 2010.
- [6] G J Berman, D M Choi, W Bialek, and J W Shaevitz. Mapping the stereotyped behaviour of freely moving fruit flies. *Journal of The Royal Society Interface*, 11(99):20140672–20140672, July 2014.
- [7] N R Bernardino, V Blickle, and S Dietrich. Wetting of Surfaces Covered by Elastic Hairs. *Langmuir*, 26(10):7233–7241, May 2010.
- [8] N R Bernardino and S Dietrich. Complete wetting of elastically responsive substrates. *Physical Review E*, 85(5):051603, May 2012.

- [9] J. Berthier and K. A. Brakke. *The Physics of Microdroplets*. John Wiley & Sons, Inc, NJ, 2012.
- [10] Erik Bitzek, Pekka Koskinen, Franz Gähler, Michael Moseler, and Peter Gumbsch. Structural Relaxation Made Simple. *Phys. Rev. Lett.*, 97(17):170201, 2006.
- [11] L Bocquet, E Charlaix, S Ciliberto, and J Crassous. Moisture-induced ageing in granular media and the kinetics of capillary condensation. *Nature*, 396(6713):735–737, 1998.
- [12] Daniel Bonn, Jens Eggers, Joseph Indekeu, Jacques Meunier, and Etienne Rolley. Wetting and spreading. *Reviews of Modern Physics*, 81(2):739–805, May 2009.
- [13] Ned Bowden, Andreas Terfort, Jeff Carbeck, and George M Whitesides. Self-Assembly of Mesoscale Objects into Ordered Two-Dimensional Arrays. *Science*, 276(5310):233–235, April 1997.
- [14] Kenneth A Brakke. The surface evolver. *Experimental Mathematics*, 1(2):141–165, 1992.
- [15] John Canny. A computational approach to edge detection. *IEEE Transactions on pattern analysis and machine intelligence*, (6):679–698, 1986.
- [16] Dinesh Chandra and Shu Yang. Capillary-Force-Induced Clustering of Micropillar Arrays: Is It Caused by Isolated Capillary Bridges or by the Lateral Capillary Meniscus Interaction Force? *Langmuir*, 25(18):10430–10434, September 2009.
- [17] Dinesh Chandra and Shu Yang. Stability of High-Aspect-Ratio Micropillar Arrays against Adhesive and Capillary Forces. *Accounts of Chemical Research*, 43(8):1080–1091, August 2010.
- [18] Mingwei Chen. Mechanical Behavior of Metallic Glasses: Microscopic Understanding of Strength and Ductility. *Annual Review of Materials Research*, 38(1):445–469, August 2008.

- [19] Himantha Cooray, Pietro Cicuti, and Dominic Vella. The capillary interaction between two vertical cylinders. *Journal of Physics: Condensed Matter*, 24(28):284104, June 2012.
- [20] E D Cubuk, S S Schoenholz, J M Rieser, B D Malone, J Rottler, D J Durian, E Kaxiras, and A J Liu. Identifying Structural Flow Defects in Disordered Solids Using Machine-Learning Methods. *Physical Review Letters*, 114(10):108001, March 2015.
- [21] Eric G Daub and Jean M Carlson. Friction, Fracture, and Earthquakes. *Annual Review of Condensed Matter Physics*, 1(1):397–418, August 2010.
- [22] E De Castro and C Morandi. Registration of translated and rotated images using finite fourier transforms. *IEEE Transactions on pattern analysis and machine intelligence*, 9(5):700–703, September 2008.
- [23] Pierre-Gilles de Gennes, Françoise Bouchard-Wyart, and David Quéré. *Capillarity and Wetting Phenomena: Drops, Bubbles, Pearls, Waves*. Springer, New York, 2004.
- [24] Ceco D Dushkin, Peter A Kralchevsky, Vesselin N Paunov, Hideyuki Yoshimura, and Kuniaki Nagayama. Torsion Balance for Measurement of Capillary Immersion Forces. *Langmuir*, 12(3):641–651, January 1996.
- [25] E B Dussan V. On the spreading of liquids on solid surfaces: static and dynamic contact lines. *Annual Review of Fluid Mechanics*, 11(1):371–400, 1979.
- [26] GEP Elliott and A C Riddiford. Dynamic Contact Angles and Rates of Adsorption. *Nature*, 195(4843):795–&, 1962.
- [27] GEP Elliott and A C Riddiford. Dynamic contact angles: I. The effect of impressed motion. *Journal of Colloid and Interface Science*, 23(3):389–398, 1967.
- [28] M L Falk and J S Langer. Dynamics of viscoplastic deformation in amorphous solids. *Physical Review E*, 57(6):7192–7205, June 1998.

- [29] Michael L Falk and J S Langer. Deformation and Failure of Amorphous, Solidlike Materials. *Annual Review of Condensed Matter Physics*, 2(1):353–373, March 2011.
- [30] Jean Farago, Alexander Semenov, Stefan Frey, and Jörg Baschnagel. New conserved structural fields for supercooled liquids. *Eur. Phys. J. E*, 37(6):46, June 2014.
- [31] Carlos A Felippa. *Introduction to Finite Element Methods*. 2004.
- [32] B J Gellatly and J L Finney. Characterisation of models of multicomponent amorphous metals: the radical alternative to the voronoi polyhedron. *Journal of Non-Crystalline Solids*, 50(3):313–329, 1982.
- [33] A Gervois, L Oger, P Richard, and J P Troadec. Voronoi and radical tessellations of packings of spheres. *Lect. Notes Comput. Sci.*, 2331(SACLAY-SPHT-T-2001-135):95–104, May 2002.
- [34] Christoph Gögelein, Martin Brinkmann, Matthias Schröter, and Stephan Herminghaus. Controlling the Formation of Capillary Bridges in Binary Liquid Mixtures. *Langmuir*, 26(22):17184–17189, November 2010.
- [35] Nick Gravish, Paul B Umbanhowar, and Daniel I Goldman. Force and flow at the onset of drag in plowed granular media. *Physical Review E*, 89(4):042202, April 2014.
- [36] A L Greer, Y Q Cheng, and E Ma. Materials Science and Engineering R. *Materials Science & Engineering R*, 74(4):71–132, April 2013.
- [37] S A Hall, M Bornert, J Desrues, Y Pannier, N Lenoir, G Viggiani, and P Bésuelle. Discrete and continuum analysis of localised deformation in sand using X-ray  $\mu$ CT and volumetric digital image correlation. *Geotechnique*, 60(5):315–322, January 2010.
- [38] T C Halsey and A J Levine. How Sandcastles Fall. *Physical Review Letters*, 80(cond-mat/9801204. 14):3141–3144, 1998.

- [39] Z Han, Y Li, and H J Gao. Effect of frame stiffness on the deformation behavior of bulk metallic glass. *Journal of Materials Research*, 25(10):1958–1962, January 2011.
- [40] S Herminghaus. Dynamics of wet granular matter. *Advances in Physics*, 54(3):221–261, May 2005.
- [41] Stephan Herminghaus. Roughness-induced non-wetting. *Europhysics Letters*, 52(2):165, 2000.
- [42] Richard L Hoffman. A study of the advancing interface. I. Interface shape in liquid—gas systems. *Journal of Colloid and Interface Science*, 50(2):228–241, 1975.
- [43] D J Hornbaker, Réka Albert, István Albert, Albert-László Barabási, and Peter Schiffer. What keeps sandcastles standing? *Nature*, 387(6635):765, 1997.
- [44] Hiroshi Imai, Masao Iri, and Kazuo Murota. Voronoi diagram in the Laguerre geometry and its applications. *SIAM Journal on Computing*, 14(1):93–105, 1985.
- [45] Rulon E Johnson, Jr and Robert H Dettre. Contact Angle Hysteresis. pages 112–135. American Chemical Society, Washington, D.C., July 2009.
- [46] Rulon E Johnson, Jr, Robert H Dettre, and Dale A Brandreth. Dynamic contact angles and contact angle hysteresis. *Journal of Colloid and Interface Science*, 62(2):205–212, June 2004.
- [47] Sung H Kang, Ning Wu, Alison Grinthal, and Joanna Aizenberg. Meniscus Lithography: Evaporation-Induced Self-Organization of Pillar Arrays into Moiré Patterns. *Physical Review Letters*, 107(17):177802, October 2011.
- [48] A A Keller, V Broje, and K Setty. Effect of advancing velocity and fluid viscosity on the dynamic contact angle of petroleum hydrocarbons. *Journal of Petroleum Science and Engineering*, 58(1-2):201–206, August 2007.

- [49] P. A. Kralchevsky and K. Nagayama. *Particles at Fluid Interfaces and Membranes*. Elsevier, Amsterdam, 2001.
- [50] P A Kralchevsky, V N Paunov, N D Denkov, I B Ivanov, and K Nagayama. Energetical and force approaches to the capillary interactions between particles attached to a liquid-fluid interface. *Journal of Colloid and Interface Science*, 155(2):420–437, 1993.
- [51] P A Kralchevsky, V N Paunov, I B Ivanov, and K Nagayama. Capillary meniscus interaction between colloidal particles attached to a liquid—fluid interface. *Journal of Colloid and Interface Science*, 151(1):79–94, 1992.
- [52] M R Kuhn. Structured deformation in granular materials. *Mechanics of Materials*, 31(6):407–429, June 1999.
- [53] Kenneth K S Lau, José Bico, Kenneth B K Teo, Manish Chhowalla, Gehan A J Amaratunga, William I Milne, Gareth H McKinley, and Karen K Gleason. Superhydrophobic Carbon Nanotube Forests. *Nano Letters*, 3(12):1701–1705, December 2003.
- [54] Antoine Le Bouil, Axelle Amon, Sean McNamara, and Jérôme Crassous. Emergence of Cooperativity in Plasticity of Soft Glassy Materials. *Physical Review Letters*, 112(24):246001, June 2014.
- [55] Antoine Le Bouil, Axelle Amon, Jean-Christophe Sangleboeuf, Hervé Orain, Pierre Bésuelle, Gioacchino Viggiani, Patrick Chasle, and Jérôme Crassous. A biaxial apparatus for the study of heterogeneous and intermittent strains in granular materials. *Granular Matter*, 16(1):1–8, January 2014.
- [56] Eric P Lewandowski, Marcello Cavallaro, Jr., Lorenzo Botto, Jorge C Bernate, Valeria Garbin, and Kathleen J Stebe. Orientation and Self-Assembly of Cylindrical Particles by Anisotropic Capillary Interactions. *Langmuir*, 26(19):15142–15154, October 2010.

- [57] J Loudet, A Alsayed, J Zhang, and A Yodh. Capillary Interactions Between Anisotropic Colloidal Particles. *Physical Review Letters*, 94(1):018301, January 2005.
- [58] M. J. Turner. Stiffness and Deflection Analysis of Complex Structures. *Journal of the Aeronautical Sciences (Institute of the Aeronautical Sciences)*, 23(9):805–823, September 1956.
- [59] Basavaraj Madivala, Jan Fransaer, and Jan Vermant. Self-Assembly and Rheology of Ellipsoidal Particles at Interfaces. *Langmuir*, 25(5):2718–2728, March 2009.
- [60] M L Manning and A J Liu. Vibrational Modes Identify Soft Spots in a Sheared Disordered Packing. *Physical Review Letters*, 107(10):108302, August 2011.
- [61] E H Mansfield, H R Sepangi, and E A Eastwood. Equilibrium and mutual attraction or repulsion of objects supported by surface tension. *Philosophical Transactions of the Royal Society A-Mathematical Physical and Engineering Sciences*, 355(1726):869–919, 1997.
- [62] T G Mason, A J Levine, D Ertas, and T C Halsey. Critical angle of wet sandpiles. *Physical Review E*, 60(5):R5044, 1999.
- [63] Namiko Mitarai and Franco Nori. Wet granular materials. *Advances in Physics*, 55(1-2):1–45, January 2006.
- [64] Peter K Morse and Eric I Corwin. Geometric signatures of jamming in the mechanical vacuum. *Physical Review Letters*, 112(11):115701, March 2014.
- [65] M M Nicolson. The interaction between floating particles. *Mathematical Proceedings of the Cambridge Philosophical Society*, 45(02):288–295, 1949.
- [66] Sarah Nowak, Azadeh Samadani, and Arshad Kudrolli. Maximum angle of stability of a wet granular pile. *Nature Physics*, 1(1):50–52, October 2005.

- [67] M Oda and H Kazama. Microstructure of shear bands and its relation to the mechanisms of dilatancy and failure of dense granular soils. *Geotechnique*, 1998.
- [68] Nicholas T Ouellette, Haitao Xu, and Eberhard Bodenschatz. A quantitative study of three-dimensional Lagrangian particle tracking algorithms. *Experiments in Fluids*, 40(2):301–313, November 2005.
- [69] S Plimpton. Fast Parallel Algorithms for Short-Range Molecular Dynamics. *J. Comp. Phys.*, 117:1–19, 1995.
- [70] Boaz Pokroy, Sung H Kang, L Mahadevan, and Joanna Aizenberg. Self-organization of a mesoscale bristle into ordered, hierarchical helical assemblies. *Science*, 323(5911):237–240, 2009.
- [71] Yves Pomeau and Emmanuel Villermaux. Two hundred years of capillarity research. *Physics Today*, 59(3):39–44, March 2006.
- [72] J M S Prewitt. *Picture processing and Psychopictorics*. Academic Press, Waltham, Massachusetts, 1970.
- [73] H M Princen. Capillary phenomena in assemblies of parallel cylinders: I. Capillary rise between two cylinders. *Journal of Colloid and Interface Science*, 30(1):69–75, 1969.
- [74] David Quéré. Wetting and Roughness. *Annual Review of Materials Research*, 38(1):71–99, August 2008.
- [75] J. Radon. Über die Bestimmung von Funktionen durch ihre Integralwerte längs gewisser Mannigfaltigkeiten. *Akad. Wiss.*, 69:262–277, 1917.
- [76] Aneesur Rahman. Liquid Structure and Self-Diffusion. *The Journal of Chemical Physics*, 45(7):2585, 1966.

- [77] Srinivas R Ranabothu, Cassandra Karnezis, and Lenore L Dai. Dynamic wetting: Hydrodynamic or molecular-kinetic? *Journal of Colloid and Interface Science*, 288(1):213–221, August 2005.
- [78] B Srinivasa Reddy and Biswanath N Chatterji. An FFT-based technique for translation, rotation, and scale-invariant image registration. *IEEE Transactions on Image Processing*, 5(8):1266–1271, 1996.
- [79] Jennifer M Rieser, P E Arratia, A G Yodh, J P Gollub, and D J Durian. Tunable Capillary-Induced Attraction between Vertical Cylinders. *Langmuir*, 31(8):2421–2429, March 2015.
- [80] W Rose and R W Heins. Moving Interfaces and Contact Angle Rate-Dependency. *Journal of Colloid Science*, 17(1):39–&, 1962.
- [81] Chris H Rycroft. Voro++: A three-dimensional voronoi cell library in c++. *Chaos: An Interdisciplinary Journal of Nonlinear Science*, 19(4):041111, 2009.
- [82] Azadeh Samadani and A Kudrolli. Angle of repose and segregation in cohesive granular matter. *Physical Review E*, 64(5):051301, October 2001.
- [83] Peter Schall and Martin van Hecke. Shear Bands in Matter with Granularity. *Annual Review of Fluid Mechanics*, 42(1):67–88, January 2010.
- [84] M Scheel, R Seemann, M Brinkmann, M Di Michiel, A Sheppard, B Breidenbach, and S Herminghaus. Morphological clues to wet granular pile stability. *Nature Materials*, 7(3):189–193, February 2008.
- [85] G E Schröder-Turk, S Kapfer, B Breidenbach, C Beisbart, and K Mecke. Tensorial minkowski functionals and anisotropy measures for planar patterns. *Journal of Microscopy*, 238(1):57–74, April 2010.

- [86] Konrad Schwenke, Lucio Isa, and Emanuela Del Gado. Assembly of Nanoparticles at Liquid Interfaces: Crowding and Ordering. *Langmuir*, 30(11):3069–3074, March 2014.
- [87] Y D Shikhrmurzaev. Dynamic contact angles and flow in vicinity of moving contact line. *AIChE Journal*, 42(3):601–612, March 1996.
- [88] Steven Slotterback, Masahiro Toiya, Leonard Goff, Jack F Douglas, and Wolfgang Losert. Correlation between Particle Motion and Voronoi-Cell-Shape Fluctuations during the Compaction of Granular Matter. *Physical Review Letters*, 101(25):258001, December 2008.
- [89] Frans Spaepen. A microscopic mechanism for steady state inhomogeneous flow in metallic glasses. *Acta metallurgica*, 25(4):407–415, 1977.
- [90] Daniel J Strickland, Yun-Ru Huang, Daeyeon Lee, and Daniel S Gianola. Robust scaling of strength and elastic constants and universal cooperativity in disordered colloidal micropillars. *Proceedings of the National Academy of Sciences*, 111(51):18167–18172, December 2014.
- [91] Daniel J Strickland, Lei Zhang, Yun-Ru Huang, Daniel J Magagnosc, Daeyeon Lee, and Daniel S Gianola. Synthesis and mechanical response of disordered colloidal micropillars. *Phys. Chem. Chem. Phys.*, 16(22):10274–10285, 2014.
- [92] G Strom, M Fredriksson, P Stenius, and B Radoev. Kinetics of Steady-State Wetting. *Journal of Colloid and Interface Science*, 134(1):107–116, January 1990.
- [93] Michele Taroni and Dominic Vella. Multiple equilibria in a simple elastocapillary system. *Journal of Fluid Mechanics*, 712:273–294, September 2012.
- [94] H Tavana and A W Neumann. On the question of rate-dependence of contact angles. *Colloids and Surfaces A: Physicochemical and Engineering Aspects*, 282-283:256–262, July 2006.

- [95] P Tegzes, T Vicsek, and P Schiffer. Avalanche Dynamics in Wet Granular Materials. *Physical Review Letters*, 89(9):094301, August 2002.
- [96] R Vaidyanathan, M Dao, G Ravichandran, and S Suresh. Study of mechanical deformation in bulk metallic glass through instrumented indentation. *Acta materialia*, 2001.
- [97] Nikolina D Vassileva, Dirk van den Ende, Frieder Mugele, and Jorrit Mellema. Capillary Forces between Spherical Particles Floating at a Liquid Interface. *Langmuir*, 21(24):11190–11200, November 2005.
- [98] Orlin D Velev, Nikolai D Denkov, Vesselin N Paunov, Peter A Kralchevsky, and Kuniaki Nagayama. Direct measurement of lateral capillary forces. *Langmuir*, 9(12):3702–3709, 1993.
- [99] Dominic Vella and L Mahadevan. The “Cheerios effect”. *American Journal of Physics*, 73(9):817, 2005.
- [100] Dominic Vella, Paul D Metcalfe, and Robert J Whittaker. Equilibrium conditions for the floating of multiple interfacial objects. *Journal of Fluid Mechanics*, 549(-1):215–224, February 2006.
- [101] C A Volkert, A Donohue, and F Spaepen. Effect of sample size on deformation in amorphous metals. *Journal of Applied Physics*, 103(8):083539, 2008.
- [102] C A Wilson and J A Theriot. A correlation-based approach to calculate rotation and translation of moving cells. *IEEE Transactions on Image Processing*, 15(7):1939–1951, July 2006.
- [103] Nan Xue, Shuai Wu, Sijie Sun, David Quéré, and Quanshui Zheng. Strongly Metastable Assemblies of Particles at Liquid Interfaces. *Langmuir*, 30(49):14712–14716, December 2014.
- [104] G D Yarnold. The Hysteresis of the Angle of Contact of Mercury. *Proceedings of the Physical Society of London*, 58(325):120–127, 1946.

- [105] Lei Zhang, Gang Feng, Zorana Zeravcic, Teresa Brugarolas, Andrea J Liu, and Daeyeon Lee. Using Shape Anisotropy to Toughen Disordered Nanoparticle Assemblies. *ACS Nano*, 7(9):8043–8050, September 2013.